UNIVERSIDADE DE LISBOA
FACULDADE DE CIÊNCIAS
DEPARTAMENTO DE FÍSICA

Modelling Transitions between Brain States: from rest to motor execution

David Gonçalo de Nóbrega Pereira de Lima

Mestrado em Engenharia Física

Dissertação orientada por:
Prof. Alexandre da Rocha Freire de Andrade
Prof. Sofia Rita Cardoso Fernandes

2025

Resumo

Esta dissertação insere-se no âmbito de um projeto de investigação, atualmente em curso no Instituto de Biofísica e Engenharia Biomédica (IBEB), dedicado ao desenvolvimento de um software para construção de modelos personalizados do cérebro. Estes modelos permitirão prever respostas neuronais mediante estimulação elétrica, recorrendo a dados de eletroencefalografia (EEG), de forma a otimizar protocolos para o tratamento de patologias do foro neurológico com envolvimento das funções motoras. O principal objetivo do trabalho de dissertação é o desenvolvimento de uma rede neuronal artificial que represente os estados cerebrais associados a repouso e a execução motora. Um estado cerebral consiste na dinâmica existente entre redes neuronais no córtex, sendo caracterizado por um padrão de atividade elétrica, a conectividade funcional, que reflete a forma como estas redes comunicam e se organizam para uma dada condição. Para calcular esta conectividade funcional, foram utilizados dados de EEG em indivíduos saudáveis recolhidos no IBEB. Os dados de EEG foram medidos durante diferentes atividades: execução motora com a mão esquerda; execução motora com a mão direita; imagética motora com a mão esquerda; imagética motora com a mão direita; período de repouso. O sinal EEG é medido no escalpe e tem de ser transformado para o espaço cortical através de um processo chamado reconstrução do espaço fonte ou problema inverso. Para realizá-lo foi utilizado o modelo “fsaverage”, um modelo de cabeça genérico, obtido através da combinação de ressonâncias magnética dos cérebros de 40 sujeitos, juntamente com o algoritmo “eLORETA”. O cérebro é subdivido em várias regiões de interesse utilizando o atlas cortical (ou parcelamento) "Desikan-Killiany", e para cada região é obtida uma série temporal derivada do espaço fonte. A conectividade funcional, o modo como estes sinais interagem entre si, é quantificada por 3 métricas com base na magnitude e na fase dos sinais para as bandas de frequência alfa e beta, obtendo então matrizes de conectividade funcional que caracterizam os diferentes estados cerebrais durante as várias atividades. Todo este processo foi realizado utilizando o software de código aberto “MNE-Python”.

A conectividade funcional é analisada de 2 formas. Primeiro, uma análise geral é efetuada para detetar diferenças entre as conectividades dos estados cerebrais, calculando a distância euclidiana entre as conectividades médias de cada estado a cada frequência. Segue-se uma análise estatística na qual, para uma ligação entre 2 regiões, um elemento da matriz de conectividade funcional, é executado um teste de normalidade. Se a ligação para cada estado cerebral apresentar uma distribuição normal aplica-se análise de variância (ANOVA) para verificar se existem diferenças entre os vários estados cerebrais. Se for indicado que há uma diferença significativa é aplicado o teste de Tukey para identificar entre que par de estados existe esta diferença para esta ligação. Se a distribuição não for normal é aplicado o teste de Kruskal-Wallis para indicar se existe alguma diferença seguido pelo teste de Wilcoxon para identificar entre que estados a diferença se manifesta. É também aplicada uma correção tendo em conta a taxa de falsa descoberta (FDR). Isto é feito para todas as ligações, todas as bandas de frequências e todos as métricas de conectividade. De forma geral, conclui-se que as maiores diferenças entre estados cerebrais são maiores quando estados de execução ou imagética motora são comparados entre si, ao invés

de quando comparados com o repouso. Em particular, os estados que demostraram ser mais diferentes são a execução motora com mãos opostas, imagética motora com as mãos opostas e execução motora com a mão esquerda face a imagética motora com a mão direita.

Com a conectividade funcional calculada e analisada é construída a rede neural artificial. Uma rede é composta por nodos e as ligações entre os nodos. Cada nodo modela as dinâmicas locais da população de neurónios de cada região de interesse. Para isto foi escolhida a forma normal da bifurcação de Hopf. Este modelo de dinâmicas locais está estudado extensivamente, dada a sua grande relevância para esta dissertação, bem como no estudo de estados cerebrais e as suas transições no contexto de várias patologias neurológicas como Alzheimers e Parkinson. As ligações entre cada nodo indicam a relação entre as populações de neurónios de todas as regiões de interesse. Inicialmente estas ligações são modeladas de forma a refletir a anatomia do cérbero. Para isto é utilizada a base de dados Braingraph para obter 1064 conectomas para o parcelamento cortical escolhido. Estes conectomas são baseados em scans de MRI disponibilizados pelo Human Connectome Project (HCP). Cada conectoma contêm várias métricas como o número de fibras entre as várias regiões. Foi criado um conectoma genérico com a média das métricas dos 1064 conectomas. Este conectoma é chamado conectividade estrutural.

São simuladas várias séries temporais para cada nodo correspondentes aos dados empíricos, segmentos de 4 s com aproximadamente 2000 pontos (o sinal EEG tem uma frequência de amostragem de 500 Hz) e é calculada a conectividade entre os vários nodos, a conectividade funcional simulada. Para calcular a semelhança entre as matrizes de conectividade funcional empírica e simulada são utilizadas 4 métricas: a distância euclidiana, a distância de correção, a correlação de Pearson e o índice de similaridade estrutural. Com base nestas várias métricas é feita uma exploração dos parâmetros do modelo. É avaliado como variar cada parâmetro afeta a conectividade funcional simulada, a semelhança entre a conectividade funcional simulada e empírica, o efeito de cada conectividade estrutural e se estes parâmetros variam de forma diferente para diferentes variáveis como as métricas de conectividade funcional, as bandas de frequência e os estados cerebrais. Com esta exploração inicial feita, a conectividade entre os nodos do modelo é refinada de modo a refletir também a conectividade funcional e não só a conectividade anatómica do cérebro, obtendo-se a conectividade efetiva. Após isto, é realizada outra vez uma breve exploração dos parâmetros e é decidido o conjunto de parâmetros que melhor reproduzem a conectividade funcional empírica. Como os parâmetros que maximizam a semelhança entre conectividades muitas vezes não são únicos, são também introduzidas outras métricas como a meta-estabilidade e coerência globais e os estados probabilísticos metaestáveis resultantes da análise das dinâmicas dos vetores próprios (LEiDA). Tendo em conta tudo isto, é ajustado um modelo final para cada frequência, métrica de conectividade e estado cerebral.

O modelo final mostra a capacidade de reproduzir a conectividade funcional dos diferentes estados cerebrais, para as diferentes métricas e frequências com um alto grau de semelhança. Os parâmetros, fora algumas exceções, comportaram-se da forma esperada, sendo a implementação da conectividade efetiva responsável pelo maior incremento entre a semelhança empírica e simulada. Entre as métricas de semelhança destacou-se a distância euclidiana permitindo identificar um espaço de soluções muito mais restrito face aos outros métodos. Existe também uma alta correlação entre as diferenças gerais calculadas através da distância euclidiana para os dados empíricos e simulados. Para avaliar a semelhança entre as duas análises estatísticas foram aplicadas métricas da matriz de confusão. Estas indicaram que o modelo prevê com bastante precisão a maioria das diferenças significativas entre estados cerebrais, com um desempenho ligeiramente melhor a simular as diferenças entre os estados cerebrais que demonstraram as maiores diferenças. Portanto, o modelo reproduz as diferenças entre estados não só a um nível geral, mas também ao nível de cada ligação individual entre regiões do cérebro. A coerência global é também

modelada com sucesso permitindo estudar melhor os estados cerebrais. A meta-estabilidade e os estados probabilísticos metaestáveis são métricas que representam o aspeto dinâmico do sistema e para ambas foram obtidos resultados semelhantes. O modelo demonstra a capacidade de reproduzir os valores empíricos, mas não é possível restringire-lo a esses valores com os parâmetros disponíveis. Embora esta tese se tenha centrado exclusivamente em dados de EEG relacionados a execução motora e imagética a estrutura de modelação desenvolvida fornece uma base para aplicações mais amplas. Dado que o modelo atual reproduz com sucesso os estados cerebrais e as suas diferenças em condições saudáveis — e considerando que modelos baseados em Hopf já foram aplicados de forma eficaz para simular patologias neurológicas e estimulação elétrica — espera-se que a extensão deste modelo permita estudar os estados cerebrais patológicos efetivamente.

Palavras chave: Conectividade funcional, rede neuronal artificial, estados cerebrais

Abstract

This thesis is part of an ongoing research project at the Instituto de Biofísica e Engenharia Biomédica (IBEB), dedicated to developing software for constructing personalized brain models. These models aim to predict neuronal responses to electrical stimulation using electroencephalography (EEG) data, ultimately contributing to optimized therapeutic protocols for neurological disorders affecting motor functions. The main objective is to develop a brain network model capable of representing brain states associated with rest and motor execution. The EEG data used was collected from healthy right-handed participants during five conditions: rest, left and right-hand motor execution, and left and right-hand motor imagery. The EEG signals were preprocessed, transformed into cortical space using eLORETA and the fsaverage head model, and then parcellated using the Desikan–Killiany atlas. Functional connectivity (FC) was quantified through three metrics: Coherence (COH), phase locking value (PLV), and amplitude envelope correlation (Pearson). Outside the FC, other relevant metrics used were global coherence and metastability as well as the Probabilistic Metastable Substates (PMS) resulting from Leading Eigenvector Dynamics Analysis (LEiDA). Analyzing the empirical data revealed that all brain states are very similar. Global coherence, metastability and PMS showed no significant differences between states. The FC reveals some slight differences which were most pronounced between motor tasks, particularly opposite-hand movements showed the highest differences. The final model accurately reproduces empirical FC across tasks and frequencies, capturing not only overall similarities but also task-specific differences with high sensitivity and precision. Fitting global coherence showed that right-handed movements may require a higher degree of synchronization. While the model can reproduce the empirical dynamic measures (metastability and PMS), they cannot be fitted precisely.

Keywords: Functional Connectivity, Brain network model, Brain states

Agradecimentos

Em primeiro lugar queria agradecer aos meus orientadores, o professor Alexandre Andrade e a professora Sofia Fernandes, pela sua disponibilidade, esforço e paciência. Os seus conselhos e conhecimentos relativos ao tópico da tese foram imprescindíveis durante o trabalho.

A Vasco Silva pelo seu trabalho que foi a fundação desta dissertação e por todas as ocasiões em que se mostrou disponível para ajudar.

Obrigado aos meus amigos pela camaradagem, bons momentos e ajuda durante estes anos e a todas as pessoas que, de uma forma ou de outra, me ajudaram neste percurso.

Finalmente, gostaria de agradecer à minha família pelo amor, apoio e incentivo que me deram, sem eles nunca teria conseguido chegar a este ponto.

Index

List of Figures

List of Tables

List of Acronyms

ANOVA Analysis of Variance. 29

BEM Boundary Element Method. xiii, 6, 16

BNM Brain Network Model. 1, 2, 9, 10, 21, 55

COH Coherence. xiv, xv, xvii–xix, xxi, xxii, 11, 27, 33, 40, 42–45, 47, 52, 54, 55, 68, 69, 71, 72, 87–89, 91, 93, 95, 98

dCor Distance Correlation. 25, 26

DTI Diffusion Tensor Imaging. 9, 10

DWI Diffusion Weighted Magnetic Resonance Imaging. 10

EC Effective Connectivity Matrix. xii, xxi, 10, 22, 24, 26, 42, 43, 45, 91, 93

EC Effective Connectivity. xii, xiv, xv, xvii–xix, xxi, 10, 24, 25, 42–47, 51, 55, 56, 86–96

ED Euclidean Distance. xiv, xv, xxi, 25, 28, 29, 31–34, 40, 43, 45, 52, 53, 55, 56

EEG Electroencephalogram. 3

EEG Electroencephalography. xiii, 1–3, 5–7, 9, 13–15, 18, 22, 25, 27, 55, 56

eLORETA Exact Low Resolution Electromagnetic Tomography. 7, 18

Envelope Envelope Functional Connectivity. xiv, xv, xviii, xix, xxii, 12, 31, 33, 34, 40, 45, 53–55, 69, 70, 73, 74, 88, 90–93, 95, 100, 101

FA mean mean of the fractional anisotropies of the fibers. xiv, 21, 40, 55, 86

FC Functional Connectivity Matrix. xiv, xv, xxi, 10, 25, 28, 29, 33, 34, 52, 53

FC Functional Connectivity. xiii–xv, xvii–xix, xxi, xxii, 1, 10–13, 22, 24–29, 31–34, 40, 42–47, 49, 51, 53–56, 67–75, 77, 86–94, 97, 101

FDR False Discovery Rate. 29, 54

FEM Finite Element Method. 6

fMRI Functional Magnetic Resonance Imaging. 1, 5, 9, 22, 27, 55, 56

List of Acronyms

FN False Negative. 29

FP False Positive. 29

GFP Global Field Power. xiii, 17

HCP Human Connectome Project. 21

IBEB Instituto de Biofísica e Engenharia Biomédica. 1, 13

ICA Independent Component Analysis. 14

ICP Iterative Closest Point. 16

KL Symmetrized Kullback-Leibler Divergence. 28

KOP Kuramoto Order Parameter. 26, 27, 56

LEiDA Leading Eigenvector Dynamics Analysis. xiv, 24, 25, 27, 28, 35, 36, 50, 56

LORETA Low Resolution Electromagnetic Tomography. 7

ME Motor Execution. xiii, 2, 13, 33, 56, 67

MEG Magnetoencephalography. 1, 5, 18, 22

MEL Motor Execution Left. 13, 14

MER Motor Execution Right. 13, 14

MFM Mean Field Model. 8

MI Motor Imagery. xiii, 2, 13, 33, 56, 67

MIL Motor Imagery Left. 13, 14

MIR Motor Imagery Right. 13, 14

MNE Minimum Norm Estimation. 7

MNE-Python MNE-Python. 7, 12, 14, 16, 17, 20

MRI Magnetic Resonance Imaging. 6, 15, 16, 18, 21

NFM Neural Field Model. 8, 9

NMW Neural Mass Model. 8

NPV Negative Predictive Value. 29, 54

PCC Pearson Correlation Coefficient. xxi, 11, 12, 25, 26, 53

PLV Phase-Locking Value. xiv, xv, xviii, xix, xxii, 11, 12, 32–34, 40, 45, 46, 52, 53, 55, 68, 70, 72, 73, 87, 89, 90, 92, 94, 96, 99, 100

PMS Probabilistic Metastable Substates. xiv, 24, 28, 35–37, 50, 56

PPV Positive Predictive Value. 29, 54

PSD Power Spectral Density. xiv, 24, 38, 39

PSP postsynaptic potentials. 3

REST Resting State. xiv, xv, xviii, 2, 13, 14, 31–34, 43, 44, 51–54, 56, 67, 86, 89–91

ROI Regions of Interest. 10

SC Structural Connectivity Matrix. xiv, 10, 21, 22, 24

SC Structural Connectivity. xii, xiv, 1, 10, 24–26, 40, 42, 45, 51, 55, 77, 79, 81, 83, 85, 86

sLORETA Standardized Low Resolution Electromagnetic Tomography. 7

SSIM Structure Similarity Index. 25

tDCS Transcranial Direct Current Stimulation. xiii, 13, 14

TN True Negative. 29

TNR True Negative Rate. 29, 54

TP True Positive. 29, 54

TPR True Positive Rate. 29, 54

Tukey's HSD Tukey's HSD (honestly significant difference) test. 29

WBM Whole Brain Model. 8

WMN Weighted Minimum Norm. 7

Chapter 1

Introduction

Brain states refer to distinct patterns of neural activity associated with different levels of consciousness, cognitive functions, or pathological conditions and can be characterized by Functional Connectivity (FC), which quantifies the patterns of synchronization between brain regions, often using coherence or phase-locking metrics. It is understood that these states emerge from the dynamic interactions of neuron populations in a synchronous fashion. These electrical signals are detected in the scalp by EEG, in the form of oscillations. These oscillations can be modelled considering theories of volume conduction in biological tissues. However, there are several factors that impact the accuracy of forward (from source to sensor) and inverse (from sensor to source) modelling of signal propagation in the brain. The problem of source estimation, *i.e.* estimating the sources of the brain activity at the scalp, is also an ill-posed problem as the solution is not unique. Solutions that rely on different models, assumptions and algorithms exist, however it is unclear which one is the best and under which circumstances should it be used. Besides the relevant signal being a attenuated and distorted by other tissues, EEG is also sensitive to other non-relevant components such as muscle activity, eye movements, heartbeat and even environmental factors. These components introduce artifacts in measured data that require extensive preprocessing. All these issues add up to make the development of a realistic modelling pipeline of brain states a complex challenge.

In Brain Network Models, the brain is divided into regions, represented by nodes whose local activity is described by mathematical equations. Nodes are connected by edges derived from anatomical characteristics of the brain, Structural Connectivity (SC), Functional Connectivity or both. BNMs have been used to study how FC and SC are linked to search for a characterization of the intricacies of different brain states. Clinically, BNMs have provided insights into the biology of various neuropathologies like Epilepsy, Stroke, Traumatic Brain Injury, Alzheimer's Disease, Schizophrenia and Disorders of Consciousness. Despite this, there are several obstacles associated with this kind of modeling, in addition to the difficulties added by the methods used to obtain the modelling data such as EEG, Functional Magnetic Resonance Imaging (fMRI) or Magnetoencephalography (MEG). Many models have been posed to describe the dynamics of connections between nodes, involving multiple parameters with no unique solution. Different metrics can be also be modelled.Functional Connectivity alone, usually the most important or even only metric, can be calculated using various methods. Overall the entire process of comparison and modelling can be very perplexing, especially regarding task-based connectivity. One particular obstacle to note is that literature involving Brain network modelling based on EEG is sparse, as most studies use fMRI data.

This thesis is inserted in an ongoing investigation project at Instituto de Biofísica e Engenharia Biomédica (IBEB), dedicated to the development of personalized brain models that will allow for the modulation of neuronal responses measured by Electroencephalography (EEG), with the goal of optimizing treatment protocols targeting motor involvement in neurological pathologies. The main goal of this thesis is the development of a Brain Network Model (BNM) that simulates the brain states associated with Resting State (REST), Motor Execution (ME) and Motor Imagery (MI), to serve as a future framework to optimize stimulation delivery to repair brain states associated with motor impairments.

Chapter 2

Scientific Background

2.1 Electroencephalography

Electroencephalography (EEG), is a noninvasive neuroimaging technique that records the electrical activity of the brain by placing electrodes on the scalp. The electrical signals generated by neurons are transmitted through the conductive properties of the head and brain tissues, a phenomenon known as volume conduction, detected by the electrodes. The signals are read as eletric potentials and recorded over time in the form of an Electroencephalogram (EEG) [2, 18, 65, 19, 85, 50].

EEG is widely used in clinical settings and research to study brain activity and diagnose various neurological conditions due to its noninvasive nature and relatively low cost. Other than research, some of the primary applications of EEG include diagnosing: epilepsy, sleep disorders, depth of anesthesia, coma and encephalopathies, brain death [2, 50].

Neurons are cells responsible for encoding, transmitting, and integrating signals originating the nervous system. The exchange of information within and between neurons involves changes in the membrane potential defined by the difference between the electric potentials at the intracellular and extracellular regions ($V_{int} - V_{ext}$). When a neuron is activated, transient changes are induced in its resting membrane potential called postsynaptic potentials (PSP). The PSP are generated by interacting pyramidal cells, or pyramidal neurons.

These potential changes are controlled by changing the concentration of ions, namely Na^+, Cl^-, and K^+, inside and outside the neuron. This flux of ions is controlled through ion channels present in the membrane, that open or close depending on the membrane potential and presence of specific neurotransmitters (dopamine, epinephrine, acetylcholine, etc). Neurotransmitters are produced by neurons when synaptic transmissions occur to induce changes in connected neurons [2, 18, 14, 50] .

An action potential can occur when the summation of incoming PSP reaches a certain threshold producing a spike or impulse. PSP can be either excitatory or inhibitory, bringing the neuron closer to or further from this firing threshold. Due to the very complex geometrical configuration of the electric currents arriving at neurons, with currents of opposite charges nearby, signals originated from action potentials are heavily decreased with distance and overwhelmed by postsynaptic potentials, thus the latter are the main source of cortical potentials measured by EEG [18, 14, 76, 19, 30, 50].

The PSP that EEG is capable of detecting are those generated by neuron populations where individual neurons are active in a synchronous, or close to, state, over a volume of cross-section of roughly 6 cm^2. This detected synchronous activity is seen in EEG as oscillations. The spectral properties of these oscillations or brain waves depend on the cell types and their connectivity and also reflect the brain state.

It is commonly established that brain waves are divided by their frequency into five main bands, shown in figure 2.1, which are delta (δ) 0.5–4 Hz, theta (θ) 4–8 Hz, alpha (α) 8–12 Hz, beta (β) 12–35 Hz and gamma (γ) > 35Hz.

Alpha brain waves can be detected during wakeful mental and physical relaxation with closed eyes, when the brain is in an idle state without actively concentrating. The suppression of alpha waves is a valid signal of a more active and engaged brain state.

Beta brain waves are generally known to be correlated with active, busy or anxious thinking and active concentration and can become stronger as we plan or execute movements.

Delta waves are associated with deep dreamless sleep and unconsciousness and theta waves with deep relaxation, creativity, intuition, dreaming, and fantasizing [18, 14, 50, 2, 3, 81, 80, 79, 19].

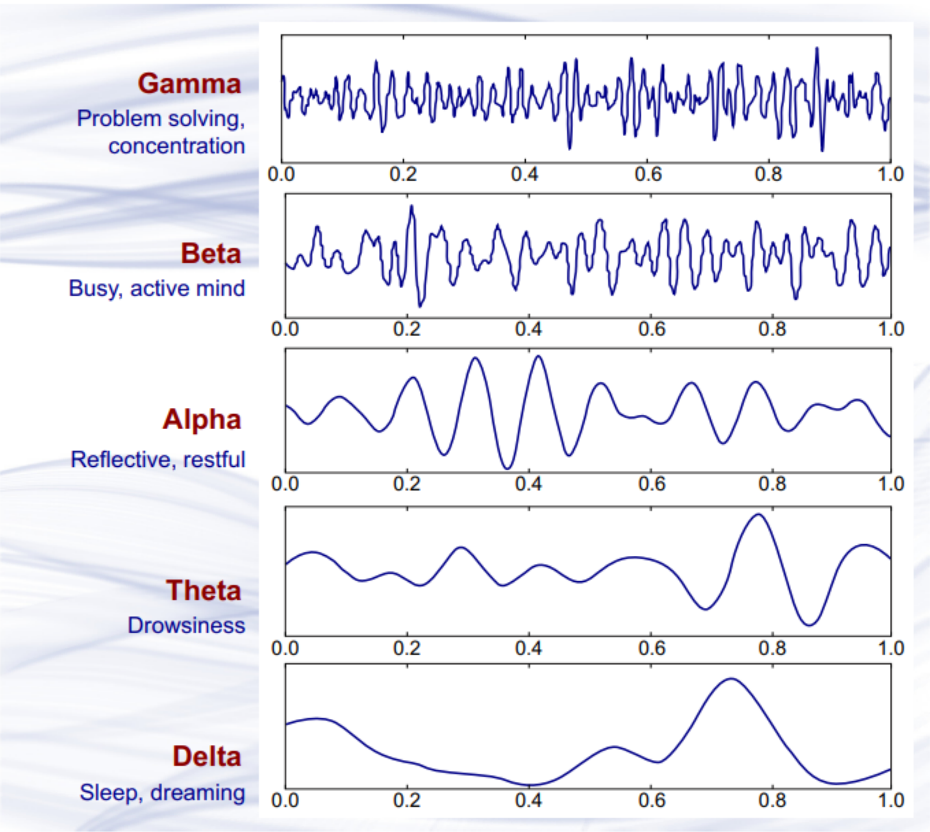

Figure 2.1: Brain wave samples with dominant frequencies belonging to beta, alpha, theta, and delta bands and gamma waves (Adapted fromAbhang et al. [2]).

2.2 Source Estimation

Regardless of the neuroimaging method used, whether it is Functional Magnetic Resonance Imaging (fMRI), Electroencephalography (EEG), or Magnetoencephalography (MEG), the resulting data does not directly represent neural activity. Instead, it reflects indirect measurements related to neural activity. To study and model the neural activity, further steps must be taken. For EEG, this process is known as source estimation.

EEG signals arise from a combination of neural activity originating from various brain regions addressed as sources, depicted in figure 2.2. Source estimation, also known as inverse modeling, tackles the task of deciphering the spatio-temporal patterns of neural activity based on these recorded signals. The main objective is to, either pinpoint the regions in the brain that give rise to the observed MEG and EEG signals, an aspect of source estimation that is commonly referred to as source localization, or disentangling the individual contributions from different brain regions in the recorded time-varying signals, the latter is often emphasized as spatio-temporal imaging [4, 30, 71, 51, 69, 68, 70, 41, 74, 48, 53, 54, 7].

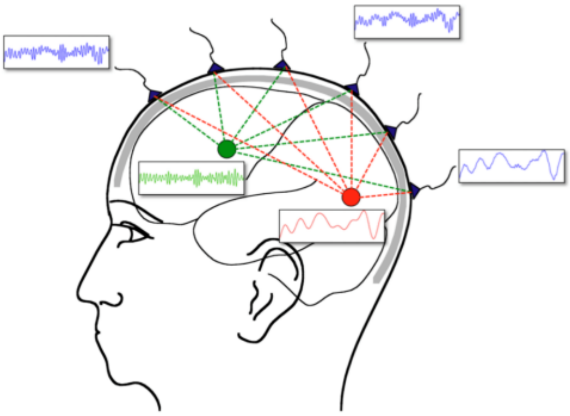

Figure 2.2: EEG electrodes and intracranial sources

2.2.1 EEG Forward Problem

Before source estimation, we must first examine the forward problem, which, in this context, refers to the calculation of the potential detected in the scalp produced by a given source in the brain. To solve the forward problem, we first begin by taking into account that sources can be modeled as dipoles. As mentioned before, the potential detected in the scalp is mainly the synchronized post-synaptic potential generated by pyramid neurons. Due to the structure of pyramid neurons and some other characteristics such currents can be viewed as a pair of monopoles, a current sink and a source, originating a dipole. Being able to describe the sources, we must next construct a head model where to put those sources, taking into account the geometry and conductivity of the different tissues such as the scalp, skull, cerebrospinal fluid and cortex, since the differences between them cause the electric potential generated by the sources to propagate in non-uniform manner. One of the most used head models with an analytical solution is the three layer spherical head model, shown in figure 2.3, where the skull is composed of 3 concentric spheres, each with isotropic conductivity.

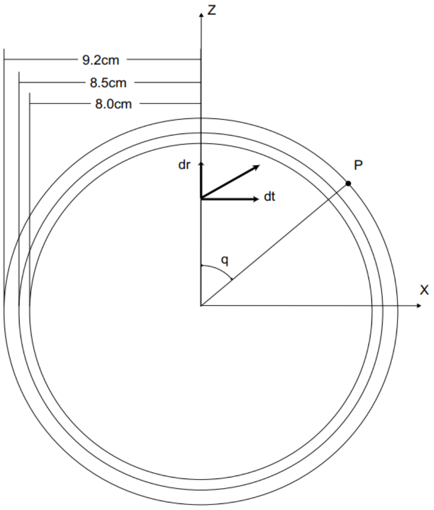

Figure 2.3: The Three layer model (Adapted from Hallez et al. [51]).

For a more precise estimation, realistic head models have been used recently, with more accurate geometric and conductive properties. Analytical solutions were replaced by numerical methods, of which the 2 most common are the Boundary Element Method (BEM) and the Finite Element Method (FEM). BEM is a 2 dimensional approach that is currently the most widely used solution, allowing for the integration of anatomical details of the head and key conductivity characteristics such as those of the brain, skull, and scalp into EEG forward solutions. In BEM the surfaces between various head tissues are modeled by using a mesh of triangles, as shown in figure 2.4, encompassing interfaces like air/scalp, scalp/skull, and skull/brain. Each tissue type must be electrically homogeneous and isotropic, with distinct conductivity values assigned to them.

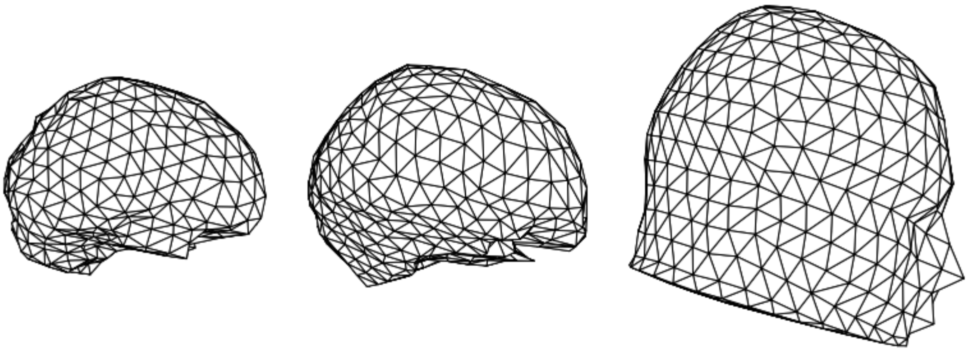

Figure 2.4: Example mesh of a human head used in BEM (Adapted from Hallez et al. [51])

FEM is 3 dimensional and requires the modeling of the entire volume, however it allows for tissues to have an heterogeneous conductivity, even accommodating anisotropic conduction distributions characteristic of the white matter. It is generally assumed to have an higher computational requirement and so less widespread than BEM. Both these numerical techniques allow for the incorporation of the subject's anatomical information using methods such as Magnetic Resonance Imaging (MRI) [71, 51, 4, 30].

Having implemented a head model and taking into account the position of the electrons on the head we can determine the EEG forward solution, by calculating the Gain or Lead Field matrix, which relates the source activity and the electrical potential detected at the scalp.

2.2.2 EEG Inverse Problem

After having calculated the forward solution we can do the opposite, *i.e.* estimate the source activity that would give rise to a certain scalp potential, and solve the inverse problem (hence why source estimation is also known as inverse modeling). Unlike the forward problem, solving the inverse problem does not lead to a unique solution, rather to a large number of source distributions, all resulting in the same scalp potential. The possible distributions are many times unstable and small changes can lead to very different results. Due to these reasons, it is commonly described as an ill-posed problem. This may be due to the fact that the forward problem is mainly focused on geometry and other properties like conductivity, while the inverse problem is focused on making *a priori* assumptions and constraints whether they be purely mathematical, making use of estimation and statistical theory, or based on biophysical or physiological information to narrow down a unique solution.

The classic approach to solve the inverse problem is the localization of a limited number of dipoles. This number should be inferior or equal to the number of electrodes or sensors to allow for a unique solution, and it is further limited by the non-linear complexity of the chosen algorithm. The number of dipole sources cannot, in most cases, be determined *a priori* and using more or less sources may impact estimates, so this approach is more and more frequently replaced by methods that do not require *a priori* constrains on the number of sources, the so called distributed source localization methods.

These methods use a large amount of sources, at least 5000, with their distribution around the brain, designated as the source space, usually constrained to the gray matter or cortex. As the source number is higher than the number of sensors, even taking into account other anatomical and physiological constraints, the solution is undetermined and requires further assumptions. One of the first and most popular approaches is the Minimum Norm Estimation (MNE). In this method, the solution that minimizes the overall current intensity is chosen (the least square solution of the minimum norm), ending up favoring more superficial sources, since these are naturally closer to the sensors. To mitigate this, Weighted Minimum Norm (WMN) methods were introduced. From these a particular method stands out, the Low Resolution Electromagnetic Tomography (LORETA), where the additional constraint of minimizing the Laplacian of the sources is added leading to a smoother and more coherent current density, but also allowing for blurred and over-smoothed solution. Upgraded versions of LORETA have been implemented, namely Standardized Low Resolution Electromagnetic Tomography (sLORETA), and Exact Low Resolution Electromagnetic Tomography (eLORETA). Table 2.1 contains a table listing some software packages that offer EEG source localization tools and the available inverse models. In this thesis, the MNE-Python package [62, 47] was used for source estimation combined with other open-source solutions [4, 69, 68, 70, 41, 74, 48, 53, 54, 7].

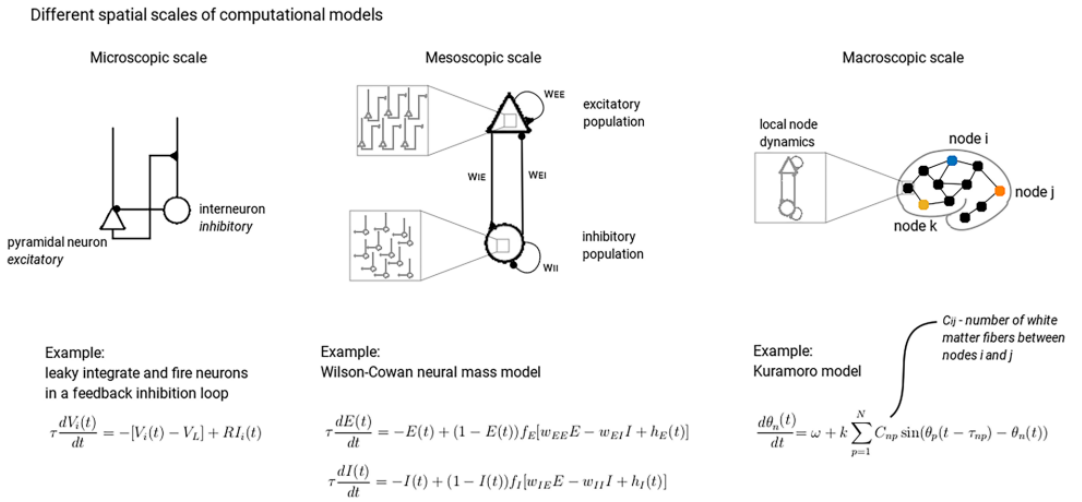

Figure 2.5: Illustration of computational models at the three scales (Adapted from [46])

Table 2.1: Examples of academic and commercial software packages that offer EEG source localization tools (Adapted from Michel et al. [68])

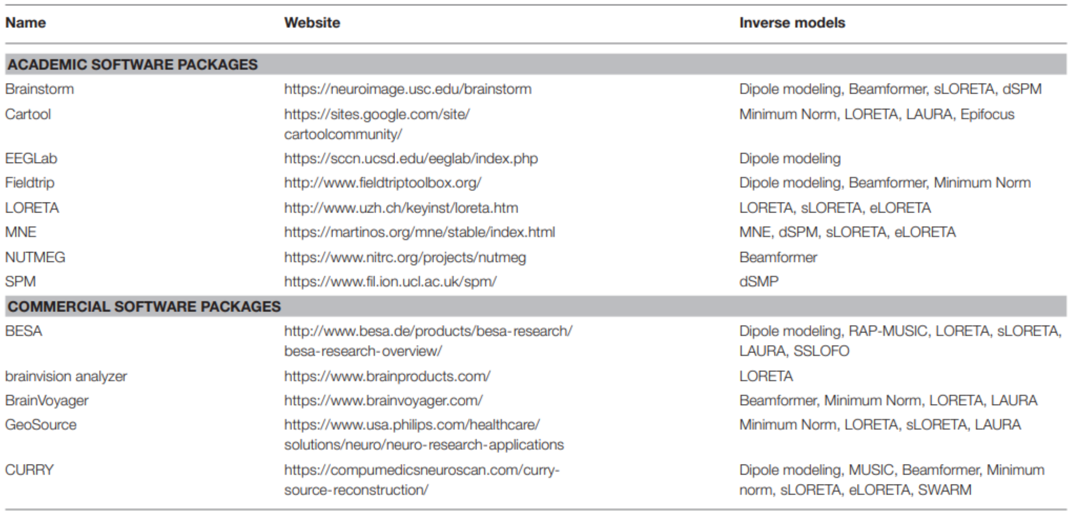

Name	Website	Inverse models
ACADEMIC SOFTWARE PACKAGES		
Brainstorm	https://neuroimage.usc.edu/brainstorm	Dipole modeling, Beamformer, sLORETA, dSPM
Cartool	https://sites.google.com/site/cartoolcommunity/	Minimum Norm, LORETA, LAURA, Epifocus
EEGLab	https://sccn.ucsd.edu/eeglab/index.php	Dipole modeling
Fieldtrip	http://www.fieldtriptoolbox.org/	Dipole modeling, Beamformer, Minimum Norm
LORETA	http://www.uzh.ch/keyinst/loreta.htm	LORETA, sLORETA, eLORETA
MNE	https://martinos.org/mne/stable/index.html	MNE, dSPM, sLORETA, eLORETA
NUTMEG	https://www.nitrc.org/projects/nutmeg	Beamformer
SPM	https://www.fil.ion.ucl.ac.uk/spm/	dSMP
COMMERCIAL SOFTWARE PACKAGES		
BESA	http://www.besa.de/products/besa-research/besa-research-overview/	Dipole modeling, RAP-MUSIC, LORETA, sLORETA, LAURA, SSLOFO
brainvision analyzer	https://www.brainproducts.com/	LORETA
BrainVoyager	https://www.brainvoyager.com/	Beamformer, Minimum Norm, LORETA, LAURA
GeoSource	https://www.usa.philips.com/healthcare/solutions/neuro/neuro-research-applications	Minimum Norm, LORETA, sLORETA, LAURA
CURRY	https://compumedicsneuroscan.com/curry-source-reconstruction/	Dipole modeling, MUSIC, Beamformer, Minimum norm, sLORETA, eLORETA, SWARM

2.3 Computational Models

According to Glomb et al. [46], computational models can be classified into 3 distinct types, depending on the scale of the neuro-physiological activity they attempt to integrate, the level of abstraction and the different aspects of neural systems they replicate (Figure 2.5).

Microscopic models describe individual neurons or micro circuits, composed by populations of interconnected individual neurons.

Mesoscopic models or Mean Field Model (MFM) describe a large population of neurons by its average properties and interactions, such as mean firing rate, and evolution in space and time. It is based on the mean field approximation, a concept from statistical physics for studying large-scale complex systems that are computationally or analytically intractable. Generally, MFM can be divided into two types: Neural Mass Model (NMW), where variables characterizing neural activity depend only on time; Neural Field Model (NFM), where variables are a function on time and space.

Macroscopic models, also called Whole Brain Model (WBM), integrate some or all large-scale sys-

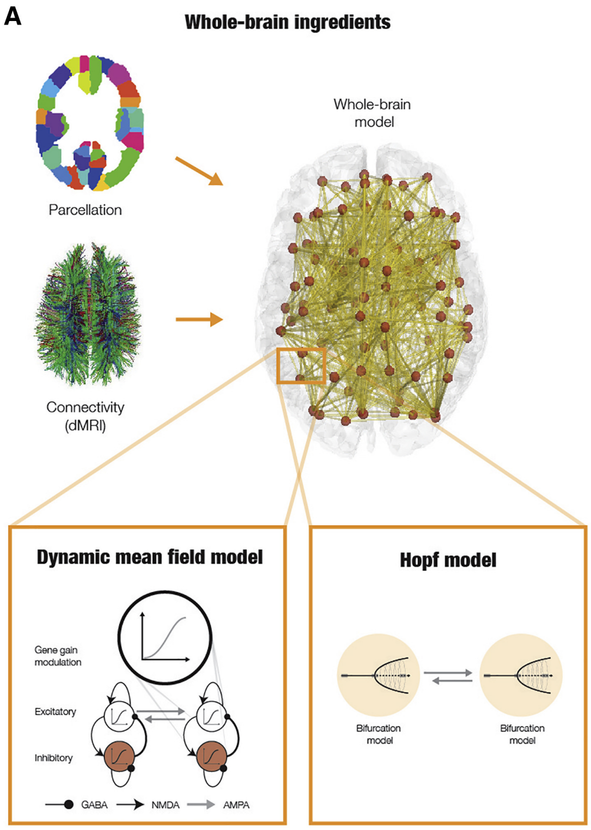

Figure 2.6: Requirements to implement a whole-brain model (Adaped from [59])

tems that support brain function and can, in general, be split into two types: Brain Network Model (BNM), in which the brain is conceptualized as a discrete network of coupled nodes, where each node emulates the local population dynamics and the coupling between reflects the brain connectome (figure 2.6); Large scale NFM, where the entire cortex is treated as a spatially continuous sheet.

An advantage BNM have over NFM is the insertion of crucial medical observables like structural connectivity, functional correlations between different brain regions or the distribution of cell types that could not be expressed in mathematical expressions, allowing the use of patient-specific neuroimaging data (e.g., DTI, fMRI, connectivity) facilitating precision medicine.

Despite the name “Whole-brain” models do not typically model the entire brain, but only parts of it, like the cerebral cortex or a single cortical hemisphere, excluding subcortical regions. The role of subcortical regions in whole brain computational models is not well studied. There are several reasons why subcortical regions have been overlooked or excluded in some computational models. One reason is the complexity of subcortical structures, which consist of diverse nuclei and intricate connections. Modeling and incorporating this complexity into whole brain models can be challenging and computationally demanding. Additionally, the availability and quality of data for subcortical regions are often more limited compared to cortical regions. Techniques like fMRI orEEG have spatial limitations and may not capture subcortical activity as effectively as cortical activity. This data limitation can hinder the inclusion of subcortical regions in computational models. For those reasons, these structures are often excluded from BNM and thus will also be excluded from our study.

However, it is important to note that there has been growing recognition of the significance of subcortical regions in recent years. Researchers are increasingly exploring the role of subcortical structures in whole brain computational models to gain a more comprehensive understanding of brain function.

Advances in imaging techniques, such as Diffusion Tensor Imaging (DTI) and deep brain stimulation, have provided new avenues for investigating subcortical regions and their contributions to brain dynamics. So, while the subcortical regions are not included in this model for the previous mentioned reasons, it can be a future avenue of research [60, 72, 75, 82, 46, 16, 59, 31].

2.4 Brain network models

In the BNM framework, the brain is parcellated into various Regions of Interest (ROI) and conceptualized as a network of nodes, where each node represents the activity of individual ROI and can be influenced by coupling from other brain regions, noise and/or external inputs. In practice, these ROI are defined according to an existing brain atlas also known as a *parcellation*.

Several methods of describing node dynamics exist, according to various degrees of abstractness, ranging from purely phenomenological to biological accurate, the kind of data we want to model, such as resting state, specific activities, epileptic seizures, data from subjects with Alzheimer's. Though it may vary depending on the model and fitting method, the coupling between these nodes is determined mainly by their connectivity, whereas it may be the Structural Connectivity (SC), the Functional Connectivity (FC) or a combination of both the Effective Connectivity (EC).

As aforementioned, the coordinated activity of multiple brain regions underlies various brain functions such as cognition, behavior, and perception. Brain connectivity measures are employed to understand how these regions interact as a network. These measures explore the relationships between brain regions, distinguishing between the different types of connectivity (SC, FC and EC).

Structural Connectivity refers to the physical connections formed by fiber pathways in the brain (eg. white matter tracts) between different regions, the actual anatomical links. SC is measured using Diffusion Weighted Magnetic Resonance Imaging (DWI). From DWI data, a weighted matrix can be derived through tractography, the Structural Connectivity Matrix (SC).

Functional Connectivity, on the other hand, examines non-directed statistical associations and dependencies between brain regions. It focuses on the patterns of activity across regions without considering any causal/implicit relationships between them. Numerous metrics are accessible to assess these dependencies resulting in a Functional Connectivity Matrix (FC).

Effective Connectivity refers to the optimal strengths of connections between regions in a model, which give rise to the observed FC. In this context, we define EC as the amalgamation of anatomical connectivity and connection weights (synaptic conductivity or the effectiveness of synaptic connections). The Effective Connectivity Matrix (EC) represents, as the name implies, the effective connection between distinct brain areas. Besides using EC as a parameter from which we can draw conclusions, it can also be used to fine-tune models, Friston [45].

Recent comparisons between connectomes, generated using diffusion tractography-based techniques and neuroanatomical tracer studies, have revealed that even state-of-the-art tractography methods may fail to detect all neuroanatomical pathways and their corresponding connection strengths. Still, many of these issues can be overcame with the use of model-based estimates of the effective connectivity, where measures of Functional Connectivity can enhance and supplement the anatomical Structural Connectivity.

As explained in section 2.1, while brain activity can be interpreted and studied at several scales, at the scale BNMs are designed, brain activity is mostly resulting from synchronous activation of neuron populations across brain regions. Hence, the brain activity associated with different brain states is characterized by the Functional Connectivity and BNMs generally attempt to reflect this metric.

The typical modeling approach, of which an example is shown in figure 2.7, consists of simulating data and computing a certain feature, normally the FC, and then adjusting the model parameters to enhance correlation between the empirical and simulated data. A fitted model can then be used to test several hypotheses, or the modeled parameters studied to get a better understanding of the modeled brain state. There are several successful clinical applications such as locating the origin of epileptic seizures in the brain, predict the chronic effects resulting from traumatic brain injuries and many more [60, 72, 75, 82, 46, 16, 59, 31].

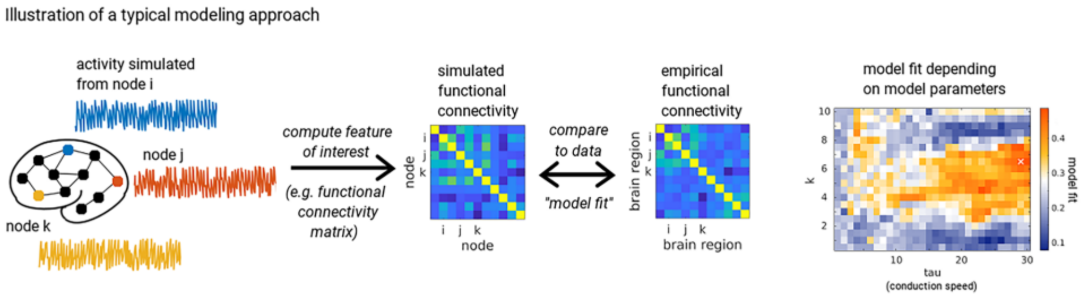

Figure 2.7: Typical modeling approach using FC (Adapted from [46])

2.5 Functional Connectivity Metrics

To compute the Functional Connectivity the chosen metrics were Coherence (COH), Phase-Locking Value (PLV) and the Pearson Correlation Coefficient (PCC).

The Coherence, $C_{xy}(f)$ between two signals x and y (in this case the sources estimate time courses of 2 different nodes, i and j) is a real value between 0 and 1 showing the degree with which two signals are linearly related. It is given as the cross power spectrum $G_{xy}(f)$ divided by the square root of the product of the two auto power spectra, $G_{yy}(f)$ and $G_{xx}(f)$, averaged across epochs and frequency band f, as shown in Equation 2.1 [6, 26, 66, 86].

$$C_{xy}(f) = \frac{|G_{xy}(f)|}{\sqrt{G_{xx}(f) \times G_{yy}(f)}} \tag{2.1}$$

The Phase-Locking Value (PLV) between two signals x and y is a real value between 0 and 1 representing the degree to which the signal phases are synchronized. It is close to 1 when the phase difference is constant and closer to 0 when the phase difference varies. It is given as the averaged Φ_{xy}, $\Phi_{xy} = e^{-i\Delta\phi_{xy}}$ across trials and frequency bands as is shown in equation 2.2, with $\Delta\phi_{xy}$ being the phase difference between signal x and y, ($\Delta\phi_{xy} = \phi_x - \phi_x$).

$$PLV_{xy} = \frac{1}{N}\sum_{n=1}^{N} e^{-i\Delta\phi_{xy}} \tag{2.2}$$

The Phase-Locking Value is similar to Coherence. While Coherence shows how two signals are related taking into account both the phase and the amplitude of the signal, the Phase-Locking Value considers only the phase.

As there are many methods of obtaining the signal's phase, there are also many ways to calculate the Phase-Locking Value. Similarly to Coherence, it can be can be obtained with the cross power spectrum, $G_{xy}(f)$, as the cross spectrum includes both magnitude and phase information between the two signals at each frequency. Dividing it by its magnitude ,$\Phi_{xy} = \frac{G_{xy}(f)}{|G_{xy}(f)|}$ removes the magnitude from the equation leaving only the phase. Using this method the PLV is a purely frequency dependent metric, as show in equation 2.3. This is the method implemented in MNE-Python and what is referred to as "PLV".

$$PLV_{xy}(f) = \frac{1}{N}\sum_{n=1}^{N}\frac{G_{xy}(f)}{|G_{xy}(f)|} \tag{2.3}$$

Another method used to calculate the Phase-Locking Value is using the instantaneous phase $\phi(t)$. After band passing the signal, $x(t)$, and applying the Hilbert transform $H\{x(t)\}$ the analytical signal $z(t)$, shown in equations 2.4, can be obtained.

$$z(t) = x(t) + jH\{x(t)\} \tag{2.4}$$

$$z(t) = A_x(t)e^{\phi_x(t)} \tag{2.5}$$

Representing the analytical signal in its polar form, 2.5 we have the argument, $argz(t) = \phi_x(t)$, corresponding to the instant phase and the magnitude, $|z(t)| = A_x(t)$, corresponding to the instant amplitude or the amplitude envelope.

This instant phase can be used as an alternate method to calculate the PLV. Amplitude can also be used as an FC metric, specifically the correlation between amplitude envelopes (normally the Pearson Correlation Coefficient, shown in equation 3.6), referred to as the Envelope Functional Connectivity (Envelope). These 3 FC metrics were chosen as they are the most commonly used and show high correlation between empirical and simulated data [61, 8, 9, 20, 58, 24, 34, 23, 42].

Chapter 3

Methods and Materials

3.1 EEG Data and pre-processing

The EEG data collection and pre-processing tasks were performed at Instituto de Biofísica e Engenharia Biomédica (IBEB) under the scope of a project dedicated to measure the efects of Transcranial Direct Current Stimulation (tDCS) in FC measured by EEG, during Motor Imagery (MI) and Motor Execution (ME). This study is described in greater detail in Silva [84]. Briefly, data was acquired in 21 healthy right-handed individuals (mean age 21.25 ± 1.97 years; 13 females), with a sampling rate of 500 Hz and following the experimental design in figure 3.1. The subjects underwent 3 trials of which only 2 will be used.

During trial 1, 3-minutes of open-eyes resting state activity (Resting State (REST)), while avoiding mind-wandering, are recorded. During trial 2, visual stimuli were presented in a random manner corresponding to 5 different tasks : motor execution of the left or right hand (Motor Execution Left (MEL),Motor Execution Right (MER)), which consists of opening and closing the respective hand consecutively; motor imagery with the left or right hand (Motor Imagery Left (MIL),Motor Imagery Right (MIR)), which consists of imagining the motor execution of the respective hand; rest in between tasks. Each stimulus appears on screen during around 5 seconds.

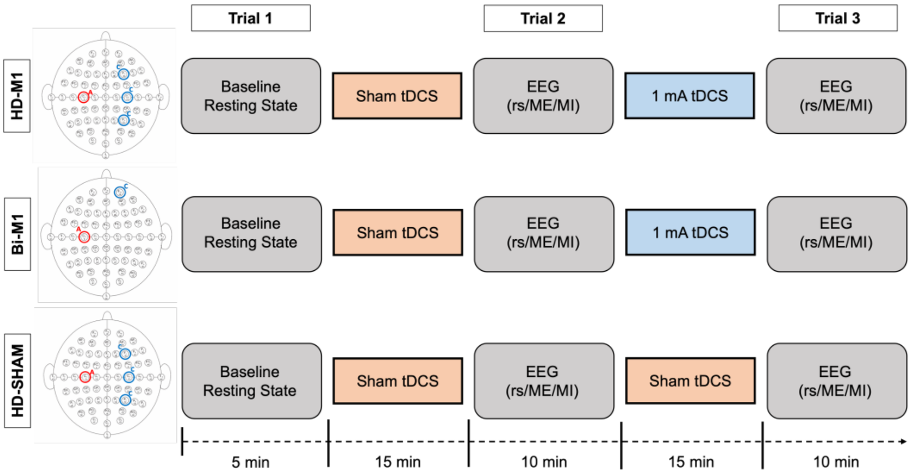

Figure 3.1: Experimental Design from Silva [84]. Three groups (HD-M1, Bi-M1 and HD-SHAM) follow the same protocol - a first trial of baseline resting state; a second trial with visual stimuli for resting state, ME and motor imagery MI tasks; and a third one following the same paradigm as the second trial. Between each trial there is a moment of tDCS (sham or active)

3. METHODS AND MATERIALS

Only Trial 2 data is used as Trial 1 was not needed and Trial 3 occurs after tDCS. While that section is not explored on this thesis it would be very interesting to model in future studies. The EEG device used to collect the data had 64 recording electrodes distributed according to the 10-10 international system, e.g. 3.2. Four of these positions were used only for stimulation and did not have an EEG recording ($C3$, $C4$, $F4$, $P4$, $Fp2$).

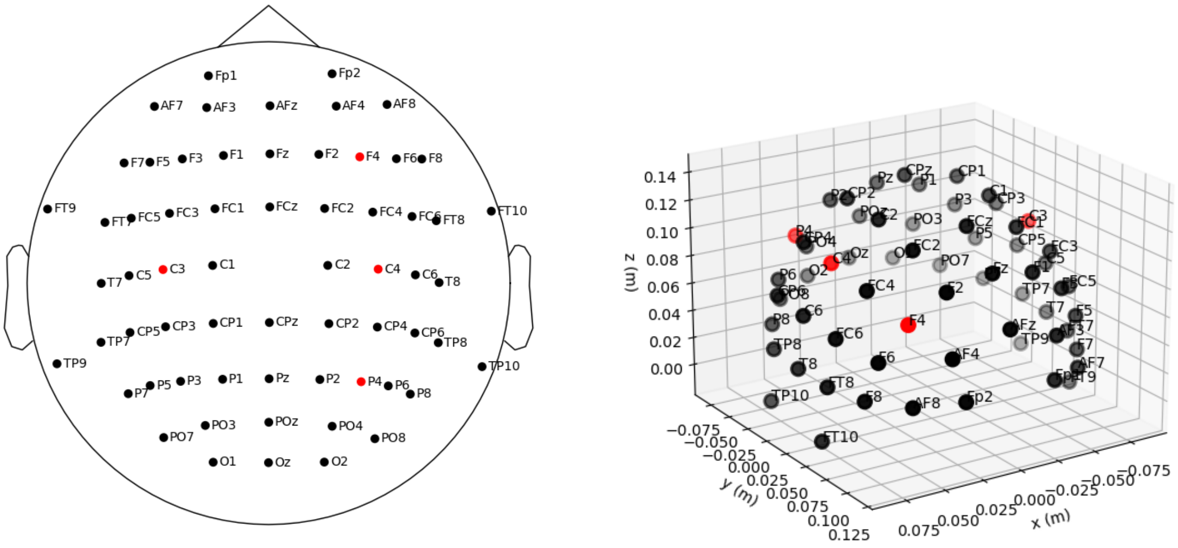

(a) 2D sensor positions

(b) 3D sensor positions

Figure 3.2: Sensor positions (2D projection 3.2a and 3D 3.2b). The red channels are the rejected channels for this particular subject after pre-processing, since these were used of stimulation.

The EEG data used was filtered with a band-pass with cutoff frequencies of 1 and 40 Hz. Independent Component Analysis (ICA) was applied to remove physiological artifacts such as ocular and heartbeat artifacts. The data was then split into multiple 4 second (2000 points) epochs, each one corresponding to one of the five tasks performed (REST; MER; MEL; MIR; MIL) Silva [84]. Figures 3.3 and 3.4 show an example of the epochs and spectral distribution for a specific subject.

All tasks involved in pre-processing, inverse modelling and some connectivity calculations are done on MNE-Python [62, 47].

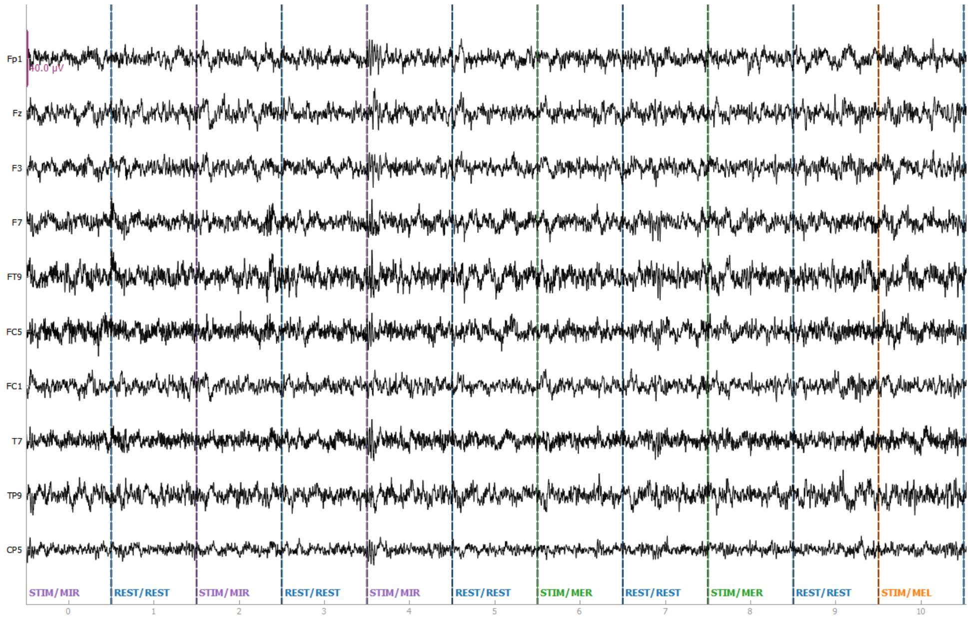

Figure 3.3: Example of an EEG recording divided in epochs according to each task

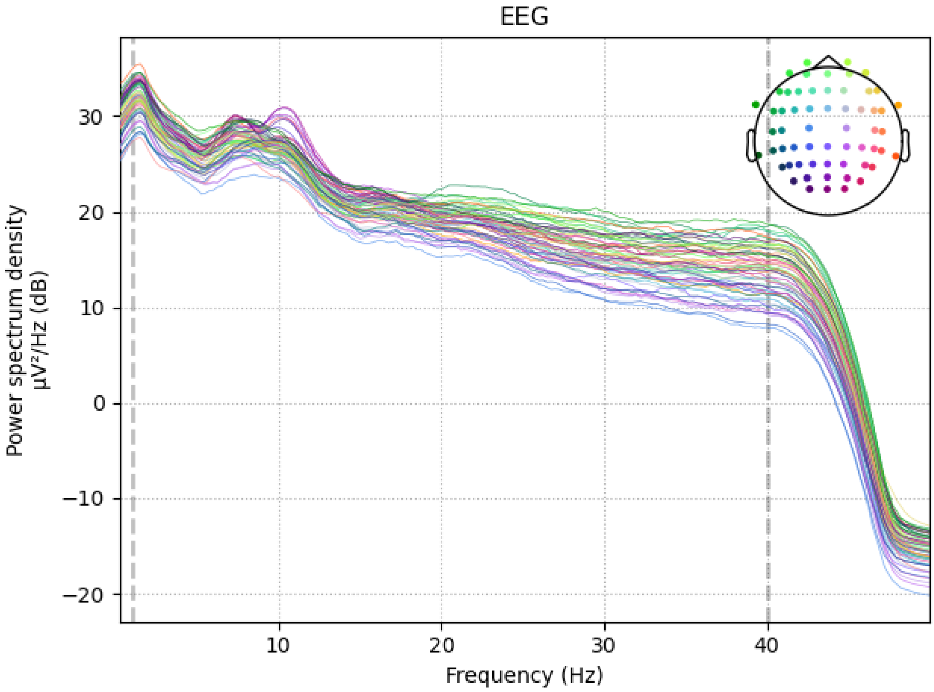

Figure 3.4: Example of a power spectral distribution of the EEG signals recorded in all available sensors in one subject.

3.2 Forward Model

After processing the EEG data, the forward model was set up. As explained in section 2.2.1, the forward model requires a head model, a source model and the EEG sensors locations. It was not possible not construct a head model for each subject, due to the lack of the subjects MRI. So the "fsaverage" template, Fischl et al. [44], an average subject template built from the combination of 40 MRI scans of real brains was chosen. This template was developed for the FreeSurfer software, Fischl [43], and later made available on MNE-Python along with an already pre-computed source space and BEM head model, constructed base on "fsaverage" template.

The BEM head model, shown in figure 3.5, contains 3 surfaces, the inner skull, outer skull and scalp, with the respective conductivities being 0.3, 0.006 and 0.3 S/m, as these are the default MNE-Python values [47] (also used in Silva [84]). The effect of the conductivity values, the ratio between skull and soft tissue conductivity and other possible conductivity values are explored in Hallez et al. [51]. The source space, shown in figure 3.6, defines the position and orientation of every possible source point. This space was recursively subdivided into icosahedra, ending up with 10242 source points in each hemisphere.

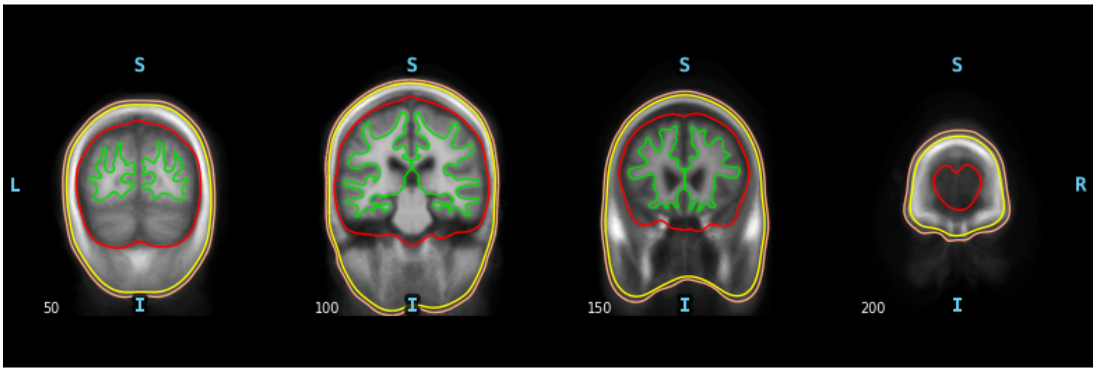

Figure 3.5: Slices number 50, 100, 150 and 200 of the BEM model's outer boundaries of scalp, outer and inner skull and white/grey matter interface are represented by orange, yellow, red and green contours, respectively, as well as the fsaverage brain.

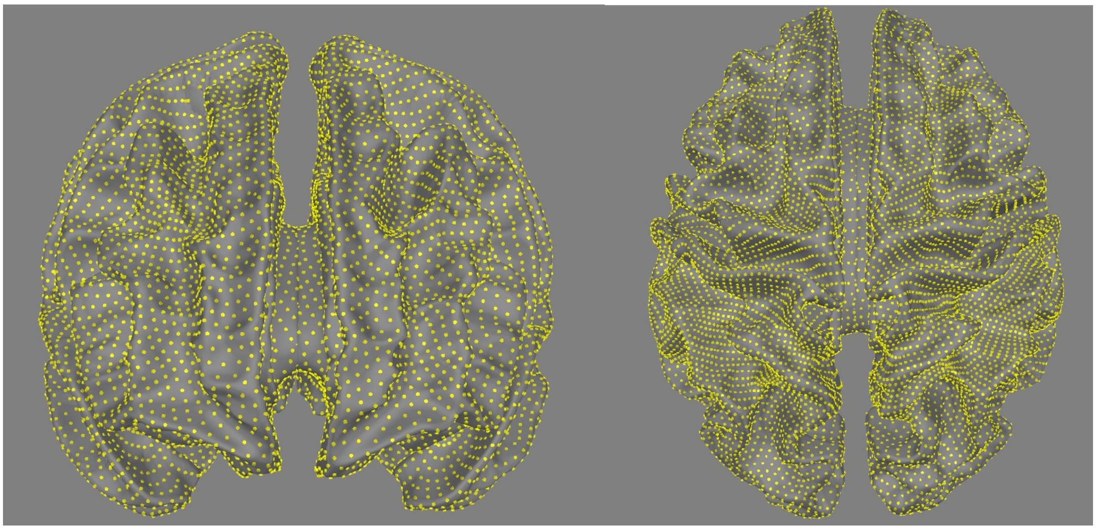

Figure 3.6: Source space distributed along fsaverage brain with 10242 source points in each hemisphere.

After setting the BEM model and source space, the last step consists of inserting the sensor information and aligning their position with our BEM, a procedure known as coregistration. This can be done in an automated fashion, first by fitting the MRI fiducials and then refining the fit with the Iterative Closest Point (ICP) algorithm, to minimize the median distance between the electrodes and the head surface, producing a transformation file. The final product can be seen in figure 3.7, allowing for the computation of the forward solution, a lead field gain matrix of 63 sensors x 61452 dipoles, $n_p = n_s \times n_h \times n_o = 10242 \times 2 \times 3$ with n_p = number of dipoles, n_s = number of sources in each hemisphere, n_h = number of hemispheres, n_o = number of coordinates (as the source orientations are unconstrained, each source corresponds to 3 dipoles placed orthogonally to form a Cartesian coordinate system).

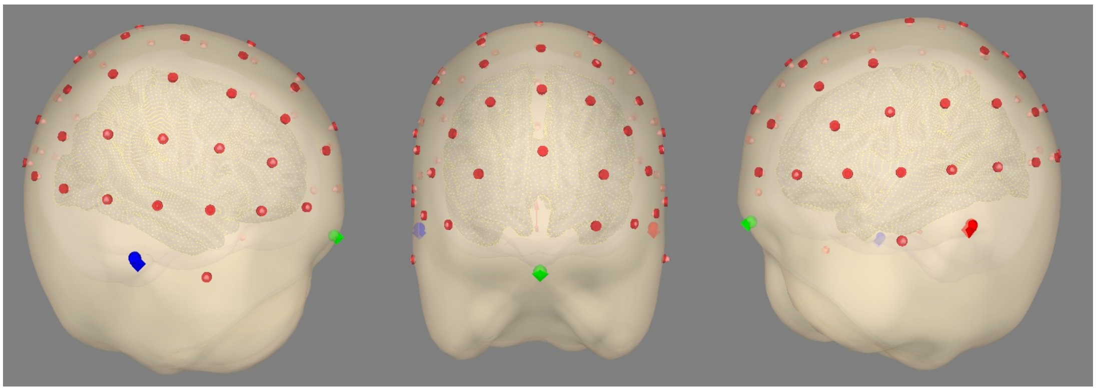

Figure 3.7: Complete head model with red, blue and green vectors corresponding to the fiducials, red spheres to the electrode positions, with a median distance to the scalp of $1.81mm$, red disks the electrodes' projection on the scalp (positions that will be used on forward modeling), the inner and outer skull surfaces, source space and fsaverage brain

3.3 Source Estimation

With the forward model implemented, the inverse model can be calculated in MNE-Python. First, a noise covariance matrix is calculated to provide an estimation of the signal noise. The definition of noise depends on the paradigm: in this work we considered resting state brain activity with eyes open. The last 250 *ms* of the resting state intermission between each task were used to calculate the covariance matrix for each of the subjects, according to Silva [84]. The estimated covariance can be numerically unstable and introduce bias based on the number of samples, thus it should be regularized. There are many methods to regularize the covariance matrix. MNE-Python provides an automated manner, using cross-validation to choose the appropriate regularization implemented, Engemann et al. [40]. This is done by determining how well the covariance matrix whitens the data using the negative log-likelihood of unseen data. The final results are shown in figure 3.8: the whitened baseline signal should follow a multivariate Gaussian distribution and be between -1.96 and 1.96, representing a 95% confidence interval, at a given time sample while the expected value for the Global Field Power (GFP) is 1.

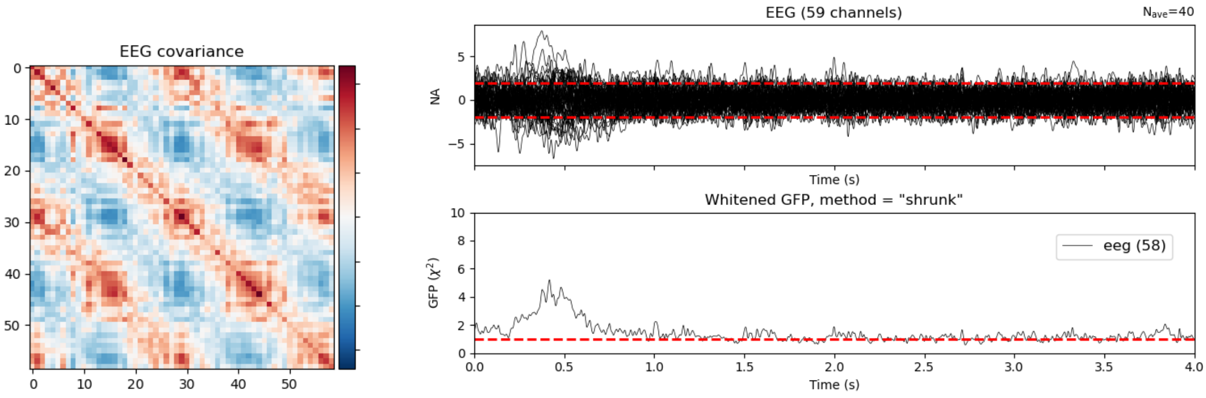

(a) Covariance matrix

(b) Whitened evoked signals for each channels and the whitened GFP

Figure 3.8: 3.8a Covariance matrix and 3.8b its effects on the whitened signal and GFP for best method found for the considered 59 EEG channels

With the covariance matrix calculated, we can now perform the source estimation. For this purpose, there are some important parameters to take into account. First, the orientation: due to symmetry and geometry, the net sum of the direction of the postsynaptic currents in the pyramidal cells are generally perpendicular to the cortical surface, as the parallel components cancel each other out, Ahlfors et al. [4]. Considering this, it is not unusual to constrain the source orientation as perpendicular to the cortical surface, however EEG and MEG have low spatial resolution: even in a small volume the orientation of a source relative to the cortical surface can change drastically. This also exacerbates possible errors in the alignment of the MEG/EEG and MRI coordinate frames. To minimize this problem, a "loose" orientation constraint can be added in such a way that other directions are also taken into account but with less weight, Lin et al. [63]. This constraint was also applied with eLORETA, similarly to Silva [84]. Figure 3.9 shows an example plot of the fsaverage brain with the vector source estimates at a specific point in time. While vectors are shown here, for further analysis only their magnitude will be considered.

Table 3.1: Anatomical labels for the 68 regions in the Desikan-Killiany parcellation. The two region numbers per line refer to right and left hemisphere respectively.

Region Number	Region Name
1, 35	lateral orbitofrontal
2, 36	pars orbitalis
3, 37	frontal pole
4, 38	medial orbitofrontal
5, 39	pars triangularis
6, 40	pars opercularis
7, 41	rostral middle frontal
8, 42	superior frontal
9, 43	caudal middle frontal
10, 44	precentral
11, 45	paracentral
12, 46	rostral anterior cingulate
13, 47	caudal anterior cingulate
14, 48	posterior cingulate
15, 49	isthmus cingulate
16, 50	postcentral
17, 51	supramarginal
18, 52	superior parietal
19, 53	inferior parietal
20, 54	precuneus
21, 55	cuneus
22, 56	pericalcarine
23, 57	lateral occipital
24, 58	lingual
25, 59	fusiform
26, 60	parahippocampal
27, 61	entorhinal
28, 62	temporal pole
29, 63	inferior temporal
30, 64	middle temporal
31, 65	banks of superior temporal sulcus
32, 66	superior temporal
33, 67	transverse temporal
34, 68	insula

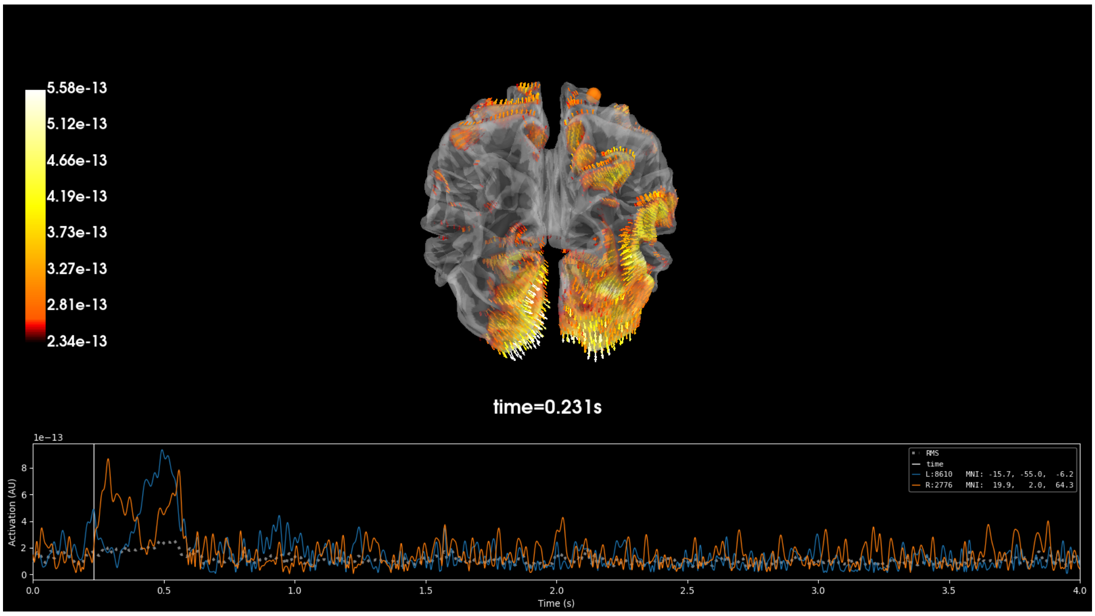

Figure 3.9: Example of the source estimation vectors at a certain time point. The color scale represents the intensity of the neural source activations.

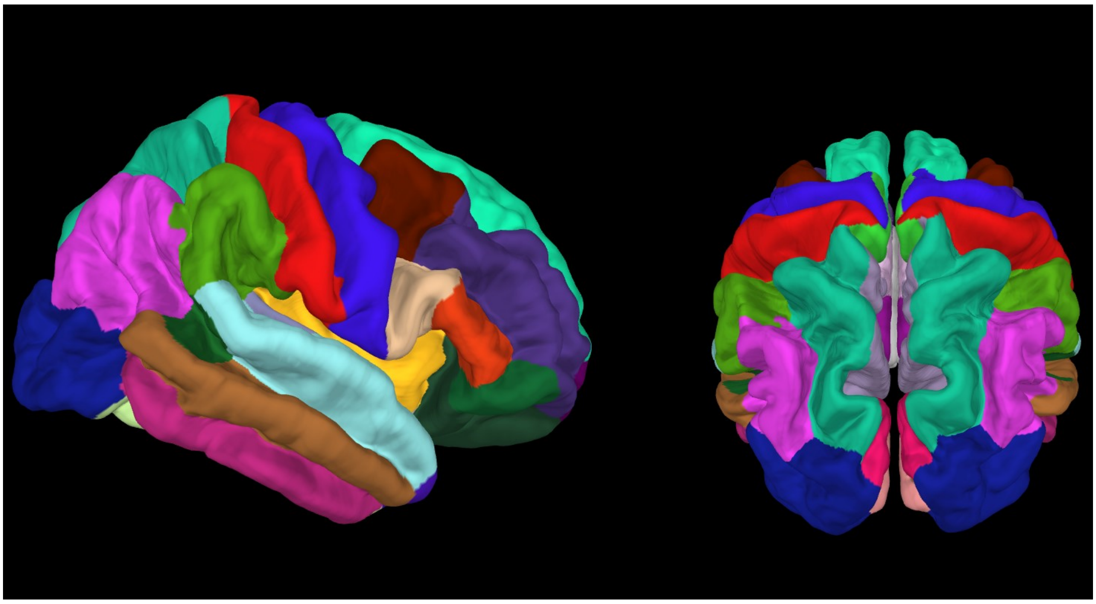

Figure 3.10: Desikan-Killiany parcellation atlas plotted onto the fsaverage brain

After performing source estimation we can now transition the data onto a brain atlas parcellation. The Desikan-Killiany parcellation atlas, Desikan et al. [38] was chosen, as it is the one of the most commonly used in the bibliography and is available in MNE-Python. Figure 3.10 represents the chosen parcellation, plotted onto the fsaverage brain. Table 3.1 indicates the regions and regions labels in figure 3.10. To extract each label time course, the mean flip method is used: the dominant direction of source space normal vector orientations within each label is found, applying a sign-flip to time series at vertices whose orientation is more than 90° (different from the dominant direction) and then averaging across vertices at each time point within each label.

3.4 Structural Connectivity

The structural connectivity data set was taken from Kerepesi et al. [57], a database that includes various connectomes generated from MRI scans from the Human Connectome Project (HCP). The dataset chosen here is the 86 nodes set, which corresponds to the Desikan-Killiany parcellation, along with some extra nodes belonging to sub cortical regions, containing the brain graphs of 1064 different subjects. The relevant attributes from the dataset along with their function on a brain graph are indicated on table 3.2, with the region name and number being the same as in table 3.1 and the edges corresponding to structural connectivity metrics: fiber length mean - mean of the fiber lengths (in millimeters); FA mean - mean of the fractional anisotropies of the fibers; number of fibers. Averaging the 1064 brains we obtain 3 SCs shown in figure 3.11.

attribute name	graph component
number of fibers	edge
FA mean	edge
fiber length mean	edge
hemisphere	node
region name	node
region number	node
z position	node
y position	node
x position	node

Table 3.2: Relevant attributes from the braingraph dataset and their role on the graph

Figure 3.11: SC for the braingraph dataset averaged according to (a) FA mean, (b) number of fibers and (c) fiber length mean

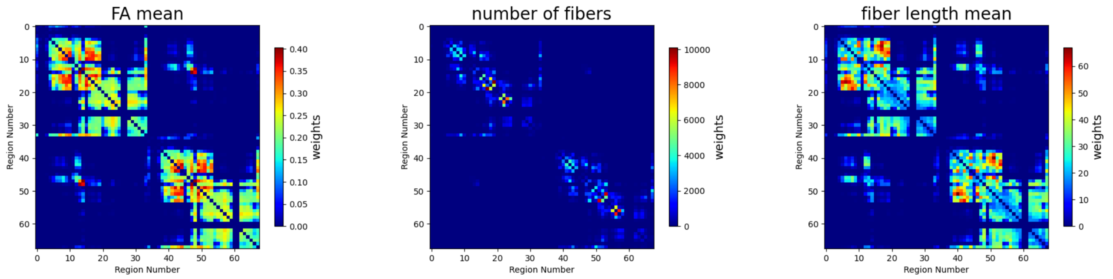

(a) FA mean between each region

(b) number of fibers between each region

(c) fiber length mean between each region

Acknowledgments: Data was provided in part by the Human Connectome Project, WU-Minn Consortium (Principal Investigators: David Van Essen and Kamil Ugurbil; 1U54MH091657) funded by the 16 NIH Institutes and Centers that support the NIH Blueprint for Neuroscience Research; and by the McDonnell Center for Systems Neuroscience at Washington University."

3.5 Local Dynamics Model

The BNM employed in this thesis consists of 68 interconnected nodes, obtained through the aforementioned parcellation method. The overall dynamics of this BNM model arise from the interactions between the local dynamics of individual nodes, which are described by the normal form of a supercritical Hopf bifurcation and can be coupled through either the Structural Connectivity Matrix or the Effective Connectivity Matrix.

Traditionally, models of brain signals have been categorized into two main families: noise-based models and oscillatory-based models. Hopf bifurcation-based models bridge the gap between these two approaches by integrating the principles of both noise-based and oscillatory-based models. They are built upon the normal form of a Hopf bifurcation. In these models, the behavior of the signal generator undergoes a sudden change after surpassing a critical value of one or more parameters. Specifically, a Hopf bifurcation is the point at which a system that initially exhibits stable fixed point behavior loses its stability and begins to oscillate. By incorporating Hopf bifurcation, these models allow for transitions between asynchronous noise activity and oscillatory behavior. This characteristic makes them suitable for reproducing empirical data observed in EEG, MEG or fMRI.

Figure 3.12 and table 3.3 show multiple models used to describe local brain dynamics. The Hopf model was chosen as it is one of the more abstract models and easier to understand, implement and study. Additionally, it has been used to successfully reproduce several aspects of Functional Connectivity and is widely used in various studies. It is also highly relevant as several of these studies focus on themes like resting state activity, transitions between sleep and wakefulness, mechanistic differences between brain states and even Parkinson's disease and Alzheimer's disease, ensuring the model feasibility for future works implementing this network. Besides availability and widespreading, one of the reasons for choosing the Desikan-Killiany parcellatio is that it is frequently used together with the Hopf model [33, 77, 35, 88, 56, 39, 36, 87, 32, 49, 34, 37, 83, 78, 21, 55] .

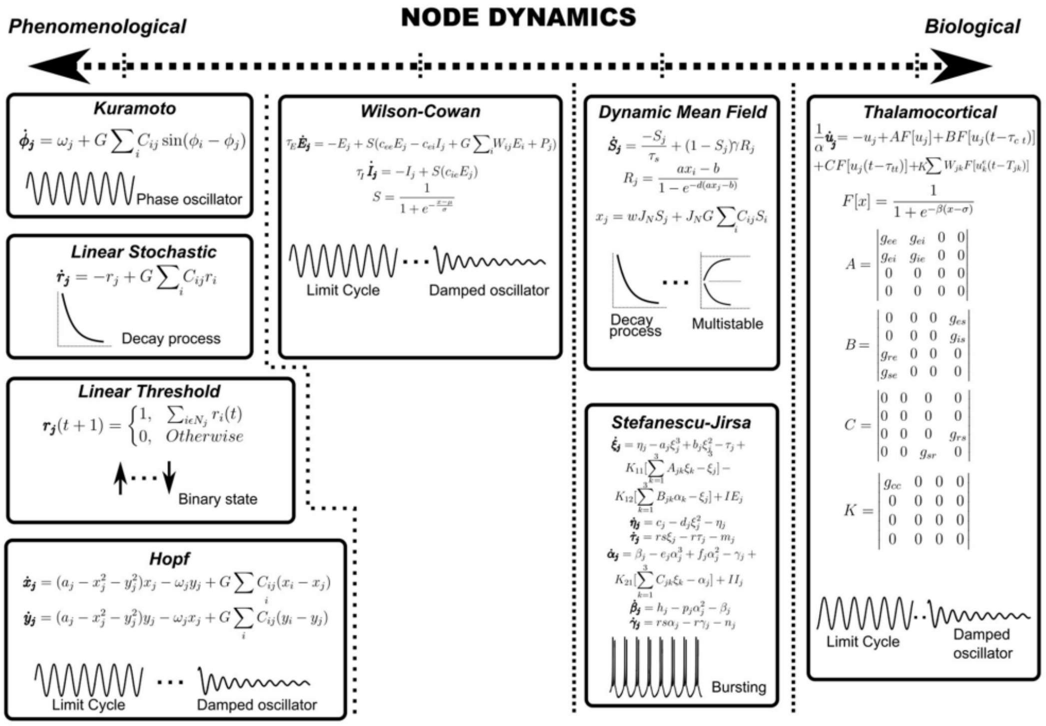

Figure 3.12: Node dynamics models categorized on an axis according to phenomenological or biological validity (Adapted from Pathak et al. [75]))

Table 3.3: Comparison between different models of whole-bran resting-state activity (Adapted from Cabral et al. [21])

	Biophysical properties	Dynamical regime			Model Validation		
		Uncoupled units	Coupled units	Origin of slow fluctuations	Spatial Static FC	Temporal FC Dynamics	Spectral Envelope FC
Spiking Neurons	Integrate-and-fire excitatory and Inhibitory neurons (AMPA, NMDA, GABA receptors)	Fixed point	Multi-stability between Fixed Points	At the brink of Multi-stability	Yes	Yes	?
Conductance-based	Membrane potential of E and I pools controlled by ionic conductance and NMDA receptors	Chaotic with oscillations	Chaotic (range of frequencies)	Intermittent self-organization from chaos	Yes	Yes	Yes
Neural Field	Coupled Excitatory and Inhibitory pools of neurons	Limit-Cycle	Limit-Cycle (arbitrary frequencies)	Connectome-specific Harmonics	Yes	?	?
FitzHugh-Nagumo	Membrane potential of neuronal pool with recovery time-constants	Fixed Point	Fixed point or Limit-cycle (10Hz)	Vicinity of a Supercritical Bifurcation - Damping	Yes	?	Yes
Wilson-Cowan	Coupled Excitatory and Inhibitory pools of neurons	Limit-Cycle (40Hz)	Limit-Cycle (40Hz)	Meta-stable Chimera Synchronization	Yes	?	?
Kuramoto γ Oscillators	Oscillator representing synchronous neuronal firing	Limit-Cycle (40, 60Hz)	Intrinsic Limit-cycle (γ) or Collective Limit-cycle (α,β)	Meta-stable Chimera Synchronization	Yes	Yes	Yes
Hopf Model With Fast Oscillations	Bifurcation representing Synchronous vs Asynchronous neuronal firing	At bifurcation Fixed Point to Limit-Cycle	Fixed point or Limit-Cycle (2-30Hz)	Vicinity of Supercritical bifurcation & Meta-stable Synchronization	Yes	Yes	Yes
Dynamic Mean Field	Synaptic input currents and firing rates	Fixed point	Multi-stability between Fixed Points	At the brink of Multi-stability	Yes	Yes	No
Kuramoto Ultra-slow Oscillators	Oscillator representing BOLD fluctuations	Limit-Cycle (0.1Hz)	Limit-Cycle (0.05Hz)	Meta-stable Chimera Synchronization	Yes	Yes	No
Hopf Model With Ultra-Slow Oscillations	Slow-oscillations representing BOLD fluctuations	At bifurcation Fixed Point to Limit-Cycle	Fixed point or Limit Cycle (0.04-0.07Hz)	Vicinity of a supercritical Bifurcation & Meta-stable Synchronization	Yes	Yes	No
Linear Stochastic Model	Noise representing firing rate deviations	Fixed Point	Fixed Point	Noise deviations around equilibrium	Yes	No	No
Spatial Autoregression	Structured Noise	-	-	-	Yes	No	No

For the Hopf model, we can define ω as the intrinsic frequency of each node, a as the local bifurcation parameter, η as additive Gaussian noise with standard deviation $\beta = 0.02$. The temporal evolution of the activity, z, in node j is given in the complex domain as:

$$\frac{dz_j}{dt} = z(a_j + i\omega_j - |z_j^2|) + \beta\eta_j(t) \tag{3.1}$$

where

$$z_j = \rho_j e^{i\theta_j} = x_j + iy_j \tag{3.2}$$

The normal form of the supercritical Hopf bifurcation model has a bifurcation at $a_j = 0$. For $a_j < 0$ there exists a stable fixed point at $z_j = 0$, which corresponds to a low activity noisy state due to the additive Gaussian noise, and for $a_j > 0$, the local dynamics shows a stable limit cycle oscillation with frequency $f_j = \frac{\omega_j}{2\pi}$. The whole-brain dynamics are then described by the following set of coupled equations:

$$\frac{dx_j}{dt} = [a_j - x_j^2 - y_j^2]x_j - \omega_j y_j + G\sum_i C_{ij}(x_i - x_j) + \beta\eta_j(t) \tag{3.3}$$

$$\frac{dy_j}{dt} = [a_j - x_j^2 - y_j^2]y_j + \omega_j x_j + G\sum_i C_{ij}(y_i - y_j) + \beta\eta_j(t) \tag{3.4}$$

where G is a global coupling strength parameter that scales the adjacency connectivity matrix C, a $n \times n$ square matrix where n is the number of nodes according to the parcellation, n equaling 68 in this case. C_{ij} would be the value that couples nodes i and j, normally the Structural Connectivity (SC_{ij}) or the Effective Connectivity (EC_{ij}) as mentioned. x, corresponding to the real component of z, Re(z), represents the simulated source activity.

When the bifurcation parameter (a) of a node is negative, the model is in the noisy regime and it indicates that the node activity is random or asynchronous (asynchronous firing of neurons). On the other hand, when a is positive the model is in the oscillating regime and the node generates stable oscillatory dynamics (synchronized firing of neurons). Nodes with non-zero a are less responsive to environmental conditions since they are either generating noise or locked into a stable oscillatory pattern. This can be seen on figure 3.13. With a close to zero, or the bifurcation, the model is in the fluctuating regime. Here the generated noise is enough to trigger some oscillations but not in a sustained fashion as in the oscillating regime. This regime represents an adaptive brain that can quickly switch between states and most studies found that it best models a resting state brain [36, 35, 78, 56, 34].

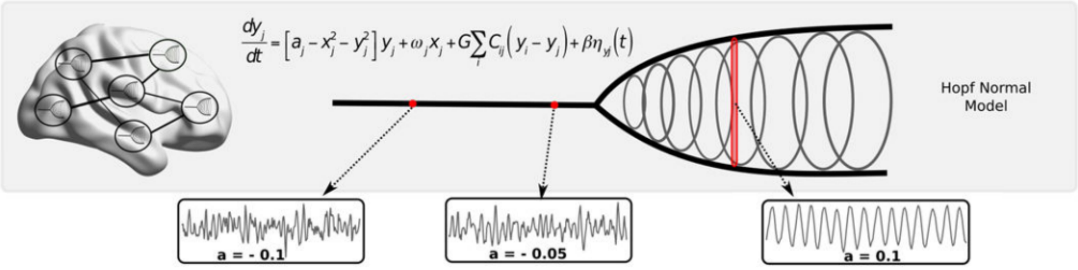

Figure 3.13: Effect of bifurcation parameter, a (adapted from Demirtaş et al. [36])

3.6 Model Fitting

The goal of fitting the model is adjusting the parameters a, G and C to align and maximize the similarity between model simulated and empirical data. The metrics used to fit the model other than the already explained Functional Connectivity are the coherence and metastability along with the PMS calculated using LEiDA, explained further ahead.

While it is possible to explore all parameters extensively in a grid like fashion this is a very computationally demanding task as such the bifurcation parameter a is typically set homogeneously (the same for all nodes) near the bifurcation point $(a = 0)$. The a parameter more is often explored in the context of pathological alterations in brain dynamics. In the present study, a was not extensively optimized, as it was not anticipated to play a significant role in healthy task-based dynamics. It is possible for a to be assigned heterogeneously across nodes. Heterogeneous tuning typically requires adjusting each region based on its Power Spectral Density (PSD) profile. This approach is not practical here due to the frequency limitations of the Hopf model, which can only capture oscillatory dynamics within a narrow range (typically ± 2 Hz), Deco et al. [34].

The Structural Connectivity Matrix, C, serves as the anatomical scaffold of the model and can be further optimized into an Effective Connectivity Matrix to enhance the fit between model and data.

However, apart from such optimizations, the global coupling parameter G is the primary control knob for regulating network dynamics and achieving correspondence with empirical data. As such, parameter exploration is primarily focused on tuning G.

EEG data is normally split into separate frequency bands for analysis. The bands of interest for this work regarding motor-based tasks are the alpha (8-12 Hz) and beta split into lower beta (12-16 Hz) and middle beta (16-20 Hz), matching well with the Hopf model's simulating range (Schomer et al. [80]).

In parameter explorations, it is common to find an interval of values that maximize the similarity between metrics. The ideal behavior is a local minimum or maximum where it is possible to narrow down the best value. For this reason a wide variety of metrics are used.

The modeling approach will then be: G parameter exploration across FC metrics, frequency bands, SC and tasks with a at the bifurcation. After the best G is determined, an exploration of a follows at that G value. The EC is then fitted and the previous steps repeated along with LEiDA and coherence and metastability, explained further ahead, to create the final model for every FC metric, frequency band and brain state.

3.6.1 Functional Connectivity

In most studies and articles, Functional Connectivity is fitted for or used in the fitting process [31, 59, 72, 16, 75, 60, 46]. The most direct, first approach method at fitting for Functional Connectivity is a parameter space exploration to determine the parameters that maximize similarity between empirical and simulated signals. The problem with this method, and the reason why it can only be used as a first approach, is that it is difficult to find unique solutions. These problems can be solved by using supplementary fitting methods, which are explained in further detail in the next sections, or by using higher computational effort and statistical analysis.

To evaluate the similarity between the simulated and empirical Functional Connectivity Matrix, multiple metrics were used: Euclidean Distance (ED), Structure Similarity Index (SSIM), Distance Correlation (dCor), and Pearson Correlation Coefficient (PCC).

Euclidean Distance, shown in equation 3.5, is one of the most commonly used metrics. It measures the overall dissimilarity, meaning that lower values indicate higher similarity with 0 corresponding to the highest similarity possible. For two FC matrices FC^{emp} and FC^{sim} of size $(N \times N)$ where x and y correspond to the upper or lower triangular matrix element of each matrix respectively, $x = \{x_1, ..., x_n\}$, $y = \{y_1, ..., y_n\}$ and $n = \frac{N(N-1)}{2}$, the Euclidean Distance is given as the root sum of squared differences for each element of x and y

$$ED(x,y) = \sqrt{\sum_{i}^{n} (x_i - y_i)^2} \tag{3.5}$$

Pearson Correlation Coefficient (PCC), shown in equation 3.6, measures the linear correlation between 2 datasets and is commonly represented by r. Given x and y, r is given as the covariance of x and y divided by the product of their standard deviations.

$$r_{xy} = \frac{cov(x,y)}{\sigma_x \sigma_y} = \frac{\sum_{i=1}^{n} (x_i - \mu_x)(y_i - \mu_y)}{\sqrt{\sum_{i=1}^{n} (x_i - \mu_x)^2} \sqrt{\sum_{i=1}^{n} (y_i - \mu_y)^2}} \tag{3.6}$$

where μ_x, μ_y are means, σ_x, σ_y are standard deviations.

Structure Similarity Index, shown in equation 3.7 is mostly used in image processing and takes into account luminance, contrast, and structure. Given x and y, SSIM is calculated as:

$$\mathrm{SSIM}(x,y) = \frac{(2\mu_x\mu_y + c_1)(2\sigma_{xy} + c_2)}{(\mu_x^2 + \mu_y^2 + c_1)(\sigma_x^2 + \sigma_y^2 + c_2)} \tag{3.7}$$

where σ_x^2, σ_y^2 are variances, and σ_{xy} is covariance and c_1 and c_2 are two variables to stabilize the division with weak denominator.

Distance Correlation (dCor), shown in equation 3.10, is similar to Pearson Correlation Coefficient but captures both linear and nonlinear dependencies by calculating pairwise distances. Given x and y and the respective pairwise distance matrices $a_{i,j} = \sqrt{(x_i - x_j)^2}$ and $b_{i,j} = \sqrt{(y_i - y_j)^2}$ of size $(n \times n)$, the doubly centered distances matrices $A_{j,k} = a_{j,k} - \bar{a}_j - \bar{a}_k + \bar{a}$ and $B_{j,k} = b_{j,k} - \bar{b}_j - \bar{b}_k + \bar{b}$ are calculated. Distance covariance, shown in equation 3.8, is the average product of the A and B matrices. Distance variance, shown in equation 3.9, is the distance covariance for the same variable. Finally, dCor^2 is given as the squared distance covariance of x and y divided by the product of their distance standard deviations [55, 83, 27].

$$\mathrm{dCov}^2(x,y) = \frac{1}{n^2}\sum_{i=1}^{n}\sum_{j=1}^{n} A_{ij}B_{ij} \tag{3.8}$$

$$\mathrm{dVar}^2(x) = dCov^2(x,x) = \frac{1}{n^2}\sum_{j,k} A_{ij}^2 \tag{3.9}$$

$$\mathrm{dCor}^2(x,y) = \frac{\mathrm{dCov}^2(x,y)}{\sqrt{\mathrm{dVar}^2(x)\ \mathrm{dVar}^2(y)}} \tag{3.10}$$

3.6.1.1 Effective Connectivity

A gradient-descent approach was implemented to obtain the Effective Connectivity Matrix that maximizes similarity between empirical and simulated Functional Connectivity , using Structural Connectivity as a primmer (equation 3.11).

$$\mathrm{EC}_{ij}^{\mathrm{new}} = \mathrm{EC}_{ij}^{\mathrm{old}} + \alpha\left(\mathrm{FC}_{ij}^{emp} - \mathrm{FC}_{ij}^{sim}\right) \tag{3.11}$$

where α is the learning rate ($\alpha = 0.01$) and $(i,\ j)$ are the non-zero connectivity nodes [32, 49, 36].

3.6.2 Metastability and Coherence

For each of the 68 brain regions, the phase of the band-pass filtered neural activity time series are calculated by applying the Hilbert transform and obtaining $a(t) = A(t)e^{i\varphi(t)}$, where $A(t)$ is the instantaneous amplitude (or envelope) and $\varphi(t)$ the instantaneous phase, the same procedure used in connectivity calculation section 2.5.

The Kuramoto Order Parameter (KOP), $R(t)$, is a measure of synchronization in an ensemble of oscillating signals (equation 3.12). When the phases are uniformly distributed and the regions are independent, R approaches zero. Conversely, when all phases are equal, indicating full synchronization, R equals one.

$$R(t) = \left|\sum_{j=1}^{n} e^{i\varphi_j(t)}\right| / n \tag{3.12}$$

The temporal average of the Kuramoto Order Parameter was defined as the coherence, which provides a measure of mean synchronization across the brain regions. This coherence reflects the overall level of synchronization observed in the neural activity time series not to be confused with the FC metric Coherence mentioned in 2.5. The standard deviation of the Kuramoto Order Parameter defined as the metastability. The metastability captures the variation in synchronization over time, providing insights into the dynamic changes in synchronization patterns across the brain regions.

By calculating the coherence and metastability using the Kuramoto Order Parameter, it is possible to quantitatively assess the level of synchronization and its variability in the neural activity time series [35, 56, 24, 36, 78, 83, 34].

Unlike other metrics, when exploring the coherence and metastability no similarity metrics are required as they are scalars values and can be compared directly by applying a fit on the parameter exploration. In this thesis, a logarithmic fit was used in the form of $y = a\ln(x+c)+b$, where y equals either the coherence or metastability and x the a or G parameter. The parameter that results in matching of empirical and simulated coherence or metastability is estimated with $x = e^{\frac{y-b}{a}} - c$ and has a standard error σ_x, obtained from uncertainty propagation through partial derivatives, show in equation 3.14, where σ corresponds to the covariance matrix describing the uncertainty of parameters a, b, c and $\mathbf{J}$ the Jacobian matrix shown in equation 3.13 [15, 73].

$$\mathbf{J} = \begin{bmatrix} \frac{\partial x}{\partial a} & \frac{\partial x}{\partial b} & \frac{\partial x}{\partial c} \end{bmatrix} = \begin{bmatrix} -\frac{(y-b)}{a^2} e^{\frac{y-b}{a}} & -\frac{1}{a} e^{\frac{y-b}{a}} & -1 \end{bmatrix} \tag{3.13}$$

$$\sigma_x^2 = \mathbf{J}\Sigma\mathbf{J}^\top, \tag{3.14}$$

Statistical analysis is performed using the Pairwise Z-test. The test statistic is shown in equation 3.15. The power of the test is given by 3.16, where $\Phi(|z|)$ is the cumulative normal distribution function.

$$z = \frac{x_1 - x_2}{\sqrt{\sigma_1^2 + \sigma_2^2}} \tag{3.15}$$

$$p = 2 \cdot (1 - \Phi(|z|)) \tag{3.16}$$

3.6.3 Leading Eigenvector Dynamics Analysis

Leading Eigenvector Dynamics Analysis (LEiDA) is a method used to analyze brain activity taking into account transient dynamics and which reduces the dimensionality of the problem by using eigenvectors.

LEiDA has proven useful in studying brain states and their transitions, providing insights into the dynamic organization of Functional Connectivity in the brain. While it has not been directly applied to source estimated EEG data, its application to fMRI data has yielded valuable findings in understanding the spatio-temporal dynamics of brain activity and exploring functional subsystems involved in different cognitive processes [22, 64, 32, 59].

The analysis begins by calculating a phase coherence matrix, dFC(i, j, t), at each time point to quantify the synchrony between different brain regions. The signals are first band-pass filtered and then Hilbert-transformed to obtain the phase evolution of the time series for each node, the same process used in 3.6.2. The phase coherence between each pair of nodes, i and j, at time t is then estimated using the cosine of the phase difference, as shown in Equation 3.17:

$$\mathrm{dFC}(i, j, t) = \cos(\varphi(i, t) - \varphi(j, t)) \tag{3.17}$$

The cosine function is used to measure the similarity or alignment between the phases. If two brain areas have similar phases at that instance the phase coherence will be close to 1 (areas in-phase). On the other hand, if their signals are orthogonal or the phases vary significantly, the phase coherence will be close to 0 with the maximum phase difference corresponding to a phase coherence of -1 (areas in anti-phase).

The resulting dFC matrix is of size $N \times N \times T$, where N is the number of brain areas (in this case, 68) and T is the total number of time points. The dFC matrix is symmetric across the diagonal, and meaningful values can be obtained from either the upper or lower triangular parts of the matrix. This characteristic allows for dimensionality reduction by calculating its leading eigenvector, $V_1(t)$, at each time point. The leading eigenvector is the eigenvector associated with the largest eigenvalue. This leading eigenvector, of size $N \times 1$, captures the dominant connectivity pattern of the dFC matrix at that time point. By calculating the outer product of $V_1(t)$, $V_1 \otimes V_1^T$, the connectivity pattern can be visualized. By using the leading eigenvector we reduce dimensionality from $N(N-1)/2$ to N while still explaining most of its variance.

To identify recurrent FC patterns, clustering analysis is applied to all the leading eigenvectors $V_1(t)$ across time points epochs and tasks. The k-means clustering algorithm is used with varying values of k (number of clusters) from 2 to 20. The resulting cluster centroids represent the recurrent FC patterns and are named Probabilistic Metastable Substates (PMS). The optimal number of clusters, k, is determined based on various criteria such as Silhouette index and significant differences between condition probabilities.

Following this, each frequency and task is characterized by the probability of occurrence (or fractional occupancy), which is calculated with the number of epochs assigned to a given Probabilistic Metastable Substates divided by the total number of epochs for each task.

To measure the resemblance between the simulated and empirical PMS Euclidean Distance (equation 3.5) and Symmetrized Kullback-Leibler Divergence are used. Symmetrized Kullback-Leibler Divergence (KL), shown in 3.18, is a statistical measure used to quantify how much a model and empirical probability distribution Q and P vary.

$$\mathrm{KL}(P,Q) = \frac{1}{2}\sum_i \left[P(i)\log\left(\frac{P(i)}{Q(i)}\right) + Q(i)\log\left(\frac{Q(i)}{P(i)}\right)\right] \tag{3.18}$$

LEiDA is a very powerful tool to understand the brain however it is used in this study merely as a tool to get a better fit to the model, so details will not be explored in depth.

3.7 Statistical Analysis and Model Performance

As many of the methods used to calculate the Functional Connectivity rely on using a certain number of epochs the FC can not be calculated directly for each individual epoch. A bootstrap resampling approach was taken where 500 FC were calculated for each task, FC and frequency band using 50 random epochs. After the model is fully fitted epochs matching the experimental data (length of 4 s and frequency of 500 Hz) are simulated for each task, FC and frequency band, from which simulated FCs are calculated (each with 50 epochs following the experimental data bootstrap).

The procedure describe results in two datasets of empirical and simulated FCs, with shape $(n_{fb}, n_t, n_m, 500, n_n, n_n)$ where n_{fb} = number of frequency bands, n_m = number of FC metrics , n_t = number of tasks and n_m = number of nodes.

Statistical analysis is performed on each dataset for each node connection in particular, all upper or lower triangular FC elements, $(n_{fb}, n_t, n_m, 500, \frac{n_n \times (n_n - 1)}{2})$. The analysis starts with the Shapiro–Wilk test for normality followed by a Analysis of Variance (ANOVA) if the data is considered normal ($\alpha < 0.05$), otherwise the Kruskal-Wallis test is used. If there are significant differences ($\alpha < 0.05$), a pairwise comparison between each task is done using, respectively, Tukey's HSD (honestly significant difference) test (Tukey's HSD) or Wilcoxon signed-rank test depending on the data normality. False Discovery Rate (FDR) is corrected for using the Benjamini-Hochberg method.

To measure how well the simulated model performed, the statistical significant differences between the simulated and empirical data were overlapped via confusion matrix. The results are classified as: True Positive (TP) when the model correctly simulates an empirical difference (a hit); False Positive (FP) when the model simulates a difference that was not detected empirically (a false alarm, overestimation, or type I error); True Negative (TN) when there was no simulated or empirical difference (correct rejection); False Negative (FN) when there was no difference simulated by the model, but there was an empirical difference (a miss, underestimation or type II error).

Positive Predictive Value (PPV) or Precision, shown in equation 3.19, can be interpreted as the likelihood that the model will simulate a difference correctly.

$$\mathrm{PPV} = \frac{TP}{TP + FP} \tag{3.19}$$

Negative Predictive Value (NPV), shown in equation 3.20, is similar to PPV. It can be interpreted as the likelihood that the model will not incorrectly simulate a difference.

$$\mathrm{NPV} = \frac{TN}{TN + FN} \tag{3.20}$$

True Positive Rate (TPR) also named Recall or Sensitivity, shown in equation 3.21, can be seen as the probability of detection or the ratio between correctly simulated all empirical differences.

$$\mathrm{TPR} = \frac{TP}{TP + FN} \tag{3.21}$$

True Negative Rate (TNR) or Specificity, shown in equation 3.22, is similar to TPR, *i.e.* the probability of rejection. The ratio between all non significant differences and the correctly simulated ones.

$$\mathrm{TNR} = \frac{TN}{TN + FP} \tag{3.22}$$

Permutation testing with 10000 permutations and FDR correction is applied to each metric guaranteeing statistical significance, $\alpha < 0.05$.

The ED between averaged FC is calculated from which a matrix indicating task differences is obtained for each FC metric and frequency band. The correlation between ED matrices is then calculated as another model performance indicator.

Chapter 4

Results

4.1 Experimental Data Analysis

4.1.1 Functional Connectivity

As FC can present large variations across individuals, subjects were excluded from FC analysis if presenting an average FC z-score greater or equal to 2 or an Euclidean Distance (ED) between the FC and the grand average FC above 15. These values were determined empirically in order to remove outliers. Figure 4.1 shows the average of FC metrics for the sample of subjects included. FC for all subjects is shown in Figure A.1. Excluding only the subjects that fit the criteria the grand average FC was calculated for each data type. The Resting State FC is shown in figure 4.2, for each frequency band and each connectivity type. The task-related FC do not present noticeable differences and are shown in Appendix 5.

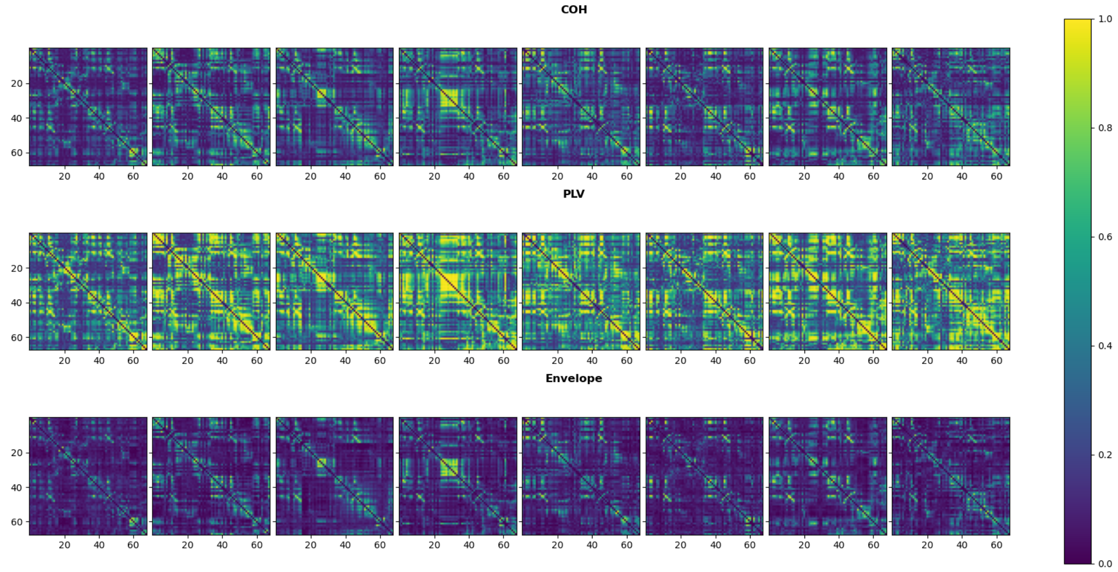

Figure 4.1: Resting State Functional Connectivity for subjects ($n = 8$) with z-score ≤ 2 and Euclidean Distance≤ 15. The color scale on the right refers to the connectivity. Envelope varies between -1 and 1 and has normalized to match the other metrics.

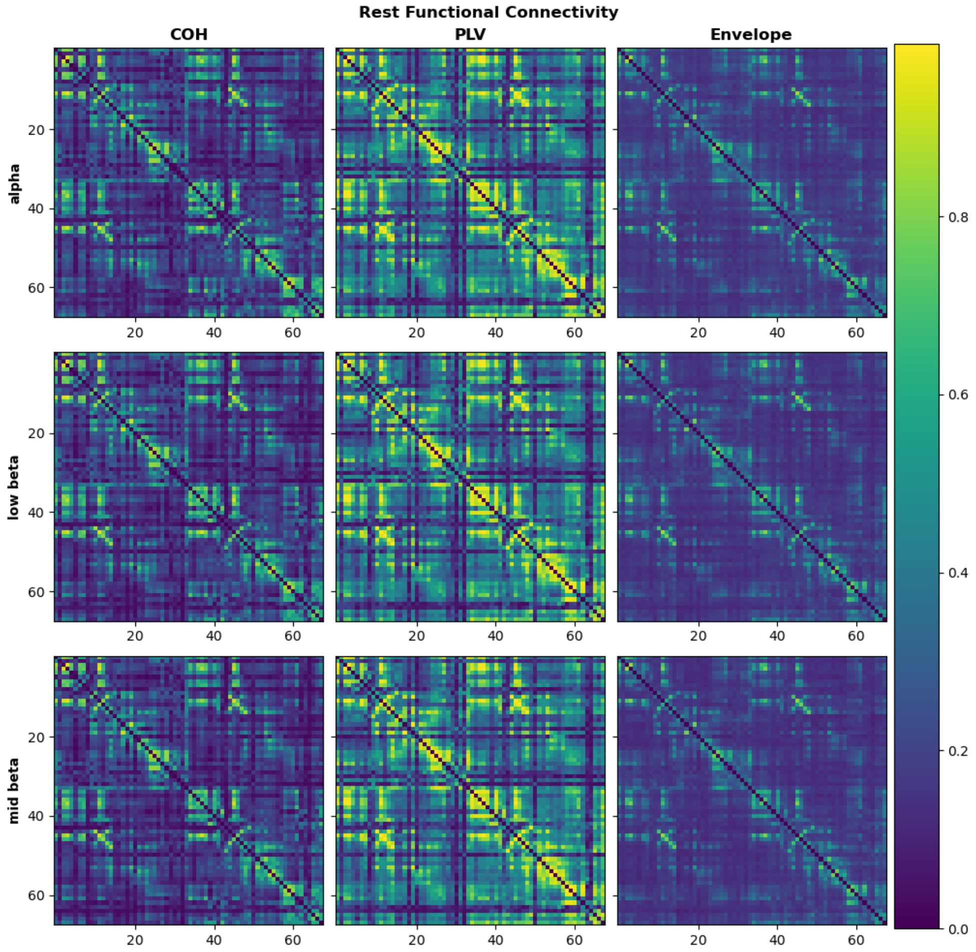

Figure 4.2: Grand average Functional Connectivity calculated in Resting State considering only the selected subjects, for alpha, low beta and mid beta frequency bands.

To better detect differences in FC between rest and tasks, we can subtract the REST FC from each task FC. Figure A.6 shows the results for Phase-Locking Value; the remaining can be found in section A.1 of the Appendices.

To analyze how the FC varies across activities, the Euclidean Distance between each task's FC was calculated and represented in two forms: a matrix for each FC metric and frequency band, shown in figure 4.4 and the corresponding ED in table 4.1.

Figure 4.3: PLV FC difference between rest and other tasks.

PLV is the metric where the most differences are measured , followed by COH and Envelope. The tasks that show the most differences are left and right handed Motor Execution, left and right handed Motor Imagery and left handed Motor Execution with right handed Motor Imagery. Differences are higher in between motor tasks than when compared with Resting State.

Table 4.1: Euclidean Distance between task's FC for all frequency bands and metrics with green and blue being values above 50th and 90th percentile for each metric, respectively.

	COH			PLV			Envelope			
	alpha	low beta	mid beta	alpha	low beta	mid beta	alpha	low beta	mid beta	mean
REST-MEL	2.37	2.55	2.49	2.51	2.69	2.48	1.39	1.37	1.34	2.13
REST-MER	2.16	1.78	1.78	2.41	2.12	2.23	1.28	1.22	1.20	1.8
REST-MIL	2.15	1.89	1.92	2.71	2.40	2.51	1.29	1.33	1.35	1.95
REST-MIR	2.03	2.16	1.71	2.22	2.08	2.30	1.34	1.29	1.27	1.82
MEL-MER	3.01	2.76	2.64	2.94	3.16	3.20	1.71	1.81	1.62	2.54
MEL-MIL	2.37	2.37	2.48	3.00	3.14	3.09	1.64	1.67	1.78	2.39
MEL-MIR	2.83	2.99	2.48	2.77	3.17	2.84	1.55	1.80	1.63	2.45
MER-MIL	2.61	2.03	2.41	3.31	3.00	2.78	1.63	1.64	1.71	2.35
MER-MIR	2.22	1.92	2.06	2.63	2.44	2.74	1.56	1.53	1.52	2.07
MIL-MIR	2.30	2.33	2.05	3.58	3.23	3.18	1.63	1.70	1.81	2.42
mean	2.41	2.28	2.2	2.81	2.74	2.73	1.5	1.54	1.52	

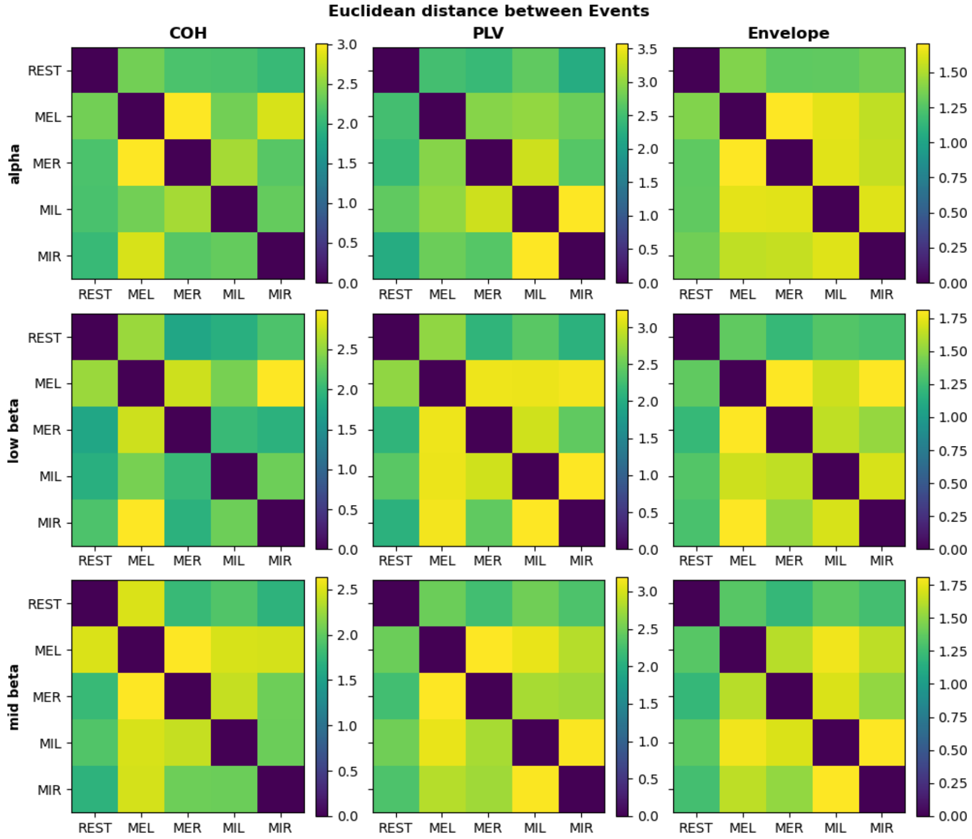

Figure 4.4: Euclidean Distance between task's FC for all frequency bands and methods

To check if these differences are significant, a statistical analysis is performed following the methods described in section 3.7. In section A.2 of the appendices, the biggest differences in task FC connections for each metric and frequency band are shown. Table 4.2 shows the average absolute statistically significant differences for each metric and frequency band. The results are consistent with the trends shown in table 4.1: PLV is the most sensitive metric, and Envelope the least. Non-REST comparisons exhibit stronger differences with the top three being MEL-MER, MIL-MIR and MEL-MIR.

Table 4.2: Average absolute FC task differences for all metrics and frequency bands. Only statistical significant differences ($\alpha < 0.05$) were considered

metric	frequency	REST-MEL	REST-MER	REST-MIL	REST-MIR	MEL-MER	MEL-MIL	MEL-MIR	MER-MIL	MER-MIR	MIL-MIR	mean
COH	alpha	0.0373	0.0353	0.0341	0.0328	0.0499	0.038	0.0458	0.0427	0.0364	0.0375	0.039
	low beta	0.0387	0.0298	0.0297	0.0343	0.0454	0.0384	0.0468	0.034	0.0314	0.0372	0.0366
	mid beta	0.037	0.0285	0.0305	0.0271	0.0425	0.0387	0.0389	0.0386	0.034	0.0332	0.0349
Envelope	alpha	0.0262	0.0243	0.0246	0.0255	0.0311	0.0305	0.0285	0.0298	0.0288	0.0298	0.0279
	low beta	0.0253	0.023	0.0245	0.0243	0.0328	0.0304	0.0329	0.0301	0.0282	0.0315	0.0283
	mid beta	0.0248	0.0227	0.0253	0.0236	0.0296	0.0326	0.0295	0.0309	0.0278	0.0338	0.0281
PLV	alpha	0.04	0.0387	0.0437	0.0373	0.0473	0.0481	0.0446	0.0533	0.0437	0.0588	0.0455
	low beta	0.0425	0.0343	0.0389	0.0344	0.0498	0.0506	0.0503	0.0486	0.0403	0.0532	0.0443
	mid beta	0.0388	0.0362	0.0411	0.0374	0.0515	0.0493	0.0454	0.0455	0.0451	0.0519	0.0442
	mean	0.0345	0.0303	0.0325	0.0307	0.0422	0.0396	0.0403	0.0393	0.0351	0.0408	

4.1.2 Metastability and Coherence

The coherence and metastability, calculated as explained in section 3.6.2, for each task and frequency band, are shown in figure 4.5. Using the same statistical analysis procedure as in 3.7, no significant differences were detected.

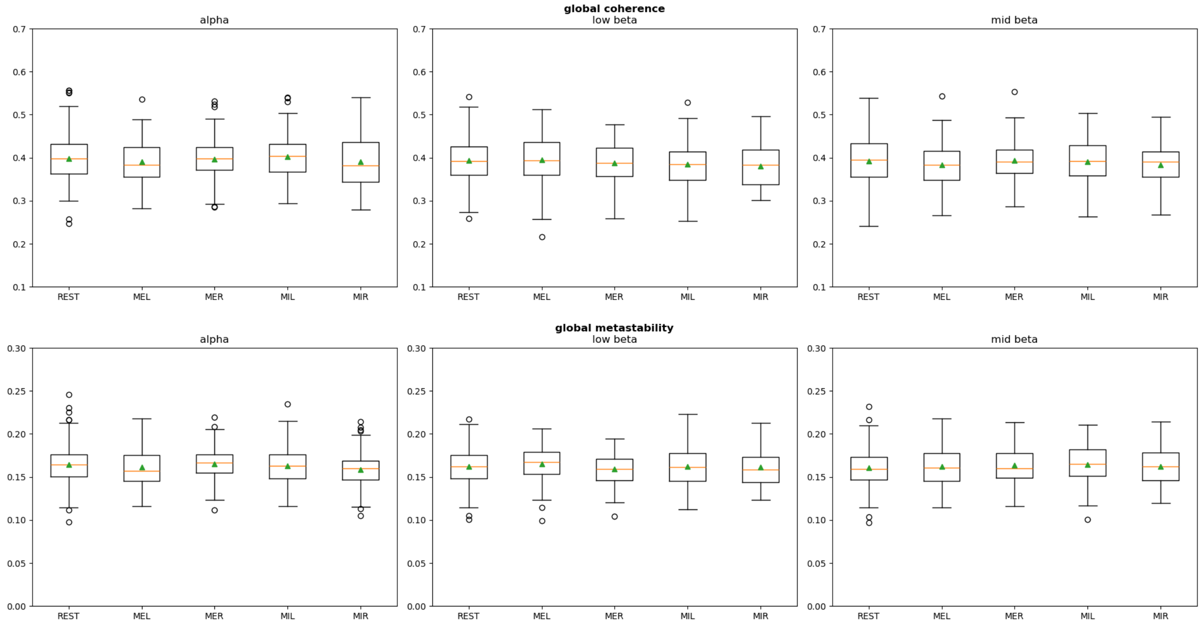

Figure 4.5: Coherence and metastability box plots for every task and frequency band

4.1.3 LEiDA

The results of the Leading Eigenvector Dynamics Analysis (LEiDA), obtained as explained in section 3.6.3, are shown in figures 4.6 and 4.7. The optimal number of clusters was determined to be 2 giving rise to PMS A and B. For each PMS the connectome, showing only connections in the 99% percentile, and the corresponding matrix are shown followed by the probability of occurrence for each frequency band and task. LEiDA does not help in distinguishing tasks as the PMS' probability of occurrence for each task are almost identical.

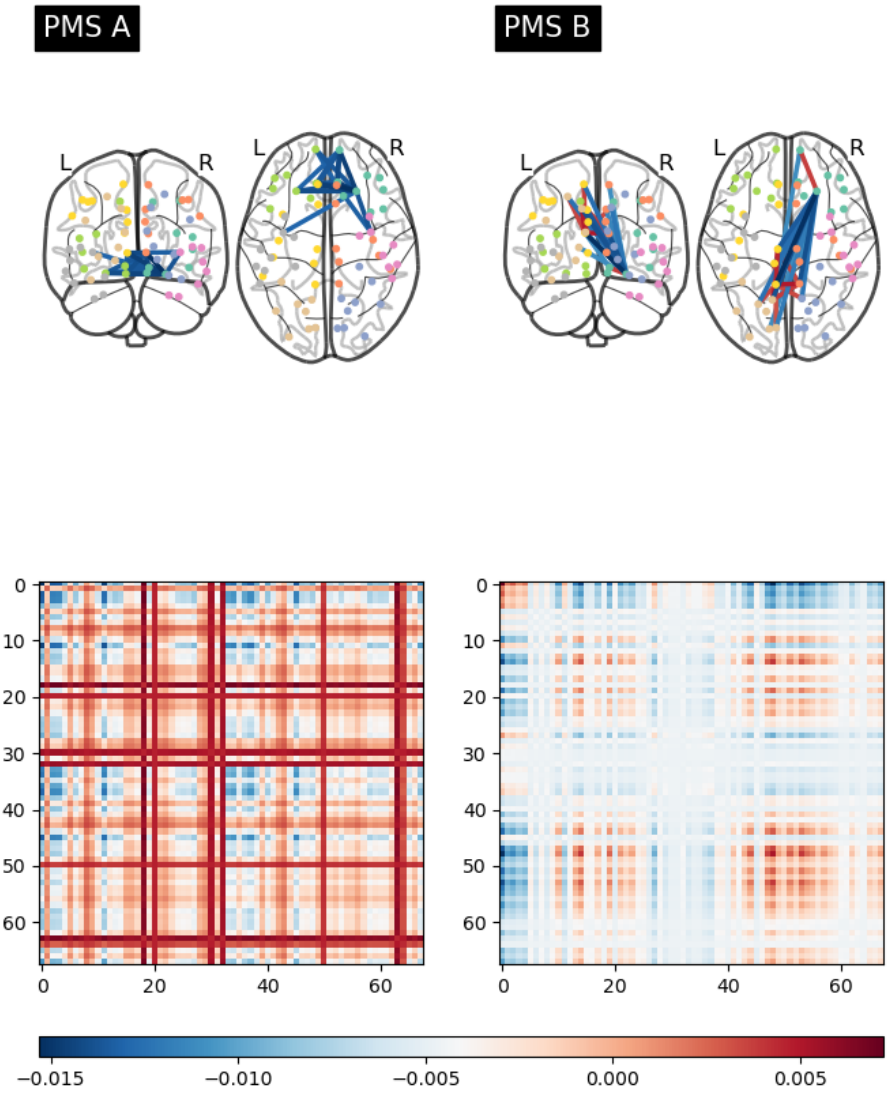

Figure 4.6: Probabilistic Metastable Substates obtained from Leading Eigenvector Dynamics Analysis. In the first row the connectome, showing only connections in the 95% percentile, are shown. The second row displays connectivity matrix.

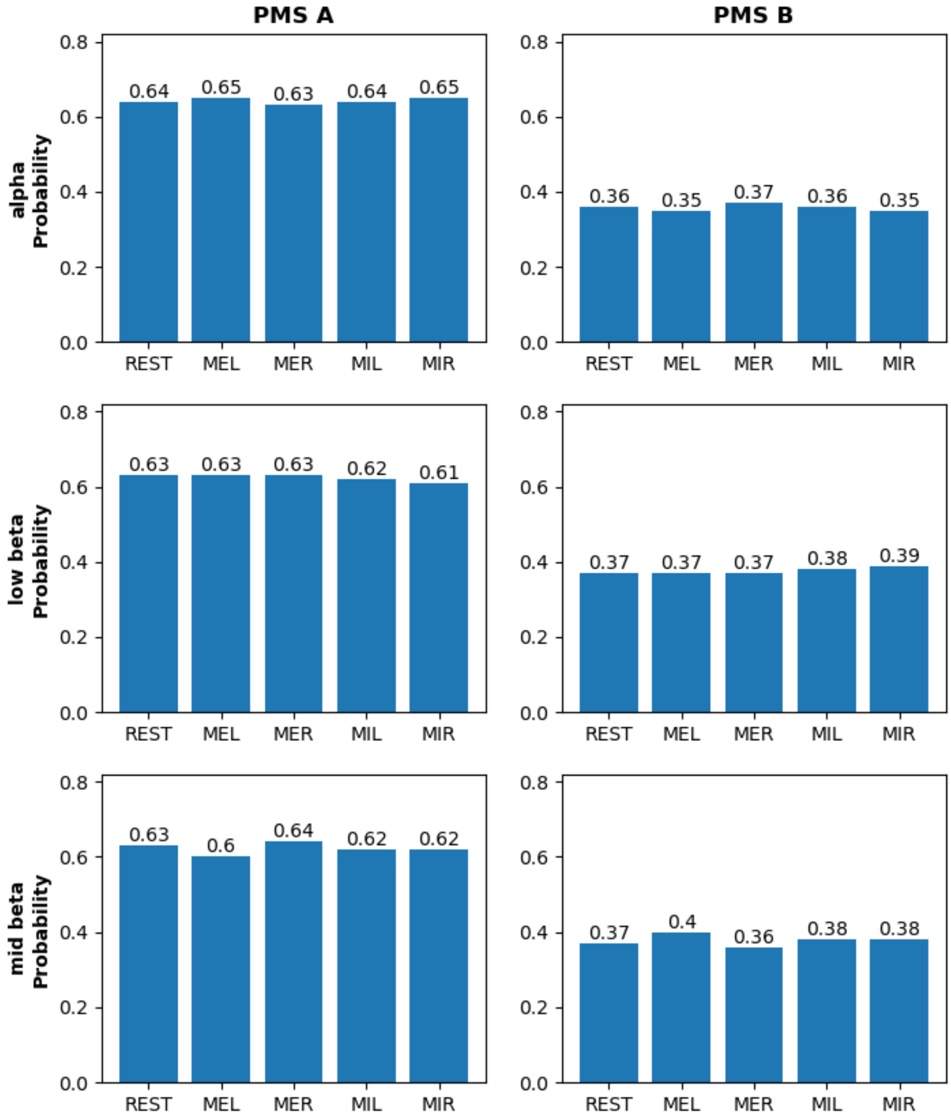

Figure 4.7: Probability of each PMS occurring for each task and frequency band.

4.2 Simulating data and comparing with Experimental data

4.2.1 Supercritical Bifurcation Region

As explained in section 3.5, there are 3 parameters that can be adjusted in the Hopf model: the bifurcation parameter a, the global coupling strength parameter G and the adjacency connectivity matrix C. The a parameter is normally set to 0 at the supercritical bifurcation. At this point the noise is enough to generate oscillations, but not in a sustained fashion.

This expected behavior was verified for low frequencies, but not for the ones of interest. Shown in figure 4.8 is the single node model output for 20 cycles at 2 different frequencies. At the lower frequency the model behaves as expected but at a higher frequency the model stays oscillating despite the *a* parameter being at or below 0.

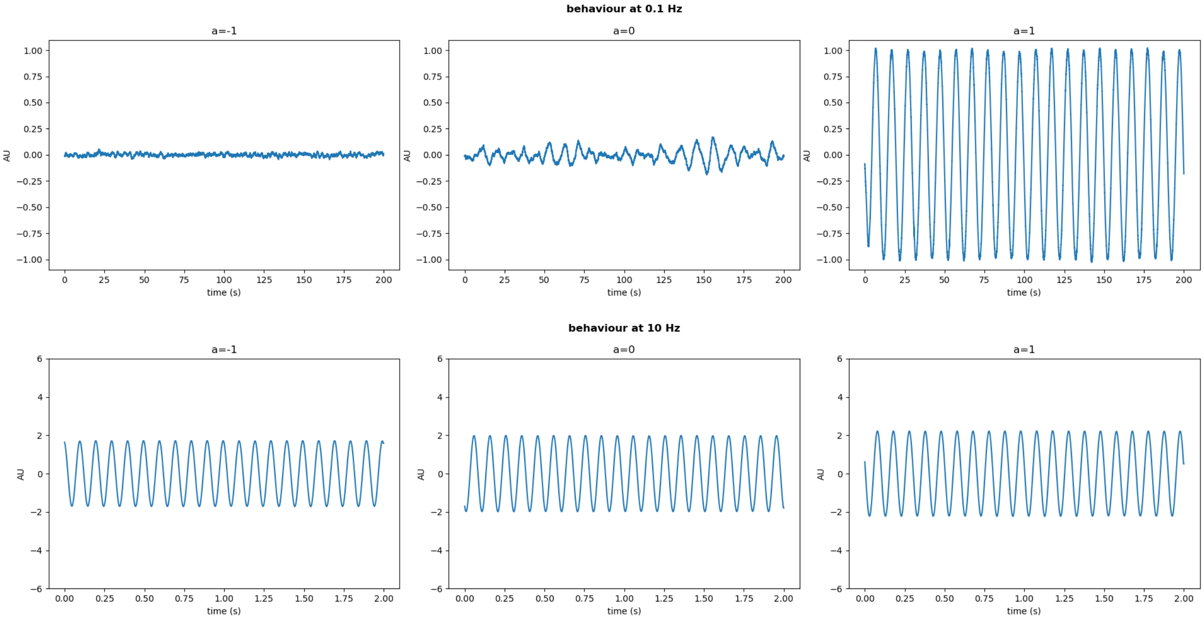

Figure 4.8: Model behavior at 1 Hz and 10 Hz for the 3 regimes: noisy ($a < 0$), fluctuating ($a = 0$) and oscillating ($a > 0$). At 10 Hz the model does not behave as expected and is always oscillating

To estimate if the signal was oscillating, two measures were used: the average amplitude for each oscillation cycle and the ratio between the frequency peak and total power, obtained from the Power Spectral Density (PSD). This gave us a good estimation of the position of the *a* parameter of the bifurcation. Higher frequencies have the bifurcation located at a lower value of the *a* parameter. This can be seen in figure 4.9, where for the two previous measures a threshold is set to estimate the *a* value at witch the model starts to oscillate. After getting an approximate location of the bifurcation for each frequency band an *a* parameter is chosen by plotting the time series. In figure 4.10, simulated data with the chosen *a* parameters, alongside experimental data is displayed.

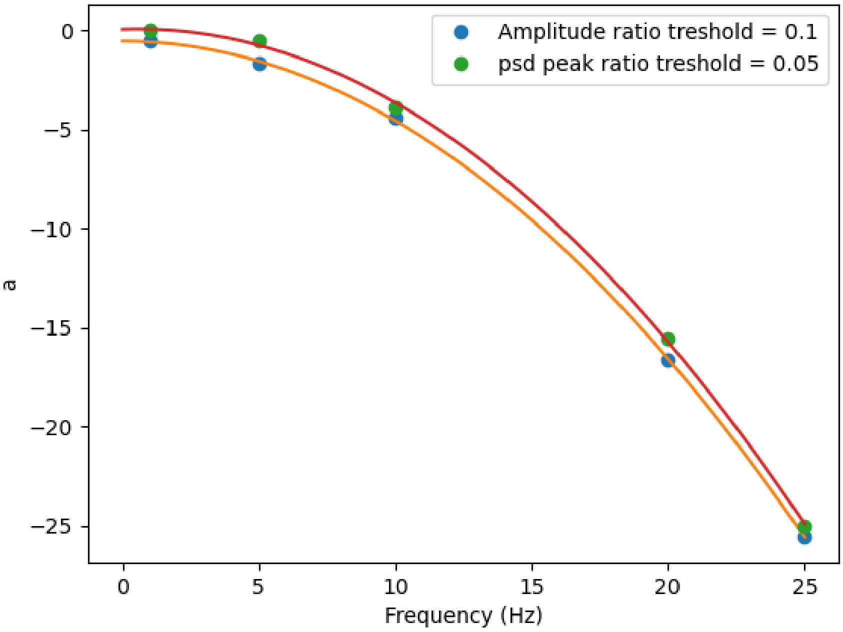

Figure 4.9: a values in which the model crosses the amplitude ratio threshold of 0.1, blue points, and PSD peak ration threshold of 0.05, green points. As the frequency increases a lower a value is required to reach the threshold.

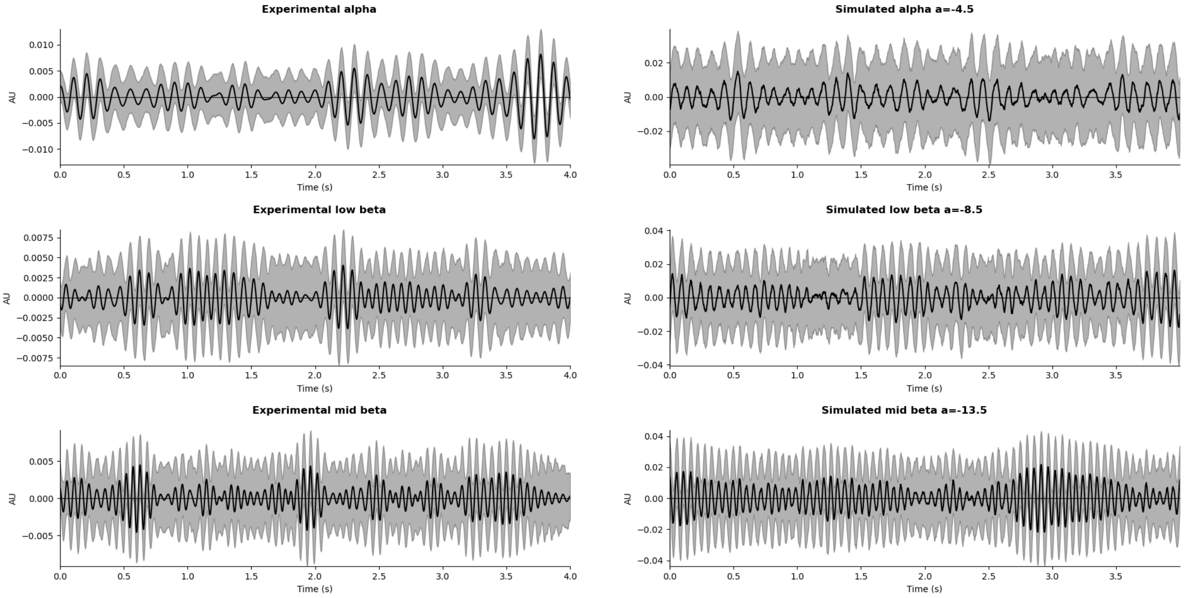

Figure 4.10: Filtered average experimental signal and average simulated signal for determined a values. The solid black line corresponds to the average and the grey shade represents the standard deviation. The simulated data's number of epochs and length match the experimental data's

4.2.2 FC Parameter Fit

For each Structural Connectivity, frequency band and task the a and G parameter were determined with the simulated and empirical Functional Connectivity, using the metrics mentioned on section 3.6. In figures 4.11 and 4.12 we have the G and a fit respectively for the structural connectivity based on the FA mean for the alpha frequency band. While the remaining fits are shown in sections B.1.1 and B.1.2 of the appendices, in table 4.3 a summary of the exploration result across all FC and SC metrics as well as frequency bands and tasks is shown.

The G parameter explorations were done using the supercritical bifurcation parameters found in section 4.2.1. Across the different SCs FA mean and Tract Lengths show similar trends. Both favor G values of around 1, while the number of fibers requires a higher G value of at least 4. Despite the trend lines being fairly noisy, the trend is very similar across different tasks and it is not possible to distinguish any significant differences in the G values the tasks tend to.

For the a fit, figure 4.12, the G values that maximized similarity found on the previous fit were used. No significantly different behavior is seen among tasks. In most fits, it is possible to identify a drop in similarity as the value of a increases past the threshold of the bifurcation. This is particularly clear in the ED metric. In a values below the threshold, the similarity is mostly constant.

All the fits are shown in sections B.1.2 and B.1.1. Table 4.3 shows a summary of the exploration result across all FC and SC metrics as well as frequency bands and tasks. Overall COH FC shows the highest similarity followed by Envelope and Phase-Locking Value (PLV). The mid beta frequency band shows a higher similarity compared to the remaining bands and the FA mean SC also shows higher similarity compared to the other SC metrics. There are no clear differences in between tasks.

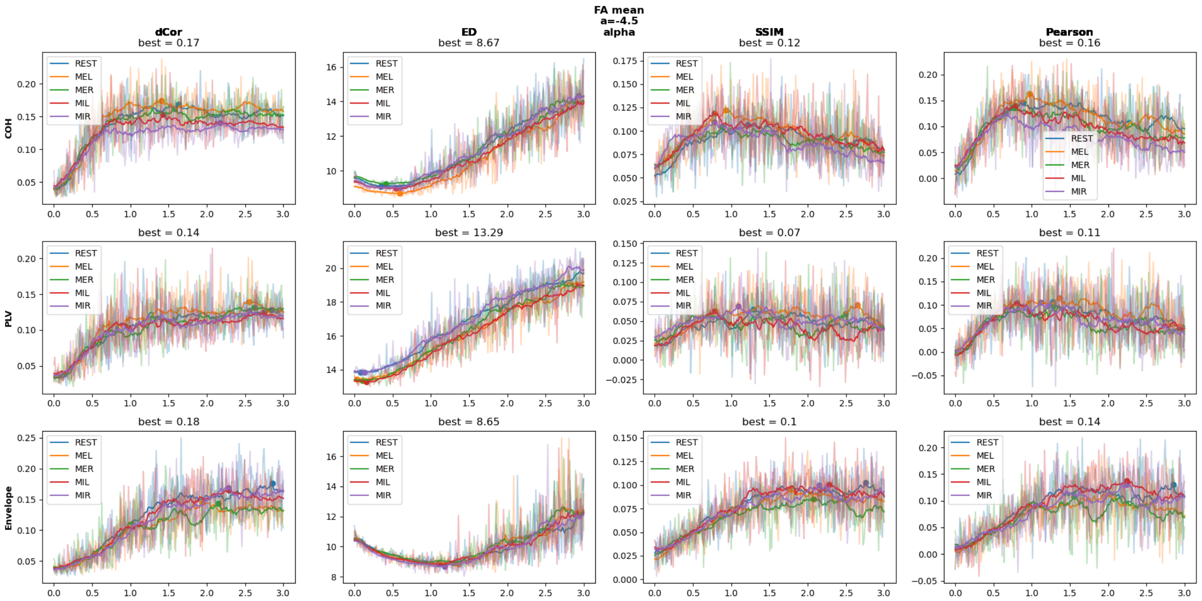

Figure 4.11: G parameter exploration using FA mean as the adjacency connectivity matrix, C, for every task at the alpha frequency and the respective supercritical bifurcation parameter. Each color corresponds to a different task's fit with a moving average filter and a dot on the best fit point. The actual fits are the shaded profiles.

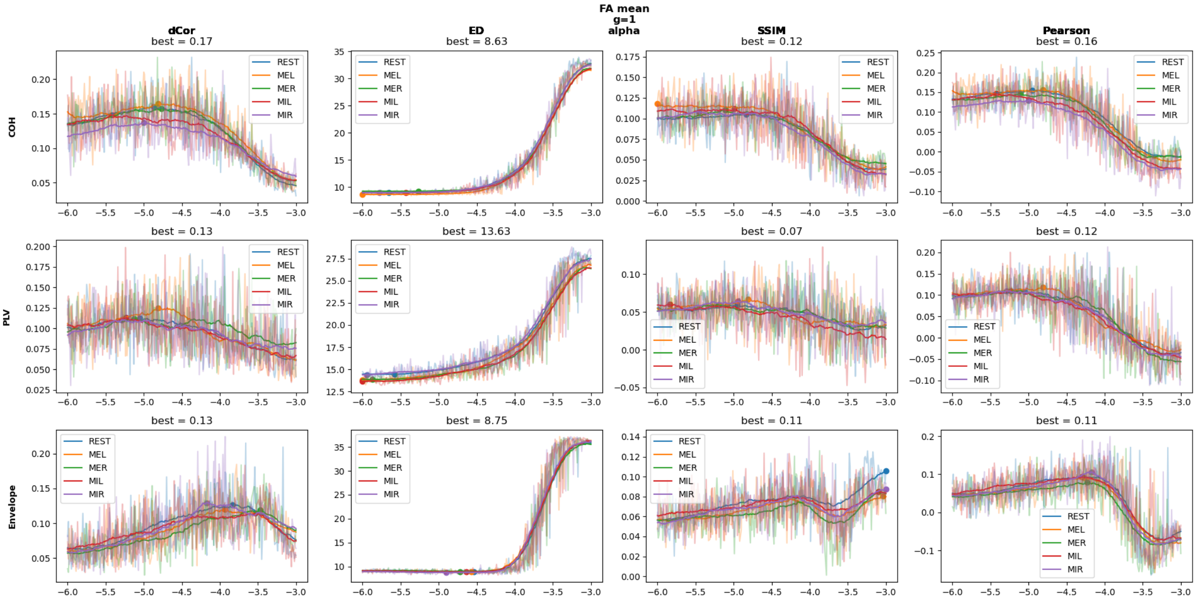

Figure 4.12: *a* parameter exploration using FA mean as the adjacency connectivity matrix, *C*, for every task at the alpha frequency. The *g* parameter was chosen for each structural connectivity based on the previous *g* parameter exploration. Each color corresponds to a different task's fit with a moving average filter and a dot on the best fit point. The actual fits are the shaded profiles.

Table 4.3: *a* and *G* parameter exploration summary, best similarity metric values, averaged across different explored variables

	G exploration				*a* exploration			
	ED	dCor	SSIM	Pearson	ED	dCor	SSIM	Pearson
alpha	10.605	0.127	0.085	0.112	10.537	0.136	0.083	0.117
low beta	10.596	0.132	0.087	0.119	10.54	0.146	0.088	0.13
mid beta	10.513	0.139	0.089	0.126	10.518	0.151	0.086	0.133
MEL	10.443	0.133	0.088	0.123	10.411	0.15	0.088	0.133
MER	10.599	0.133	0.085	0.115	10.579	0.142	0.083	0.122
MIL	10.504	0.133	0.086	0.12	10.449	0.144	0.088	0.129
MIR	10.567	0.133	0.088	0.12	10.53	0.142	0.087	0.124
REST	10.743	0.131	0.087	0.116	10.688	0.145	0.083	0.125
FA mean	10.551	0.146	0.094	0.133	10.458	0.16	0.095	0.135
Number of fibers	10.563	0.145	0.092	0.138	10.633	0.155	0.093	0.155
Tract lengths	10.599	0.107	0.076	0.086	10.503	0.118	0.068	0.091
COH	8.839	0.155	0.109	0.15	8.965	0.17	0.114	0.16
Envelope	8.908	0.126	0.092	0.103	8.918	0.141	0.082	0.113
PLV	13.967	0.116	0.06	0.103	13.712	0.123	0.06	0.106

4.2.3 Effective Connectivity

The last parameter that can be fitted in the Hopf model is the adjacency connectivity matrix, C. This is done using equation 3.11 as explained in chapter 3.6.1.1 for each frequency and task.

An initial exploration is done for the different SC and FC, shown in figure 4.13. The Coherence FC achieves the closest similarity out of all the connectivity metrics. FA mean SC is used as the initial value on EC fits going forward as the initial SC does not appear to have much of an effect.

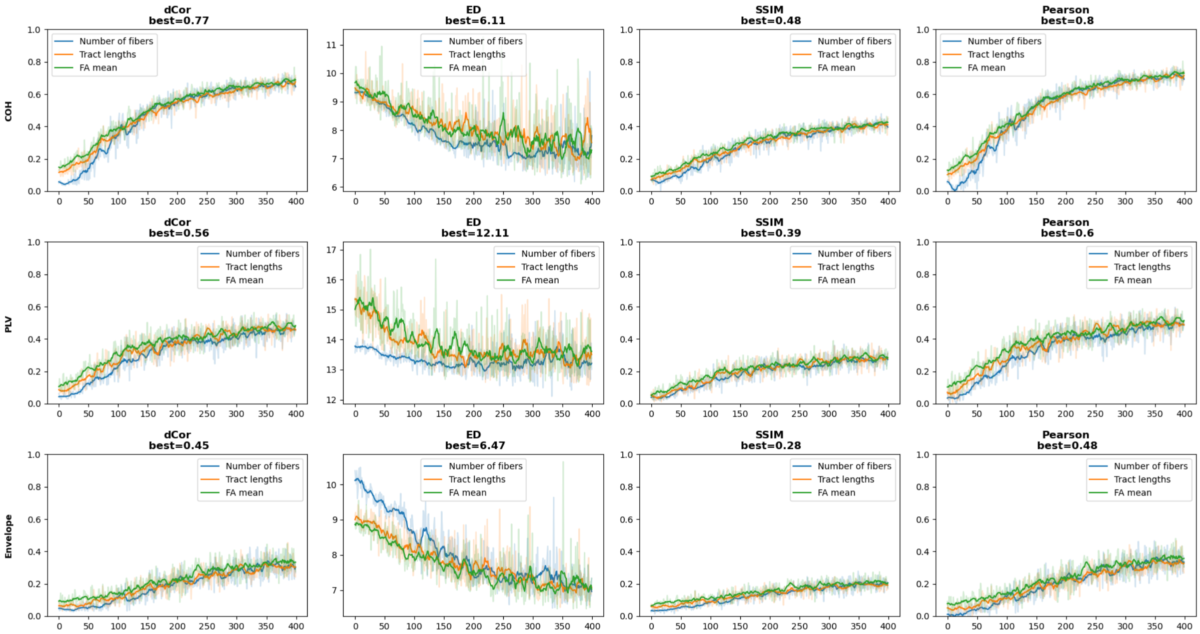

Figure 4.13: EC fit for each SC and FC at the alpha frequency and respective supercritical bifurcation parameter. Each color corresponds to a fit with a different SC starting point with a moving average filter. The actual fit is displayed in a less opaque color.

An Effective Connectivity Matrix was fitted for every task type and frequency with a corresponding to the supercritical bifurcation values found for each frequency previously, the global coupling parameter, $G = 1$ and a learning step, $\alpha = 0.01$ for 500 iterations. This is shown for the COH metric in figure 4.14. The remaining are in section B.2 of the appendices.

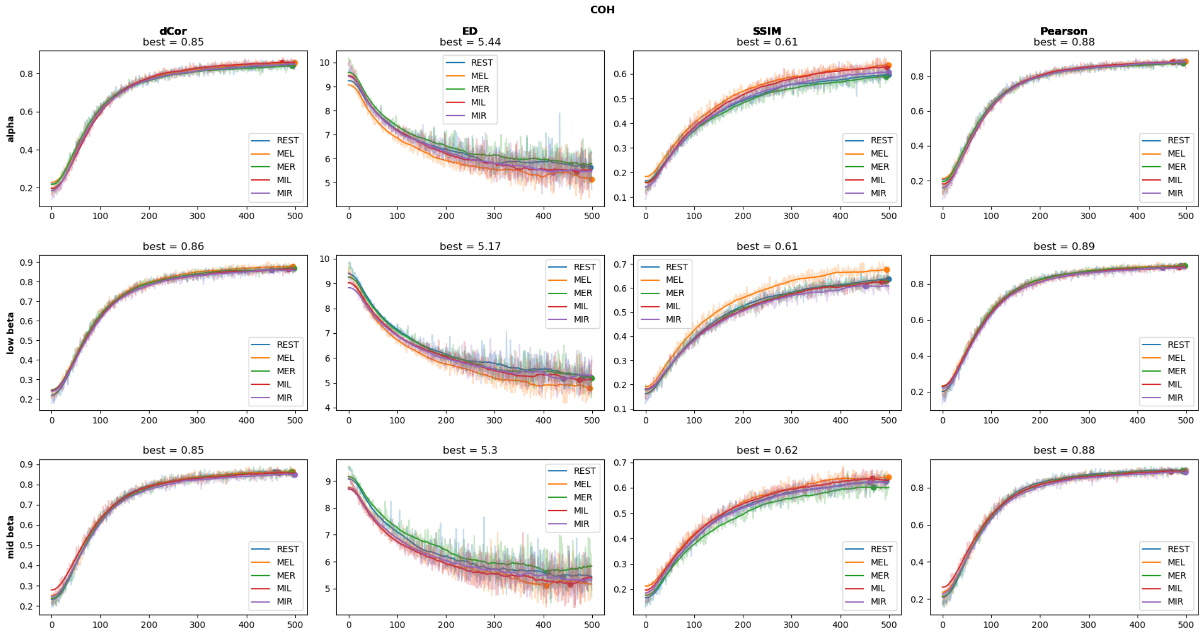

Figure 4.14: EC fit for each task type and frequency at respective supercritical bifurcation parameter and $g = 1$ using the COH FC. Each color corresponds to a fit with a different task type with a moving average filter. The actual fit is displayed in a less opaque color.

As the EC fits in 4.14 converge, the final EC is calculated as the mean EC from the last 100 iterations. These can be seen in figure 4.15 for COH. Some differences can be made visible by subtracting the REST EC from each task's EC, shown in figure 4.16 for COH, similarly to what happens in the empirical FC (results for the other FC metrics are shown in section B.2). When using the ED to compare the fitted EC, shown in table 4.4, the results show a very similar trend to the empirical FC, shown in 4.1, in that Non-REST comparisons exhibit larger differences, with the strongest being MEL-MER, MIL-MIR and MEL-MIR, however the metric indicating the largest differences between tasks is, in this case, COH.

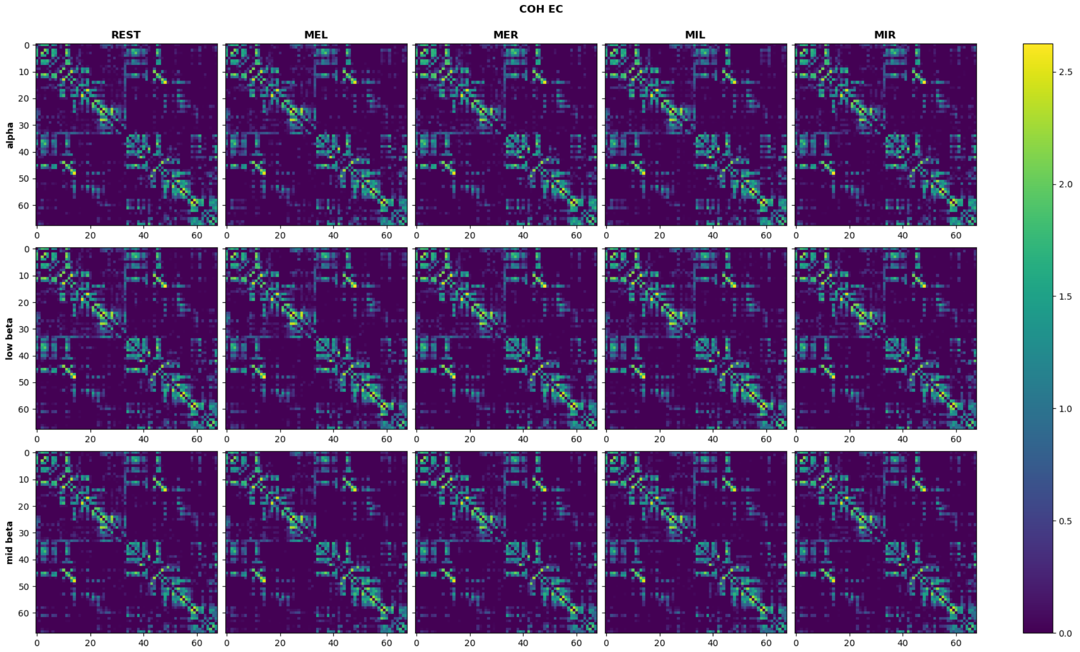

Figure 4.15: EC matrix for each for each frequency and task type using the COH FC

Figure 4.16: Differences between REST EC matrix and every other tasktype for each frequency, EC fitted using the COH FC

Table 4.4: Euclidean Distance between task's EC for all frequency bands and methods with green and blue being values above 50th and 90th percentile of each method

	COH			PLV			Envelope			
	alpha	low beta	mid beta	alpha	low beta	mid beta	alpha	low beta	mid beta	mean
REST-MEL	4.21	4.99	4.80	3.36	3.45	2.93	3.32	3.52	3.14	3.75
REST-MER	3.73	3.01	2.67	3.14	2.98	3.16	3.21	3.04	2.91	3.09
REST-MIL	3.60	3.56	3.48	3.80	3.26	3.26	3.15	3.45	3.10	3.41
REST-MIR	3.51	3.77	3.00	2.95	3.06	3.20	3.16	3.17	3.07	3.21
MEL-MER	5.70	5.36	5.45	4.49	4.43	4.32	4.40	4.42	3.91	4.72
MEL-MIL	4.67	4.36	4.29	4.40	4.27	3.87	4.21	4.46	3.95	4.27
MEL-MIR	5.53	5.34	4.99	3.99	4.03	3.62	4.02	4.31	3.96	4.42
MER-MIL	4.89	3.66	3.90	4.82	4.37	4.14	4.19	4.12	3.85	4.22
MER-MIR	4.10	3.61	3.64	3.76	3.68	4.10	3.94	3.79	3.71	3.82
MIL-MIR	4.48	4.30	3.88	5.01	4.66	4.36	4.13	4.30	4.27	4.38
mean	4.44	4.2	4.01	3.97	3.82	3.7	3.77	3.86	3.59	

4.2.3.1 FC Parameter Fit With Effective Connectivity

Parameters were explored using the same methods as in section 4.2.2 with the fitted EC for each frequency and task type. In figures 4.17 and 4.18, the parameter exploration for the PLV metric is shown. When compared to the fits using SC, it is still not possible to distinguish differences in behavior for the different tasks, however the fits are much less noisy and with more well defined maximum and minimum.

Other FC metrics are shown in section B.3. Table 4.5shows a summary of the exploration result across all FC metrics as well as frequency bands and tasks. When compared to table 4.3, containing the results of the initial parameter exploration using SC, the similarity increased drastically for all similarity metrics. Across frequency bands and tasks the results are overall very similar. For the FC metrics, the results are somewhat contradictory between ED and the other similarity metrics and as such there is no clearly superior FC metric. PLV shows the largest increase in similarity, while still having the highest ED, it is superior or equal to COH and Envelope FCs in the other metrics.

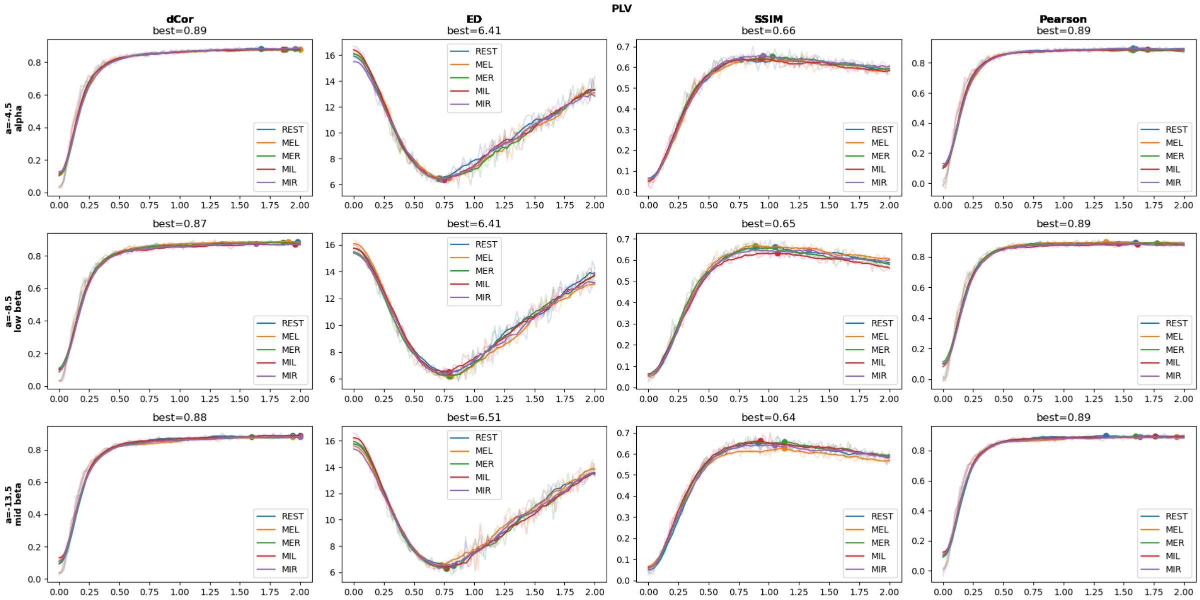

Figure 4.17: *G* parameter exploration using EC as the adjacency connectivity matrix, *C*, for every task and frequency band for the PLV FC metric. The *a* parameter is the bifurcation location determined for each frequency band. Each color corresponds to a different task's fit with a moving average filter and a dot on the best fit point. The actual fit is displayed in a less opaque color

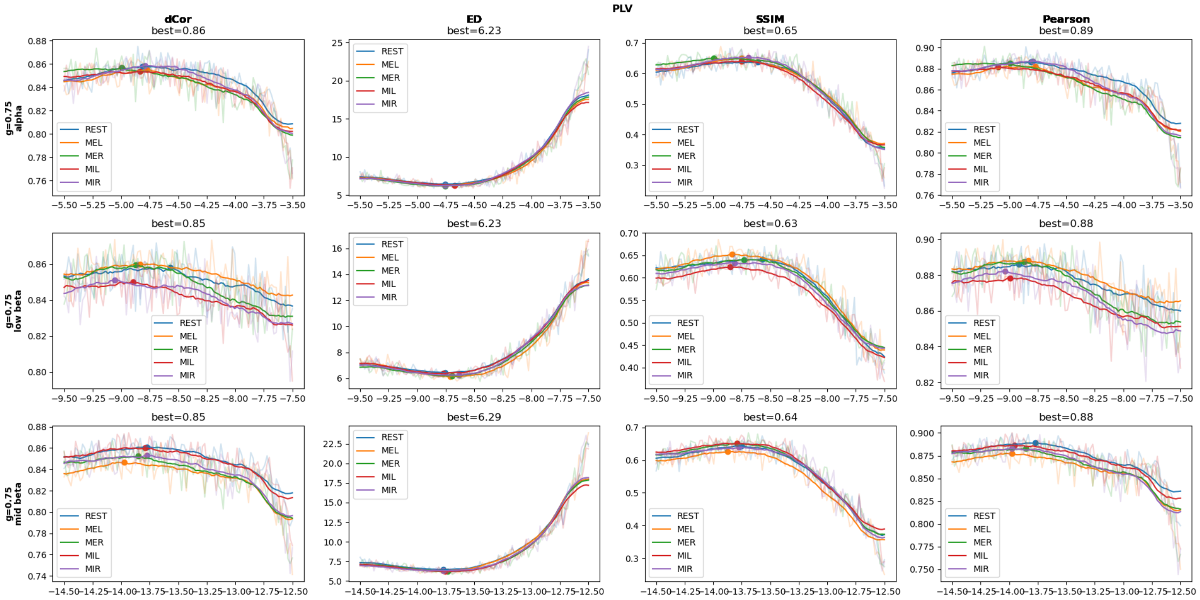

Figure 4.18: *a* parameter exploration using EC as the adjacency connectivity matrix, *C*, for every task and frequency band for the PLV FC metric. The *G* parameter was chosen for each structural connectivity based on the previous *G* parameter exploration. Each color corresponds to a different task's fit with a moving average filter and a dot on the best fit point. The actual fit is displayed in a less opaque color

Table 4.5: Summary of *a* and *G* parameter exploration with EC. Best similarity metric values, averaged across different explored variables

	G exploration				*a* exploration			
	ED	dCor	SSIM	Pearson	ED	dCor	SSIM	Pearson
alpha	5.026	0.831	0.62	0.853	4.973	0.822	0.612	0.852
low beta	4.92	0.833	0.626	0.856	4.912	0.823	0.613	0.853
mid beta	4.949	0.836	0.623	0.86	4.878	0.827	0.615	0.857
MEL	4.907	0.833	0.627	0.856	4.867	0.823	0.62	0.855
MER	5.006	0.831	0.618	0.855	4.955	0.824	0.609	0.854
MIL	4.972	0.835	0.624	0.856	4.915	0.826	0.612	0.855
MIR	4.944	0.829	0.618	0.853	4.903	0.818	0.607	0.85
REST	4.996	0.839	0.63	0.86	4.965	0.829	0.617	0.857
COH	4.936	0.865	0.627	0.896	4.985	0.883	0.611	0.913
Envelope	3.628	0.751	0.587	0.778	3.638	0.729	0.576	0.761
PLV	6.331	0.884	0.655	0.894	6.141	0.86	0.652	0.888

4.2.3.2 Metastability and Coherence

The empirical metastability and coherence, as well as the *a* and *G* parameter did not allow for the distinction of task types so it is only by using the EC that it becomes possible to fit. For each frequency, respective supercritical bifurcation parameter *a*, FC metric and task, the metastability and coherence are simulated for different *G* values, in a similar fashion to the initial *G* exploration. A logarithmic fit is then done on the *G* parameter exploration to estimate which *G* value best reproduces the empirical metastability and coherence. This is shown in figures 4.19 and 4.20 respectively, for the COH metric. The remaining figures are shown in section A.3 of the appendices.

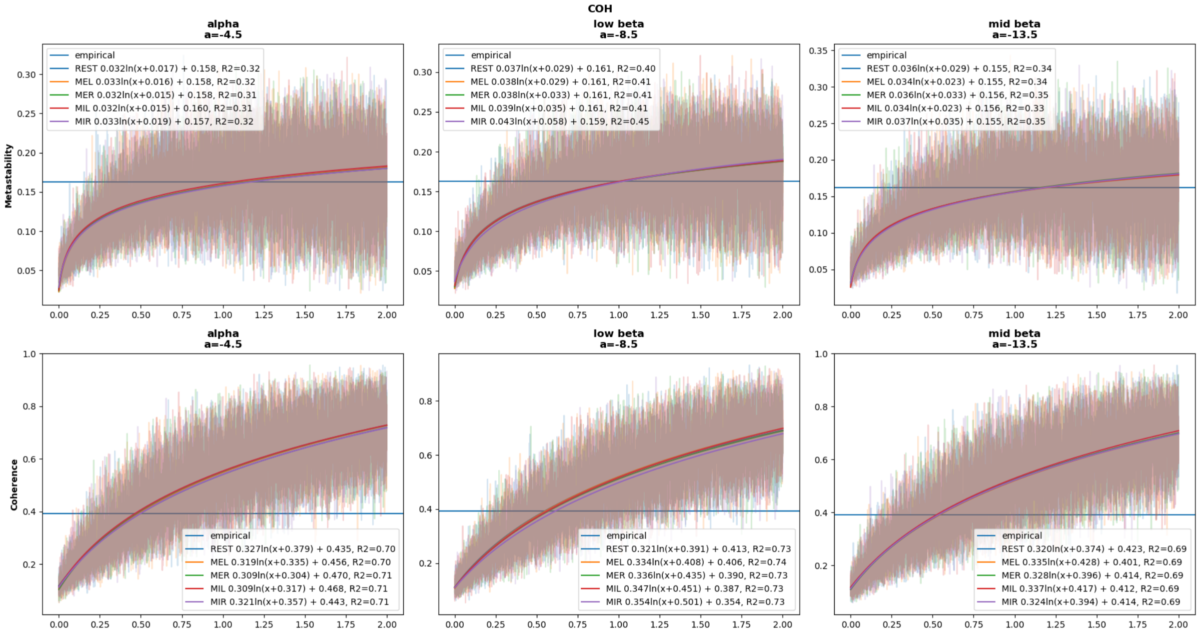

Figure 4.19: COH EC coherence and metastability *G* parameter fit for each frequency and the respective critical bifurcation region parameter

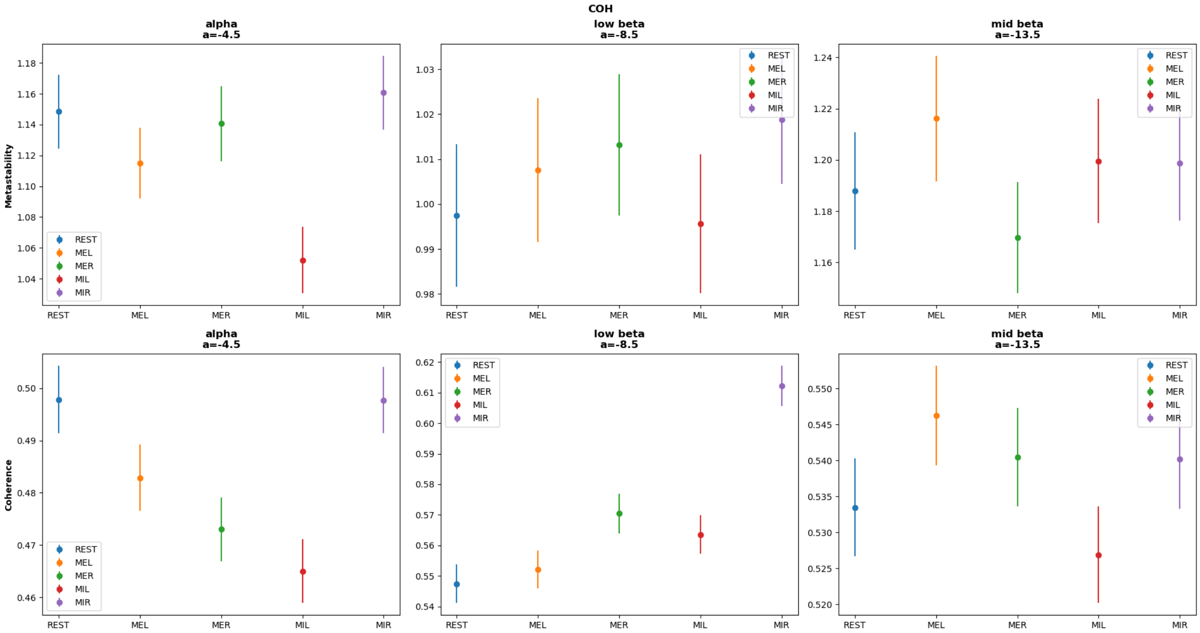

Figure 4.20: *G* parameter value estimated from the linear fits ,shown in 4.19.

The model is able to reproduce the empirical metastability and coherence however there is a large amount of variance. This is reflected in the goodness of the fit, R^2, that is particularly low for the metastability. The estimated *G* values for coherence and metastability are gathered in tables 4.6 and 4.7, respectively. For coherence *G* was highest for low beta, followed by mid beta, and then alpha frequencies, however for metastability low beta becomes the frequency band with lowest estimated *G*.

Table 4.6: Estimated *G* values from coherence fitting

	COH			Envelope			PLV			
	alpha	low beta	mid beta	alpha	low beta	mid beta	alpha	low beta	mid beta	mean
REST	0.498	0.547	0.533	0.45	0.507	0.495	0.475	0.548	0.483	0.504
MEL	0.483	0.552	0.546	0.457	0.486	0.503	0.465	0.53	0.481	0.5
MER	0.473	0.57	0.54	0.446	0.522	0.487	0.458	0.557	0.482	0.504
MIL	0.465	0.564	0.527	0.459	0.491	0.467	0.44	0.549	0.451	0.49
MIR	0.498	0.612	0.54	0.464	0.522	0.497	0.498	0.564	0.486	0.52
mean	0.483	0.569	0.537	0.455	0.506	0.49	0.467	0.55	0.477	

Table 4.7: Estimated G values from metastability fitting

	COH			Envelope			PLV			
	alpha	low beta	mid beta	alpha	low beta	mid beta	alpha	low beta	mid beta	mean
REST	1.149	0.997	1.188	0.981	0.891	1.079	1.301	1.105	1.405	1.122
MEL	1.115	1.008	1.216	1.006	0.855	1.117	1.289	1.119	1.356	1.12
MER	1.141	1.013	1.17	1.026	0.903	1.042	1.372	1.119	1.315	1.122
MIL	1.052	0.996	1.2	1.064	0.873	1.047	1.371	1.088	1.395	1.121
MIR	1.161	1.019	1.199	1.005	0.916	1.053	1.347	1.144	1.393	1.137
mean	1.124	1.007	1.195	1.016	0.888	1.068	1.336	1.115	1.373	

Tables 4.8 and 4.9 show differences in the estimated G values across tasks, with statistically significant differences ($\alpha < 0.05$) displayed in bold. Looking at coherence, table 4.8, there seems to be a clear trend across FC metrics and frequency bands where right side related tasks show higher G when compared to left sided tasks. In the metastability results, table 4.9, there are less significant values and no obvious trend, this is to be expected due to the very low R^2.

Table 4.8: Task differences in estimated G (coherence), significant differences ($\alpha < 0.05$) are displayed in bold

	COH			Envelope			PLV		
	alpha	low beta	mid beta	alpha	low beta	mid beta	alpha	low beta	mid beta
REST-MEL	0.015	-0.005	-0.013	-0.007	**0.021**	-0.008	0.011	**0.019**	0.002
REST-MER	**0.025**	**-0.023**	-0.007	0.003	-0.015	0.009	**0.017**	-0.009	0.001
REST-MIL	**0.033**	-0.016	0.007	-0.009	**0.016**	**0.029**	**0.035**	-0.001	**0.032**
REST-MIR	0.0	**-0.065**	-0.007	-0.014	-0.016	-0.002	**-0.023**	-0.015	-0.003
MEL-MER	0.01	**-0.018**	0.006	0.011	**-0.036**	0.016	0.006	**-0.027**	-0.001
MEL-MIL	**0.018**	-0.011	**0.019**	-0.002	-0.004	**0.036**	**0.025**	**-0.02**	**0.03**
MEL-MIR	-0.015	**-0.06**	0.006	-0.007	**-0.036**	0.006	**-0.034**	**-0.034**	-0.005
MER-MIL	0.008	0.007	0.014	-0.013	**0.032**	**0.02**	**0.018**	0.008	**0.031**
MER-MIR	**-0.025**	**-0.042**	0.0	**-0.017**	-0.0	-0.01	**-0.04**	-0.007	-0.004
MIL-MIR	**-0.033**	**-0.049**	-0.013	-0.005	**-0.032**	**-0.031**	**-0.058**	-0.015	**-0.035**

Table 4.9: Significant task differences in estimated G (metastability), significant differences ($\alpha < 0.05$) are displayed in bold

	COH			Envelope			PLV		
	alpha	low beta	mid beta	alpha	low beta	mid beta	alpha	low beta	mid beta
REST-MEL	0.033	-0.01	-0.028	-0.025	0.036	-0.038	0.013	-0.014	0.049
REST-MER	0.008	-0.016	0.018	-0.045	-0.012	0.038	-0.07	-0.014	0.089
REST-MIL	**0.096**	0.002	-0.012	**-0.083**	0.018	0.032	-0.07	0.017	0.009
REST-MIR	-0.012	-0.021	-0.011	-0.023	-0.025	0.026	-0.046	-0.039	0.012
MEL-MER	-0.026	-0.006	0.047	-0.02	**-0.048**	**0.075**	-0.083	0.0	0.04
MEL-MIL	**0.063**	0.012	0.017	-0.058	-0.018	**0.07**	-0.083	0.031	-0.04
MEL-MIR	-0.046	-0.011	0.017	0.001	**-0.061**	**0.064**	-0.059	-0.025	-0.037
MER-MIL	**0.089**	0.018	-0.03	-0.038	0.03	-0.006	0.0	0.031	-0.08
MER-MIR	-0.02	-0.006	-0.029	0.021	-0.013	-0.011	0.024	-0.025	-0.077
MIL-MIR	**-0.109**	-0.023	0.001	0.059	-0.043	-0.006	0.024	**-0.056**	0.003

4.2.3.3 Leading Eigenvector Dynamics Analysis

The parameter exploration done previously for a and G is repeated for the similarity between PMS obtained through LEiDA and presented in figures 4.21 and 4.22. It does appear that the model simulates the PMS somewhat successfully, but is not very useful at narrowing down a unique solution other than the best a being at the bifurcation location as was already known.

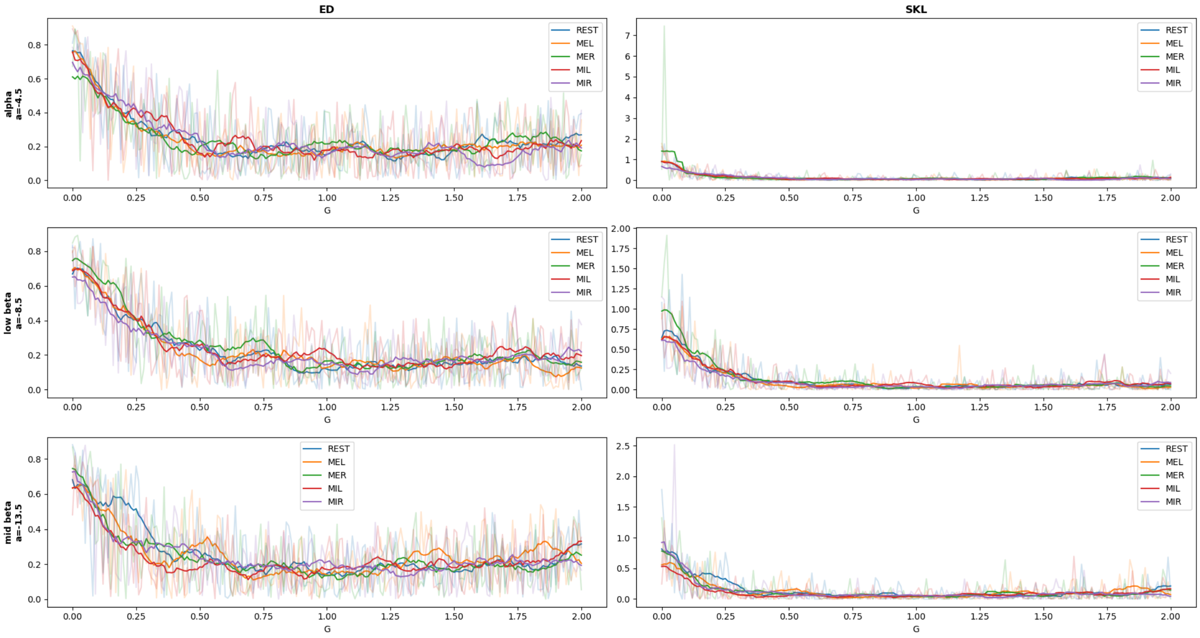

Figure 4.21: G parameter exploration for each task and frequency band at the respective supercritical bifurcation. Each color corresponds to a different task's fit with a moving average filter. The actual fit is displayed in a less opaque color

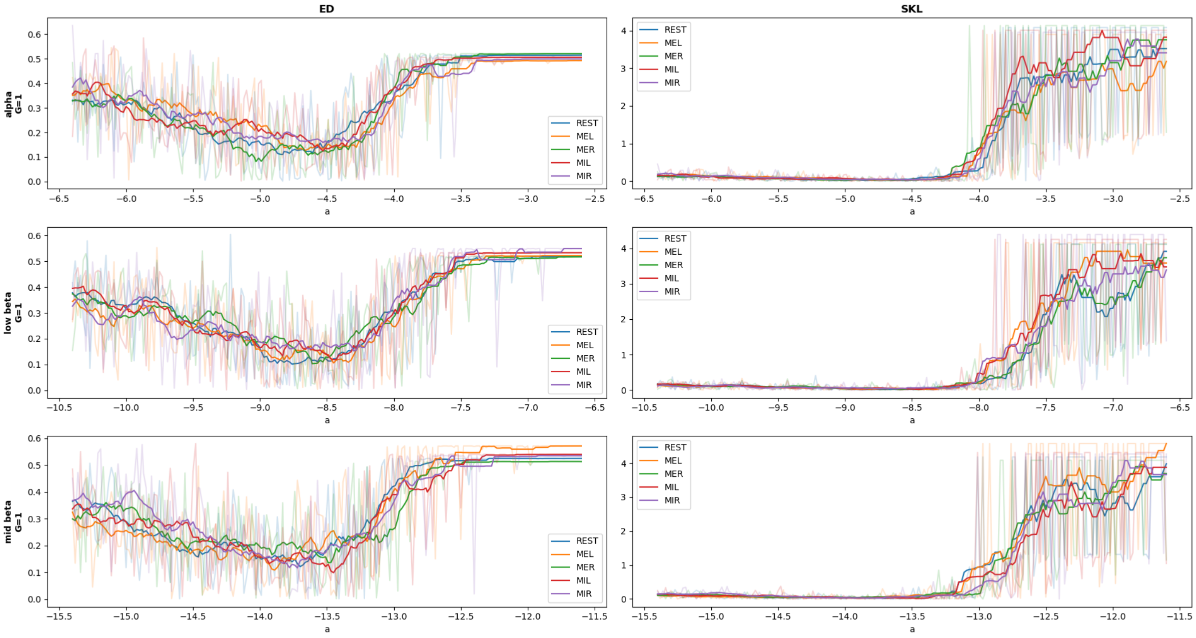

Figure 4.22: a parameter exploration for each task and frequency band with $G = 1$. Each color corresponds to a different task's fit with a moving average filter. The actual fit is displayed in a less opaque color

4.2.4 Final Model

As explained in section 3.7, for each frequency band, FC metric, and for each task the fully fitted model is used to simulate 500 FCs, each with 50 epochs of simulated data. Figure 4.23 presents simulated alpha Resting State Functional Connectivity for the different SC and EC, using *a* and *G* parameters found in the previous fits that maximize similarity between empirical and simulated FC. Using EC drastically improves the fit and also allows for the possibility of distinguishing task types through simulations, which was not possible using the *a* and *G* parameters.

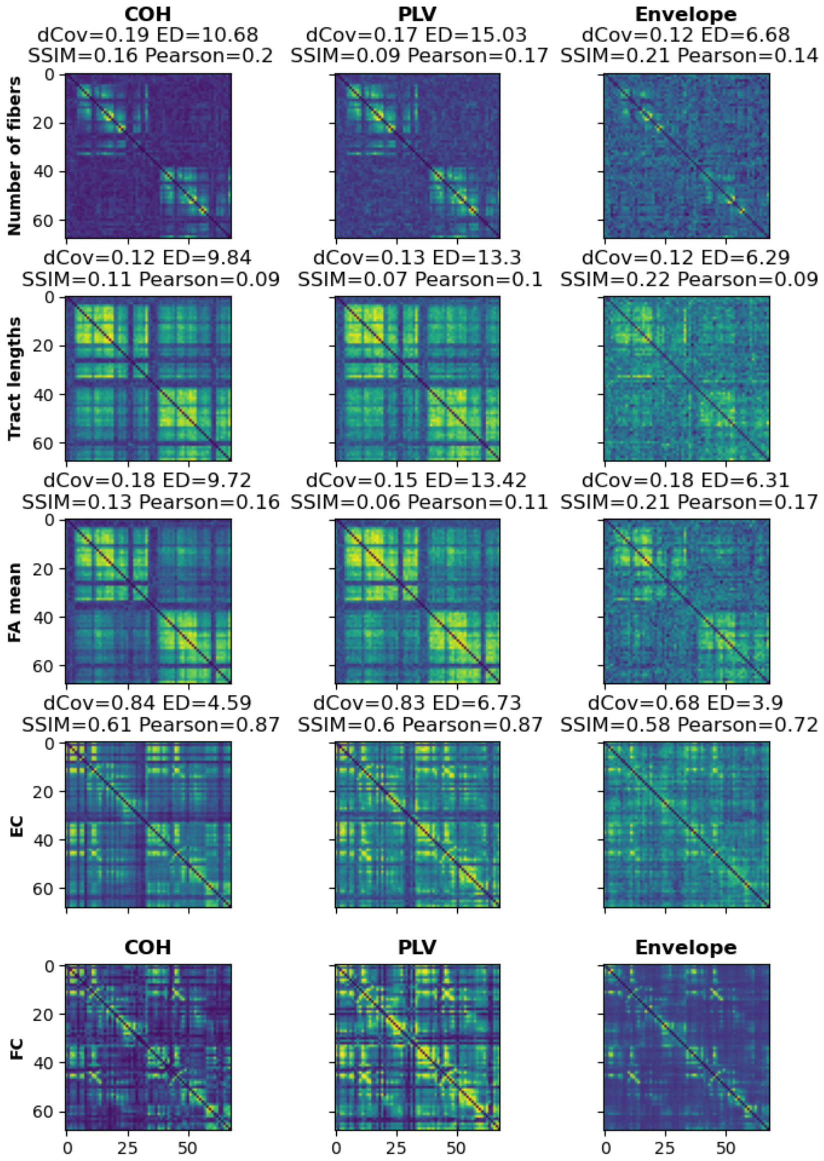

Figure 4.23: Simulated FC for the alpha frequency band using: the number of fibers as adjacency matrix, C, $a = -4.5$ and $G = 4$ (show on the first row); the Tract Lengths as adjacency matrix, C, $a = -4.5$ and $G = 1$ (show on the second row); the FA mean as adjacency matrix, C, $a = -4.5$ and $G = 1$ (show on the third row). On the last row the empirical FC is displayed for comparison. Every FC was simulated according to the a and G parameters that maximized similarity. The similarity between each simulated FC and the empirical FC are displayed above them using the metrics mentioned 3.6

The Euclidean Distance between each task's FC was calculated as done for the empirical data, shown in figure 4.24 and 4.10. Here the results showed allow us to draw the similar conclusion that MEL-MER, MIL-MIR and MEL-MIR show the highest ED. Non-REST comparisons exhibit stronger differences but PLV and COH now have very similar means 1.08 ± 0.23 and 1.02 ± 0.22, respectively. There is a high correlation between the simulated and empirical ED, shown in table 4.11.

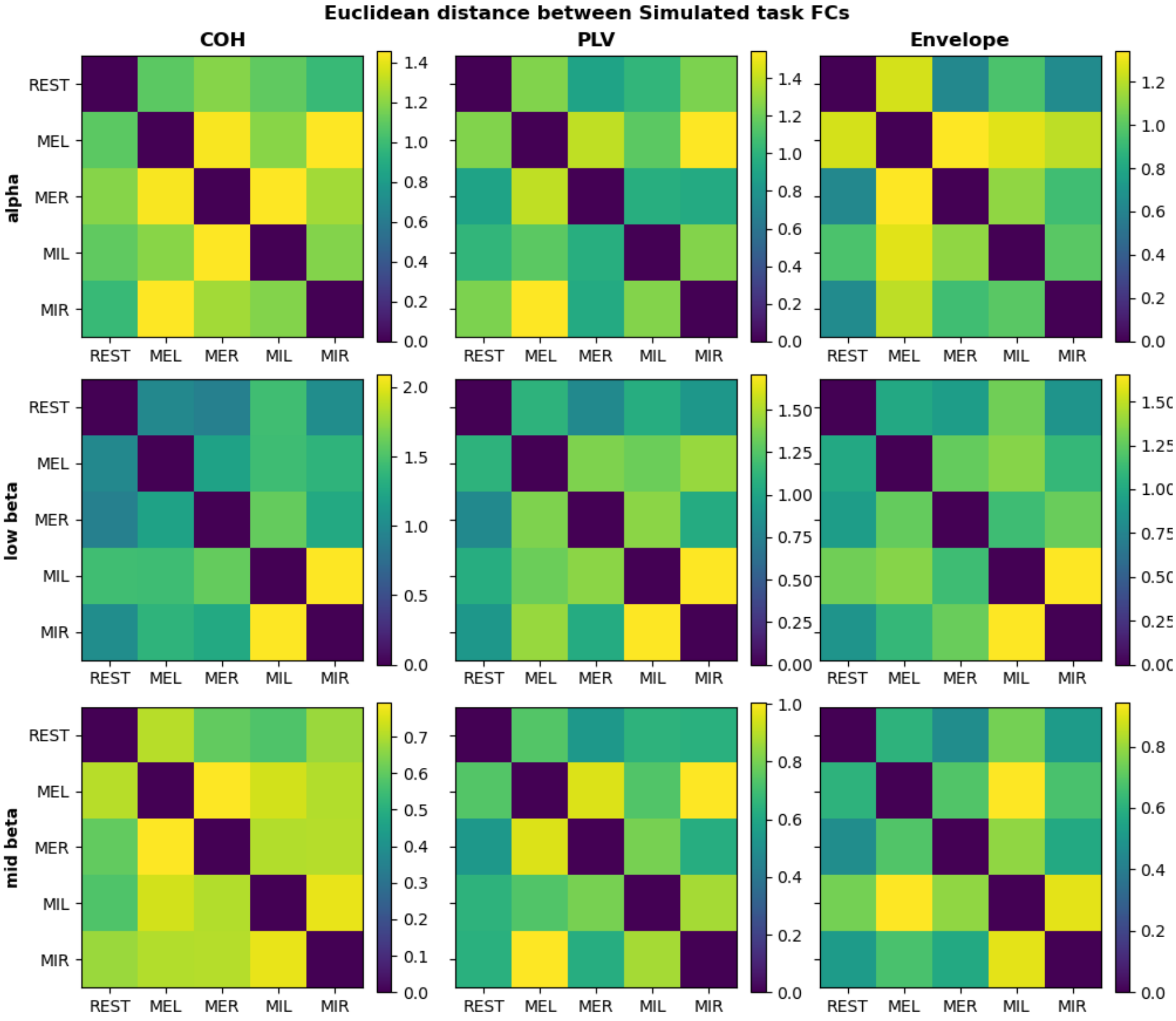

Figure 4.24: Euclidean Distance between each simulated task's FC for all frequencies and methods

Table 4.10: Euclidean Distance between simulated task's FC for all frequency bands and methods with green and blue being values above 50th and 90th percentile of each method

	COH			PLV			Envelope			
	alpha	low beta	mid beta	alpha	low beta	mid beta	alpha	low beta	mid beta	mean
REST-MEL	1.088	1.25	1.25	0.975	1.105	0.998	0.71	0.74	0.611	0.97
REST-MER	1.194	0.894	0.625	0.911	0.809	0.923	0.604	0.537	0.464	0.77
REST-MIL	1.099	1.016	0.960	1.45	1.065	1.30	0.574	0.652	0.75	0.98
REST-MIR	0.983	1.24	0.644	1.026	0.905	0.856	0.675	0.637	0.520	0.83
MEL-MER	1.44	1.39	1.34	1.207	1.38	1.26	0.79	0.95	0.69	1.16
MEL-MIL	1.20	1.151	1.28	1.44	1.33	1.36	0.74	0.732	0.94	1.13
MEL-MIR	1.46	1.54	1.20	1.36	1.44	1.102	0.703	1.01	0.672	1.17
MER-MIL	1.46	0.964	1.12	1.59	1.41	1.138	0.703	0.80	0.79	1.11
MER-MIR	1.26	0.943	0.928	1.273	1.049	1.28	0.70	0.628	0.575	0.96
MIL-MIR	1.186	1.25	0.998	2.09	1.71	1.65	0.77	0.87	0.91	1.27
mean	1.24	1.16	1.03	1.33	1.22	1.19	0.7	0.76	0.69	

Table 4.11: Pearson Correlation Coefficient between simulated and empirical task comparison ED shown in 4.24 and 4.4 respectively

method	frequency	correlation
COH	alpha	0.867
COH	low beta	0.908
COH	mid beta	0.874
PLV	alpha	0.95
PLV	low beta	0.939
PLV	mid beta	0.885
Envelope	alpha	0.963
Envelope	low beta	0.799
Envelope	mid beta	0.847

As was done in the empirical dataset, the simulated data is analyzed for statistically significance. The results averaged across node connections are shown in table 4.12. Tables and box-plots are shown in section B.5 (to reduce bloat for each table only differences above a certain value specific to each table where shown). PLV is the most sensitive metric, and Envelope the least. Overall non-REST comparisons still exhibit stronger differences, with the top three remaining unchanged. Despite maintaining the same trend, all the differences are lower in value.

Table 4.12: Average absolute simulated FC task differences for all metrics and frequency bands. Only statistical significant differences ($\alpha < 0.05$) were considered

metric	frequency	REST-MEL	REST-MER	REST-MIL	REST-MIR	MEL-MER	MEL-MIL	MEL-MIR	MER-MIL	MER-MIR	MIL-MIR	mean
COH	alpha	0.0185	0.0197	0.0183	0.0173	0.0243	0.0196	0.0242	0.0243	0.0214	0.0195	0.0207
	low beta	0.021	0.0159	0.0178	0.0225	0.0241	0.0194	0.0265	0.0163	0.0167	0.0209	0.0201
	mid beta	0.0212	0.0109	0.0167	0.0108	0.0223	0.0219	0.02	0.0193	0.0155	0.0167	0.0175
Envelope	alpha	0.0119	0.0101	0.0095	0.0119	0.013	0.0125	0.0119	0.0114	0.012	0.013	0.0117
	low beta	0.0129	0.0093	0.0109	0.0105	0.0169	0.0122	0.0177	0.014	0.0105	0.0146	0.0129
	mid beta	0.0106	0.0079	0.013	0.0086	0.0113	0.0159	0.0109	0.0132	0.0094	0.0156	0.0117
PLV	alpha	0.0159	0.0152	0.0251	0.0178	0.0197	0.024	0.0225	0.0267	0.0222	0.0358	0.0225
	low beta	0.0185	0.013	0.0178	0.0152	0.0231	0.0227	0.0245	0.0234	0.0169	0.0282	0.0203
	mid beta	0.0162	0.0153	0.0226	0.0142	0.0203	0.0224	0.0178	0.0194	0.0215	0.0278	0.0197
	mean	0.0163	0.013	0.0168	0.0143	0.0195	0.019	0.0196	0.0187	0.0162	0.0213	

4.2.4.1 Overlap between Statistical Significant Differences

The overlap between the empirical and simulated statistical significant differences is then calculated to gives another indicator of the model's performance. Each metric is permutation tested with 10000 permutations and FDR corrected.

The overlap in statistical significant differences for each connection, is shown in full in table B.10 and averaged across frequency bands, FC metrics and task comparisons in table 4.13. The model shows an extremely high PPV and TPR, indicating it is very reliable and a simulated significant difference is most likely correct, matching the empirical data as well as that most differences are being simulated. Despite this, TNR and NPV are low indicating that empirically connections showing no significant difference can show a difference in the simulation. This might happen as there is a large class disparity, with most nodes showing significant differences.

Envelope has the best PPV but lowest TPR, so it is more conservative that the other FC metrics. COH is the opposite showing the highest TPR and lowest PPV indicating it finds more True Positive however it has also less accurate. Something similar is seen with brain states: REST comparisons are less accurate when compared non-REST ones; MEL-MER, MIL-MIR and MEL-MIR show the highest performance, with non REST comparisons being inferior in accordance with the empirical analysis.

Table 4.13: Average overlap metrics for each task comparison, FC method, and frequency band

	PPV	TPR	NPV	TNR
MIL-MIR	0.900 ± 0.019	0.877 ± 0.048	0.162 ± 0.045	0.200 ± 0.091
MEL-MER	0.915 ± 0.010	0.867 ± 0.054	0.158 ± 0.028	0.230 ± 0.078
MEL-MIR	0.908 ± 0.011	0.864 ± 0.074	0.161 ± 0.034	0.225 ± 0.109
MEL-MIL	0.906 ± 0.017	0.856 ± 0.051	0.172 ± 0.035	0.249 ± 0.081
MER-MIL	0.909 ± 0.014	0.838 ± 0.059	0.160 ± 0.029	0.268 ± 0.098
REST-MIL	0.884 ± 0.022	0.835 ± 0.087	0.191 ± 0.040	0.252 ± 0.102
REST-MEL	0.898 ± 0.008	0.833 ± 0.064	0.187 ± 0.040	0.278 ± 0.075
MER-MIR	0.901 ± 0.020	0.827 ± 0.084	0.179 ± 0.033	0.287 ± 0.129
REST-MIR	0.882 ± 0.020	0.804 ± 0.084	0.189 ± 0.033	0.289 ± 0.102
REST-MER	0.885 ± 0.018	0.788 ± 0.088	0.202 ± 0.029	0.338 ± 0.127
COH	0.887 ± 0.020	0.903 ± 0.028	0.197 ± 0.039	0.169 ± 0.036
PLV	0.894 ± 0.012	0.847 ± 0.045	0.186 ± 0.029	0.259 ± 0.074
Envelope	0.914 ± 0.013	0.760 ± 0.055	0.149 ± 0.020	0.367 ± 0.075
low beta	0.900 ± 0.018	0.846 ± 0.070	0.181 ± 0.039	0.255 ± 0.086
alpha	0.896 ± 0.016	0.839 ± 0.076	0.178 ± 0.036	0.260 ± 0.118
mid beta	0.898 ± 0.023	0.827 ± 0.075	0.173 ± 0.035	0.276 ± 0.108

Chapter 5

Conclusions

The aim of this thesis was to build a Brain Network Model that not only models motor execution and imagery, but would also allow for further study in the context of electric stimulation and neural pathologies. EEG data recorded from 21 healthy right-handed subjects during rest, left and right handed motor execution and imagery tasks was used to calculate Functional Connectivity. Two approaches were taken to analyse the FC: the Euclidean Distance (ED) between the grand average FC of each task; a statistical analysis of the differences in FC for each element at every individual connection. Both approaches gave similar results, with MEL-MER, MIL-MIR and MEL-MIR showing the largest differences. Of the three FC metrics used (COH, PLV, Envelope) PLV shows the largest differences between tasks followed by COH, with Envelope showing the least.

The normal form of the Hopf bifurcation, used to model the dynamics of neuron populations, has a bifurcation at $a = 0$ and it is in this region that it best models brain activity [36, 35, 78, 56, 34]. It was verified that the bifurcation is shifted to the left of 0 at higher frequencies, with a higher frequency requiring a bigger shift. This does not occur at the lower frequencies used in fMRI. Once the shifted a parameter was found, the model worked as expected supporting the necessity of accounting for the impact of frequency in 'a'.

The a and G parameter exploration was done across frequency bands, FC metrics, and SCs, the C parameter. The G parameter exploration, done with the a parameter set at the bifurcation location. FA mean and Tract Lengths show similar trend with FA mean achieving a superior score in almost every metric except the ED where the results are very similar. While the number of fibers can achieve similar metric scores, the explorations tend to be constant with a growing G value, FA mean shows a higher tendency to form unique solutions (maximum or minimum). Analyzing the a parameter exploration there is generally a decrease in similarity as the model starts fully oscillating. Outside the oscillating regime, as the a value increase the similarity is either constant or there is a slight increase until the bifurcation. Both parameters behave in the same manner across tasks as expected, since the brain states are very similar and their slight differences would manifest in such global variables.

For the EC fit, a first approach was taken where the EC was fitted with the three possible SC and no difference was found. Since the FA mean determined allowed for the best a and G parameter exploration it was chosen as the starting point of the definitive initial EC fit. An EC was fitted for each FC metric, frequency band and task. The analysis of the final ECs reflected the results obtained in the initial analysis of the FC however, despite PLV initially being the most sensitive to differences in brain states, the EC matrix fitted using the COH FC shows larger differences when compared to the one fitted using the PLV metric. The a and G parameters were re-explored using the EC instead of the SC showing a drastically higher similarity and less noisy behavior. Across different tasks there is still no apparent difference. The

ED, when compared to other metrics, shows much more constrained results and might be a key metric when exploring other brain states that differ significantly such has neural pathologies.

Other than the FC, three other metrics were fitted for: coherence, metastability, and PMS obtained through LEiDA. Global coherence is defined as the temporal average of the Kuramoto Order Parameter and reflects the overall level of synchronization across brain regions. This metric is very well constrained by the global coupling parameter G and the model is able to replicate the empirical values. Further analysis indicates: higher synchronization at the beta frequency bands compared to the alpha band; higher synchronization in right handed tasks when compared to left handed tasks further supported by the FC analysis that showed left and right handed tasks have the highest distinction, which may be related to all of the data being gathered from right-handed individuals. Metastability is defined as the temporal average of the Kuramoto Order Parameter and reflects variation in synchronization over time. The model is able to simulate activity with the empirical metastability, however the G parameter has very little effect on it, which is translated in a very low value of R^2. Because of this, we conclude that results obtained from this metric may not be very reliable. LEiDA is a fairly recent technique and has only been applied to fMRI data. The optimal number of PMS identified from the cluster analysis is two which, although feasible, does not lead to any useful or new insights about the studied brain states. It seems that LEiDA can be used successfully on EEG data, however adjustments might be required to produce useful insights. Similar to the results obtained from metastability, the model is able to reproduce empirical results, possibly due to the EC, however other parameters have little to no effect on it. This indicates that the model has the possibility to successfully replicate dynamic behavior but there is not a method to adjust or control it.

Overall, the final model is able to reproduce the empirical FC with very high similarity across frequency bands and metrics. Moreover, the differences between brain states are not only captured globally but are also simulated with high precision and sensitivity at the node and connection levels. However, despite this strong correspondence in static connectivity, the model still presents limitations in reproducing realistic temporal dynamics. These results highlight both the strength of the model as a mechanistic framework for Functional Connectivity and the need for further refinements to better capture the transient, dynamical aspects of brain activity.

Although this thesis focused exclusively on Resting State and motor-related (Motor Execution and Motor Imagery (MI)) EEG data, the modeling framework developed here provides a foundation for broader applications. In future work, this approach will be extended to the study of neural pathologies and the effects of electrical stimulation. Given that the current model successfully reproduces FC and state-dependent differences in healthy conditions—and considering that Hopf-based whole-brain models have already been effectively applied to simulate alterations in brain dynamics associated with neurological disorders and stimulation paradigms—the extension of this framework to pathological brain states is expected to yield even more distinct and interpretable differences, further validating its clinical and theoretical relevance.

Bibliography

[1] Priyanka A. Abhang, Bharti W. Gawali, and Suresh C. Mehrotra. “Chapter 1 - Introduction to Emotion, Electroencephalography, and Speech Processing”. In: *Introduction to EEG- and Speech-Based Emotion Recognition*. Ed. by Priyanka A. Abhang, Bharti W. Gawali, and Suresh C. Mehrotra. Academic Press, 2016, pp. 1–17. ISBN: 978-0-12-804490-2. DOI: `https://doi.org/10.1016/B978-0-12-804490-2.00001-4`. URL: `https://www.sciencedirect.com/science/article/pii/B9780128044902000014`.

[2] Priyanka A. Abhang, Bharti W. Gawali, and Suresh C. Mehrotra. “Chapter 2 - Technological Basics of EEG Recording and Operation of Apparatus”. In: *Introduction to EEG- and Speech-Based Emotion Recognition*. Ed. by Priyanka A. Abhang, Bharti W. Gawali, and Suresh C. Mehrotra. Academic Press, 2016, pp. 19–50. ISBN: 978-0-12-804490-2. DOI: `https://doi.org/10.1016/B978-0-12-804490-2.00002-6`. URL: `https://www.sciencedirect.com/science/article/pii/B9780128044902000026`.

[3] Priyanka A. Abhang, Bharti W. Gawali, and Suresh C. Mehrotra. “Chapter 3 - Technical Aspects of Brain Rhythms and Speech Parameters”. In: *Introduction to EEG- and Speech-Based Emotion Recognition*. Ed. by Priyanka A. Abhang, Bharti W. Gawali, and Suresh C. Mehrotra. Academic Press, 2016, pp. 51–79. ISBN: 978-0-12-804490-2. DOI: `https://doi.org/10.1016/B978-0-12-804490-2.00003-8`. URL: `https://www.sciencedirect.com/science/article/pii/B9780128044902000038`.

[4] Seppo P. Ahlfors and Matti S. Hämäläinen. “MEG and EEG: source estimation”. In: *Handbook of Neural Activity Measurement*. Ed. by Romain Brette and AlainEditors Destexhe. Cambridge University Press, 2012, pp. 257–286. DOI: `10.1017/CBO9780511979958.007`.

[5] Elena A Allen et al. “Tracking whole-brain connectivity dynamics in the resting state”. en. In: *Cereb. Cortex* 24.3 (Mar. 2014), pp. 663–676.

[6] Colin Andrew and Gert Pfurtscheller. “Event-related coherence as a tool for studying dynamic interaction of brain regions”. In: *Electroencephalography and Clinical Neurophysiology* 98.2 (1996), pp. 144–148. ISSN: 0013-4694. DOI: `https://doi.org/10.1016/0013-4694(95)00228-6`. URL: `https://www.sciencedirect.com/science/article/pii/0013469495002286`.

[7] Shiva Asadzadeh et al. “A systematic review of EEG source localization techniques and their applications on diagnosis of brain abnormalities”. en. In: *J Neurosci Methods* 339 (Apr. 2020), p. 108740.

[8] Sergul Aydore, Dimitrios Pantazis, and Richard M Leahy. “A note on the phase locking value and its properties”. en. In: *Neuroimage* 74 (Feb. 2013), pp. 231–244.

[9] Sergul Aydore, Dimitrios Pantazis, and Richard M Leahy. “A note on the phase locking value and its properties”. en. In: *Neuroimage* 74 (Feb. 2013), pp. 231–244.

[10] Kanika Bansal, Johan Nakuci, and Sarah Feldt Muldoon. “Personalized brain network models for assessing structure–function relationships”. en. In: *Curr. Opin. Neurobiol.* 52 (Oct. 2018), pp. 42–47.

[11] Kanika Bansal et al. “Cognitive chimera states in human brain networks”. en. In: *Sci. Adv.* 5.4 (Apr. 2019), eaau8535.

[12] Kanika Bansal et al. “Data-driven brain network models differentiate variability across language tasks”. en. In: *PLoS Comput. Biol.* 14.10 (Oct. 2018), e1006487.

[13] André M. Bastos and Jan-Mathijs Schoffelen. “A Tutorial Review of Functional Connectivity Analysis Methods and Their Interpretational Pitfalls”. In: *Frontiers in Systems Neuroscience* Volume 9 - 2015 (2016). ISSN: 1662-5137. DOI: `10.3389/fnsys.2015.00175`. URL: `https://www.frontiersin.org/journals/systems-neuroscience/articles/10.3389/fnsys.2015.00175`.

[14] Claude Bédard and Alain Destexhe. “Local field potentials”. In: *Handbook of Neural Activity Measurement*. Ed. by Romain Brette and AlainEditors Destexhe. Cambridge University Press, 2012, pp. 136–191.

[15] Philip R. Bevington and D. Keith Robinson. *Data reduction and error analysis for the physical sciences*. 2003.

[16] Michael Breakspear. “Dynamic models of large-scale brain activity”. In: *Nature Neuroscience* 20.3 (Mar. 2017), pp. 340–352. ISSN: 1546-1726. DOI: `10.1038/nn.4497`. URL: `https://doi.org/10.1038/nn.4497`.

[17] Romain Brette and Alain Destexhe. “Intracellular recording”. In: *Handbook of Neural Activity Measurement*. Ed. by Romain Brette and AlainEditors Destexhe. Cambridge University Press, 2012, pp. 44–91.

[18] Romain Brette and Alain Destexhe. “Introduction”. In: *Handbook of Neural Activity Measurement*. Ed. by Romain Brette and AlainEditors Destexhe. Cambridge University Press, 2012, pp. 1–7.

[19] Jeffrey W Britton et al. *Electroencephalography (EEG): An Introductory Text and Atlas of Normal and Abnormal Findings in Adults, Children, and Infants*. en. Chicago: American Epilepsy Society, 2016.

[20] Ricardo Bruña, Fernando Maestú, and Ernesto Pereda. “Phase locking value revisited: teaching new tricks to an old dog”. In: *J. Neural Eng.* 15.5 (Oct. 2018), p. 056011.

[21] Joana Cabral, Morten L. Kringelbach, and Gustavo Deco. “Functional connectivity dynamically evolves on multiple time-scales over a static structural connectome: Models and mechanisms”. In: *NeuroImage* 160 (2017). Functional Architecture of the Brain, pp. 84–96. ISSN: 1053-8119. DOI: `https://doi.org/10.1016/j.neuroimage.2017.03.045`. URL: `https://www.sciencedirect.com/science/article/pii/S1053811917302537`.

[22] Joana Cabral et al. “Cognitive performance in healthy older adults relates to spontaneous switching between states of functional connectivity during rest”. In: *Scientific Reports* 7.1 (July 2017), p. 5135. ISSN: 2045-2322. DOI: `10.1038/s41598-017-05425-7`. URL: `https://doi.org/10.1038/s41598-017-05425-7`.

[23] Joana Cabral et al. “Exploring mechanisms of spontaneous functional connectivity in MEG: How delayed network interactions lead to structured amplitude envelopes of band-pass filtered oscillations”. In: *NeuroImage* 90 (2014), pp. 423–435. ISSN: 1053-8119. DOI: `https://doi.org/10.1016/j.neuroimage.2013.11.047`. URL: `https://www.sciencedirect.com/science/article/pii/S1053811913011968`.

[24] Joana Cabral et al. “Metastable oscillatory modes emerge from synchronization in the brain spacetime connectome”. In: *Communications Physics* 5.1 (July 2022), p. 184.

[25] Joana Cabral et al. “Role of local network oscillations in resting-state functional connectivity”. In: *NeuroImage* 57.1 (2011), pp. 130–139. ISSN: 1053-8119. DOI: `https://doi.org/10.1016/j.neuroimage.2011.04.010`. URL: `https://www.sciencedirect.com/science/article/pii/S1053811911003880`.

[26] G.C. Carter. “Coherence and time delay estimation”. In: *Proceedings of the IEEE* 75.2 (1987), pp. 236–255. DOI: `10.1109/PROC.1987.13723`.

[27] Francesca Castaldo et al. “Multi-modal and multi-model interrogation of large-scale functional brain networks”. In: *NeuroImage* 277 (2023), p. 120236. ISSN: 1053-8119. DOI: `https://doi.org/10.1016/j.neuroimage.2023.120236`. URL: `https://www.sciencedirect.com/science/article/pii/S1053811923003877`.

[28] Catie Chang and Gary H Glover. “Time-frequency dynamics of resting-state brain connectivity measured with fMRI”. en. In: *Neuroimage* 50.1 (Mar. 2010), pp. 81–98.

[29] Mike X Cohen. *Analyzing Neural Time Series Data: Theory and Practice*. The MIT Press, Jan. 2014. ISBN: 9780262319553. DOI: `10.7551/mitpress/9609.001.0001`. URL: `https://doi.org/10.7551/mitpress/9609.001.0001`.

[30] Jan De Munck, Carsten Wolters, and Maureen Clerc. “EEG and MEG: forward modeling”. In: *Handbook of Neural Activity Measurement*. Ed. by Romain Brette and AlainEditors Destexhe. Cambridge University Press, 2012, pp. 192–256. DOI: `10.1017/CBO9780511979958.006`.

[31] Gustavo Deco and Morten L. Kringelbach. “Great Expectations: Using Whole-Brain Computational Connectomics for Understanding Neuropsychiatric Disorders”. In: *Neuron* 84.5 (2014), pp. 892–905. ISSN: 0896-6273. DOI: `https://doi.org/10.1016/j.neuron.2014.08.034`. URL: `https://www.sciencedirect.com/science/article/pii/S0896627314007351`.

[32] Gustavo Deco et al. “Awakening: Predicting external stimulation to force transitions between different brain states”. In: *Proceedings of the National Academy of Sciences* 116.36 (2019), pp. 18088–18097. DOI: `https://doi.org/10.1073/pnas.1905534116`. eprint: `https://www.pnas.org/doi/pdf/10.1073/pnas.1905534116`. URL: `https://www.pnas.org/doi/abs/10.1073/pnas.1905534116`.

[33] Gustavo Deco et al. “Perturbation of whole-brain dynamics in silico reveals mechanistic differences between brain states”. In: *NeuroImage* 169 (2018), pp. 46–56. ISSN: 1053-8119. DOI: `https://doi.org/10.1016/j.neuroimage.2017.12.009`. URL: `https://www.sciencedirect.com/science/article/pii/S1053811917310236`.

[34] Gustavo Deco et al. “Single or multiple frequency generators in on-going brain activity: A mechanistic whole-brain model of empirical MEG data”. In: *NeuroImage* 152 (2017), pp. 538–550. ISSN: 1053-8119. DOI: `https://doi.org/10.1016/j.neuroimage.2017.03.023`. URL: `https://www.sciencedirect.com/science/article/pii/S105381191730232X`.

[35] Gustavo Deco et al. “The dynamics of resting fluctuations in the brain: metastability and its dynamical cortical core”. In: *Scientific Reports* 7.1 (June 2017), p. 3095. ISSN: 2045-2322. DOI: `10.1038/s41598-017-03073-5`. URL: `https://doi.org/10.1038/s41598-017-03073-5`.

[36] Murat Demirtaş et al. “A whole-brain computational modeling approach to explain the alterations in resting-state functional connectivity during progression of Alzheimer’s disease”. In: *NeuroImage: Clinical* 16 (2017), pp. 343–354. ISSN: 2213-1582. DOI: `https://doi.org/10.1016/j.nicl.2017.08.006`. URL: `https://www.sciencedirect.com/science/article/pii/S2213158217301961`.

[37] Murat Demirtaş et al. “Distinct modes of functional connectivity induced by movie-watching”. en. In: *Neuroimage* 184 (Sept. 2018), pp. 335–348.

[38] Rahul S Desikan et al. “An automated labeling system for subdividing the human cerebral cortex on MRI scans into gyral based regions of interest”. en. In: *Neuroimage* 31.3 (Mar. 2006), pp. 968–980.

[39] Patricio Donnelly-Kehoe et al. “Reliable local dynamics in the brain across sessions are revealed by whole-brain modeling of resting state activity”. In: *Human Brain Mapping* 40.10 (2019), pp. 2967–2980. DOI: `https://doi.org/10.1002/hbm.24572`. eprint: `https://onlinelibrary.wiley.com/doi/pdf/10.1002/hbm.24572`. URL: `https://onlinelibrary.wiley.com/doi/abs/10.1002/hbm.24572`.

[40] Denis A. Engemann and Alexandre Gramfort. “Automated model selection in covariance estimation and spatial whitening of MEG and EEG signals”. In: *NeuroImage* 108 (2015), pp. 328–342. ISSN: 1053-8119. DOI: `https://doi.org/10.1016/j.neuroimage.2014.12.040`. URL: `https://www.sciencedirect.com/science/article/pii/S1053811914010325`.

[41] Tae-Hoon Eom. “Electroencephalography source localization”. en. In: *Clin. Exp. Pediatr.* 66.5 (May 2023), pp. 201–209.

[42] Holger Finger et al. “Modeling of Large-Scale Functional Brain Networks Based on Structural Connectivity from DTI: Comparison with EEG Derived Phase Coupling Networks and Evaluation of Alternative Methods along the Modeling Path”. en. In: *PLoS Comput Biol* 12.8 (Aug. 2016), e1005025.

[43] Bruce Fischl. “FreeSurfer”. en. In: *Neuroimage* 62.2 (Jan. 2012), pp. 774–781.

[44] Bruce Fischl et al. “High-resolution intersubject averaging and a coordinate system for the cortical surface”. In: *Human Brain Mapping* 8.4 (1999), pp. 272–284. DOI: `https://doi.org/10.1002/(SICI)1097-0193(1999)8:4<272::AID-HBM10>3.0.CO;2-4`. eprint: `https://onlinelibrary.wiley.com/doi/pdf/10.1002/%28SICI%291097-0193%281999%298%3A4%3C272%3A%3AAID-HBM10%3E3.0.CO%3B2-4`. URL: `https://onlinelibrary.wiley.com/doi/abs/10.1002/%28SICI%291097-0193%281999%298%3A4%3C272%3A%3AAID-HBM10%3E3.0.CO%3B2-4`.

[45] Karl J Friston. “Functional and effective connectivity: a review”. en. In: *Brain Connect* 1.1 (2011), pp. 13–36.

[46] Katharina Glomb et al. “Computational Models in Electroencephalography”. In: *Brain Topography* 35.1 (Jan. 2022), pp. 142–161. ISSN: 1573-6792. DOI: `10.1007/s10548-021-00828-2`. URL: `https://doi.org/10.1007/s10548-021-00828-2`.

[47] Alexandre Gramfort et al. “MEG and EEG data analysis with MNE-Python”. In: *Frontiers in Neuroscience* 7 (2013). ISSN: 1662-453X. DOI: `10.3389/fnins.2013.00267`. URL: `https://www.frontiersin.org/journals/neuroscience/articles/10.3389/fnins.2013.00267`.

[48] Roberta Grech et al. “Review on solving the inverse problem in EEG source analysis”. In: *Journal of NeuroEngineering and Rehabilitation* 5.1 (Nov. 2008), p. 25.

[49] Gerald Hahn et al. “A new computational approach to estimate whole-brain effective connectivity from functional and structural MRI, applied to language development”. In: *Scientific Reports* 9.1 (June 2019), p. 8479. ISSN: 2045-2322. DOI: `10.1038/s41598-019-44909-6`. URL: `https://doi.org/10.1038/s41598-019-44909-6`.

[50] Jonathan J. Halford et al. *Handbook of EEG Interpretation*. Ed. by William O. Tatum. Springer Publishing Company, 2021, p. 422. ISBN: 978-0-8261-4708-0. DOI: `10.1891/9780826147097`. URL: `https://connect.springerpub.com/content/book/978-0-8261-4709-7`.

[51] Hans Hallez et al. “Review on solving the forward problem in EEG source analysis”. In: *Journal of NeuroEngineering and Rehabilitation* 4.1 (Nov. 2007), p. 46. ISSN: 1743-0003. DOI: `10.1186/1743-0003-4-46`. URL: `https://doi.org/10.1186/1743-0003-4-46`.

[52] Daniel A Handwerker et al. “Periodic changes in fMRI connectivity”. en. In: *Neuroimage* 63.3 (Nov. 2012), pp. 1712–1719.

[53] Bin He et al. “Electrophysiological imaging of brain activity and connectivity-challenges and opportunities”. en. In: *IEEE Trans Biomed Eng* 58.7 (Apr. 2011), pp. 1918–1931.

[54] Bin He et al. “Electrophysiological Source Imaging: A Noninvasive Window to Brain Dynamics”. en. In: *Annu Rev Biomed Eng* 20 (Mar. 2018), pp. 171–196.

[55] Ignacio Perez Ipiña et al. “Modeling regional changes in dynamic stability during sleep and wakefulness”. In: *NeuroImage* 215 (2020), p. 116833. ISSN: 1053-8119. DOI: `https://doi.org/10.1016/j.neuroimage.2020.116833`. URL: `https://www.sciencedirect.com/science/article/pii/S1053811920303207`.

[56] Beatrice M. Jobst et al. “Increased Stability and Breakdown of Brain Effective Connectivity During Slow-Wave Sleep: Mechanistic Insights from Whole-Brain Computational Modelling”. In: *Scientific Reports* 7.1 (July 2017), p. 4634. ISSN: 2045-2322. DOI: `10.1038/s41598-017-04522-x`. URL: `https://doi.org/10.1038/s41598-017-04522-x`.

[57] Csaba Kerepesi et al. “The braingraph.org database of high resolution structural connectomes and the brain graph tools”. In: *Cognitive Neurodynamics* 11.5 (Oct. 2017), pp. 483–486.

[58] Christopher K. Kovach. “A Biased Look at Phase Locking: Brief Critical Review and Proposed Remedy”. In: *IEEE Transactions on Signal Processing* 65.17 (Sept. 2017), pp. 4468–4480. ISSN: 1941-0476. DOI: `10.1109/tsp.2017.2711517`. URL: `http://dx.doi.org/10.1109/TSP.2017.2711517`.

[59] Morten L Kringelbach and Gustavo Deco. “Brain States and Transitions: Insights from Computational Neuroscience”. en. In: *Cell Rep* 32.10 (Sept. 2020), p. 108128.

[60] Danielle L. Kurtin et al. “Moving from phenomenological to predictive modelling: Progress and pitfalls of modelling brain stimulation in-silico”. In: *NeuroImage* 272 (2023), p. 120042. ISSN: 1053-8119. DOI: `https://doi.org/10.1016/j.neuroimage.2023.120042`. URL: `https://www.sciencedirect.com/science/article/pii/S105381192300188X`.

[61] Jean-Philippe Lachaux et al. “Measuring phase synchrony in brain signals”. In: *Human Brain Mapping* 8.4 (1999), pp. 194–208. DOI: `https://doi.org/10.1002/(SICI)1097-0193(1999)8:4<194::AID-HBM4>3.0.CO;2-C`. eprint: `https://onlinelibrary.wiley.com/doi/pdf/10.1002/%28SICI%291097-0193%281999%298%3A4%3C194%3A%3AAID-HBM4%3E3.0.CO%3B2-C`. URL: `https://onlinelibrary.wiley.com/doi/abs/10.1002/%28SICI%291097-0193%281999%298%3A4%3C194%3A%3AAID-HBM4%3E3.0.CO%3B2-C`.

[62] Eric Larson et al. *MNE-Python*. Version v1.8.0. Aug. 2024. DOI: `10.5281/zenodo.13340330`. URL: `https://doi.org/10.5281/zenodo.13340330`.

[63] Fa-Hsuan Lin et al. “Distributed current estimates using cortical orientation constraints”. en. In: *Hum Brain Mapp* 27.1 (Jan. 2006), pp. 1–13.

[64] Ana R. Lopes, Anna Letournel, and Joana Cabral. “Altered resting-state network dynamics in Schizophrenia”. In: *medRxiv* (2020). DOI: `10.1101/2020.07.21.20157347`. eprint: `https://www.medrxiv.org/content/early/2020/07/26/2020.07.21.20157347.full.pdf`. URL: `https://www.medrxiv.org/content/early/2020/07/26/2020.07.21.20157347`.

[65] Fernando Lopes da Silva. “EEG and MEG: relevance to neuroscience”. en. In: *Neuron* 80.5 (Dec. 2013), pp. 1112–1128.

[66] Sheida Malekpour, John A. Gubner, and William A. Sethares. “Measures of generalized magnitude-squared coherence: Differences and similarities”. In: *Journal of the Franklin Institute* 355.5 (2018), pp. 2932–2950. ISSN: 0016-0032. DOI: `https://doi.org/10.1016/j.jfranklin.2018.01.014`. URL: `https://www.sciencedirect.com/science/article/pii/S0016003218300747`.

[67] Fahimeh Mamashli et al. “Permutation Statistics for Connectivity Analysis between Regions of Interest in EEG and MEG Data”. In: *Scientific Reports* 9.1 (May 2019), p. 7942. ISSN: 2045-2322. DOI: `10.1038/s41598-019-44403-z`. URL: `https://doi.org/10.1038/s41598-019-44403-z`.

[68] Christoph M. Michel and Denis Brunet. “EEG Source Imaging: A Practical Review of the Analysis Steps”. In: *Frontiers in Neurology* 10 (2019). ISSN: 1664-2295. DOI: `10.3389/fneur.2019.00325`. URL: `https://www.frontiersin.org/articles/10.3389/fneur.2019.00325`.

[69] Christoph M. Michel and Bin He. “Chapter 6 - EEG source localization”. In: *Clinical Neurophysiology: Basis and Technical Aspects*. Ed. by Kerry H. Levin and Patrick Chauvel. Vol. 160. Handbook of Clinical Neurology. Elsevier, 2019, pp. 85–101. DOI: `https://doi.org/10.1016/B978-0-444-64032-1.00006-0`. URL: `https://www.sciencedirect.com/science/article/pii/B9780444640321000060`.

[70] Christoph M. Michel et al. “EEG source imaging”. In: *Clinical Neurophysiology* 115.10 (2004), pp. 2195–2222. ISSN: 1388-2457. DOI: `https://doi.org/10.1016/j.clinph.2004.06.001`. URL: `https://www.sciencedirect.com/science/article/pii/S1388245704002135`.

[71] J C Mosher, R M Leahy, and P S Lewis. “EEG and MEG: forward solutions for inverse methods”. en. In: *IEEE Trans Biomed Eng* 46.3 (Mar. 1999), pp. 245–259.

[72] John D. Murray, Murat Demirtaş, and Alan Anticevic. "Biophysical Modeling of Large-Scale Brain Dynamics and Applications for Computational Psychiatry". In: *Biological Psychiatry: Cognitive Neuroscience and Neuroimaging* 3.9 (2018). Computational Methods and Modeling in Psychiatry, pp. 777–787. ISSN: 2451-9022. DOI: `https://doi.org/10.1016/j.bpsc.2018.07.004`. URL: `https://www.sciencedirect.com/science/article/pii/S2451902218301782`.

[73] Benjamin L. Ochoa and Serge J. Belongie. "Covariance Propagation for Guided Matching". In: 2006. URL: `https://api.semanticscholar.org/CorpusID:12859410`.

[74] Roberto D. Pascual-Marqui et al. "Comparing EEG/MEG neuroimaging methods based on localization error, false positive activity, and false positive connectivity". In: *bioRxiv* (2018). DOI: `10.1101/269753`. eprint: `https://www.biorxiv.org/content/early/2018/02/22/269753.full.pdf`. URL: `https://www.biorxiv.org/content/early/2018/02/22/269753`.

[75] Anagh Pathak, Dipanjan Roy, and Arpan Banerjee. "Whole-Brain Network Models: From Physics to Bedside". en. In: *Front Comput Neurosci* 16 (May 2022), p. 866517.

[76] Klas H. Pettersen et al. "Extracellular spikes and CSD". In: *Handbook of Neural Activity Measurement*. Ed. by Romain Brette and AlainEditors Destexhe. Cambridge University Press, 2012, pp. 92–135.

[77] Adrián Ponce-Alvarez and Gustavo Deco. "The Hopf whole-brain model and its linear approximation". In: *Scientific Reports* 14.1 (Jan. 2024), p. 2615.

[78] Victor M. Saenger et al. "Uncovering the underlying mechanisms and whole-brain dynamics of deep brain stimulation for Parkinson's disease". In: *Scientific Reports* 7.1 (Aug. 2017), p. 9882. ISSN: 2045-2322. DOI: `10.1038/s41598-017-10003-y`. URL: `https://doi.org/10.1038/s41598-017-10003-y`.

[79] Donald L. Schomer and Fernando H. Lopes da Silva. *Niedermeyer's Electroencephalography: Basic Principles, Clinical Applications, and Related Fields*. Oxford University Press, Nov. 2017. ISBN: 9780190228484. DOI: `10.1093/med/9780190228484.001.0001`. URL: `https://doi.org/10.1093/med/9780190228484.001.0001`.

[80] Donald L. Schomer et al. "1011C40EEG Event-Related Desynchronization and Event-Related Synchronization". In: *Niedermeyer's Electroencephalography: Basic Principles, Clinical Applications, and Related Fields*. Oxford University Press, Nov. 2017. ISBN: 9780190228484. DOI: `10.1093/med/9780190228484.003.0040`. eprint: `https://academic.oup.com/book/0/chapter/305263278/chapter-ag-pdf/44502139/book\_35515\_section\_305263278.ag.pdf`. URL: `https://doi.org/10.1093/med/9780190228484.003.0040`.

[81] Donald L. Schomer et al. "999C39Event-Related Potentials: General Aspects of Methodology and Quantification". In: *Niedermeyer's Electroencephalography: Basic Principles, Clinical Applications, and Related Fields*. Oxford University Press, Nov. 2017. ISBN: 9780190228484. DOI: `10.1093/med/9780190228484.003.0039`. eprint: `https://academic.oup.com/book/0/chapter/305263106/chapter-ag-pdf/44502149/book\_35515\_section\_305263106.ag.pdf`. URL: `https://doi.org/10.1093/med/9780190228484.003.0039`.

[82] Donald L. Schomer et al. "Dynamics of EEGs as Signals of Neuronal Populations: Models and Theoretical Considerations". In: *Niedermeyer's Electroencephalography: Basic Principles, Clinical Applications, and Related Fields*. Oxford University Press, Nov. 2017. ISBN: 9780190228484. DOI: `10.1093/med/9780190228484.003.0003`. eprint: `https://academic.oup.com/book/0/chapter/305246527/chapter-ag-pdf/44502186/book\_35515\_section\_305246527.ag.pdf`. URL: `https://doi.org/10.1093/med/9780190228484.003.0003`.

[83] Mario Senden et al. "Cortical rich club regions can organize state-dependent functional network formation by engaging in oscillatory behavior". In: *NeuroImage* 146 (2017), pp. 561–574. ISSN: 1053-8119. DOI: `https://doi.org/10.1016/j.neuroimage.2016.10.044`. URL: `https://www.sciencedirect.com/science/article/pii/S1053811916306000`.

[84] Vasco Fontes Marques da Silva. "Targeted tDCS in Sensorimotor Networks: A Functional Connectivity Study". MA thesis. Faculty of Sciences of the University of Lisbon, 2023.

[85] Thomas Stieglitz. "Electrodes". In: *Handbook of Neural Activity Measurement*. Ed. by Romain Brette and AlainEditors Destexhe. Cambridge University Press, 2012, pp. 8–43.

[86] P. Stoica and R.L. Moses. *Spectral Analysis of Signals*. Pearson Prentice Hall, 2005. ISBN: 9780131139565. URL: `https://books.google.pt/books?id=h78ZAQAAIAAJ`.

[87] Luke Tait et al. "Network substrates of cognitive impairment in Alzheimer's Disease". In: *Clinical Neurophysiology* 130.9 (2019), pp. 1581–1595. ISSN: 1388-2457. DOI: `https://doi.org/10.1016/j.clinph.2019.05.027`. URL: `https://www.sciencedirect.com/science/article/pii/S1388245719309022`.

[88] Paul Triebkorn et al. "Fifty shades of The Virtual Brain: Converging optimal working points yield biologically plausible electrophysiological and imaging features". In: *bioRxiv* (2024). DOI: `10.1101/2020.03.26.009795`. eprint: `https://www.biorxiv.org/content/early/2024/05/15/2020.03.26.009795.full.pdf`. URL: `https://www.biorxiv.org/content/early/2024/05/15/2020.03.26.009795`.

[89] Martin Vinck et al. "Improved measures of phase-coupling between spikes and the Local Field Potential". In: *Journal of Computational Neuroscience* 33.1 (Aug. 2012), pp. 53–75.

[90] Martin Vinck et al. "The pairwise phase consistency: A bias-free measure of rhythmic neuronal synchronization". In: *NeuroImage* 51.1 (2010), pp. 112–122. ISSN: 1053-8119. DOI: `https://doi.org/10.1016/j.neuroimage.2010.01.073`. URL: `https://www.sciencedirect.com/science/article/pii/S1053811910000959`.

[91] Jakub Vohryzek et al. "Understanding brain states across spacetime informed by whole-brain modelling". en. In: *Philos Trans A Math Phys Eng Sci* 380.2227 (May 2022), p. 20210247.

Appendices

Appendix A

Experimental data

Figure A.1 presents the resting state FC for all subjects. Figures A.2 to A.4 present FC metrics for REST and other tasks (MI and ME of left or right hand). Figures A.5 to A.7 present differences in each FC metric between REST and tasks. The latter were determined only considering subjects included for FC analysis.

A.1 Functional Connectivity

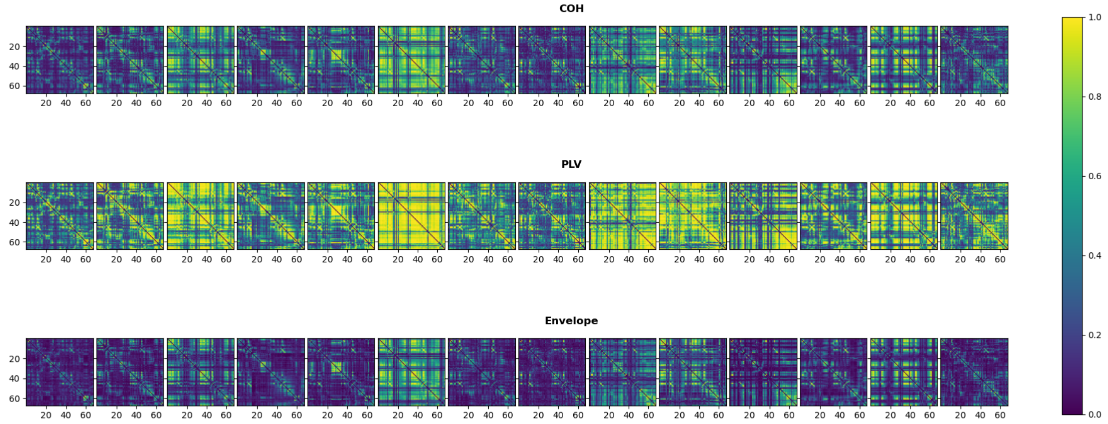

Figure A.1: Resting State Functional Connectivity for all subjects

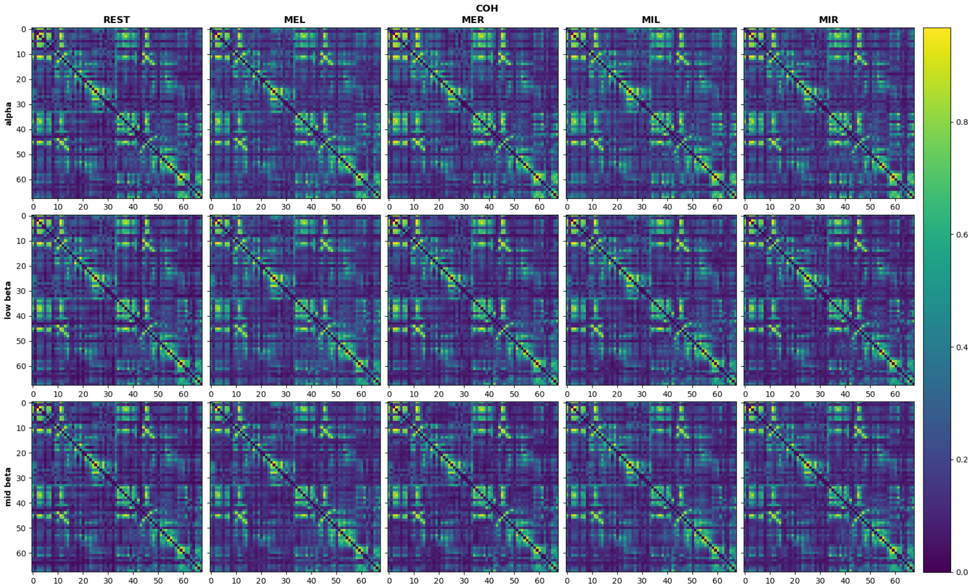

Figure A.2: COH FC during rest and other tasks.

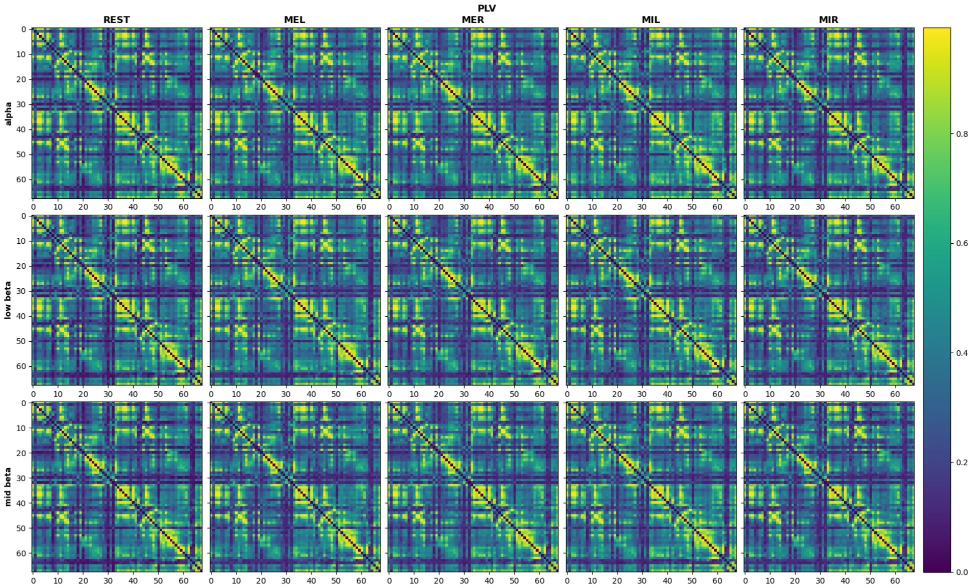

Figure A.3: PLV FC during rest and other tasks.

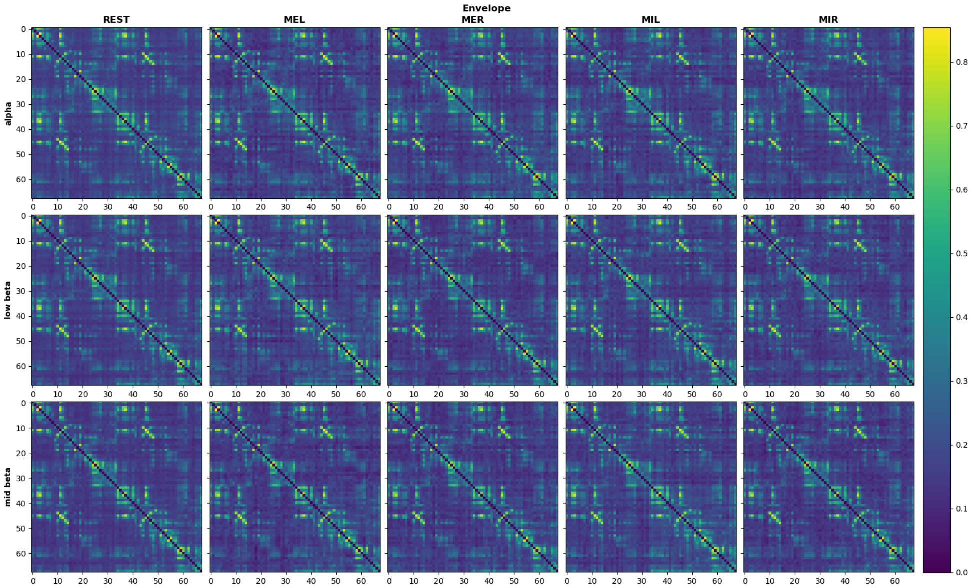

Figure A.4: Envelope FC during rest and other tasks.

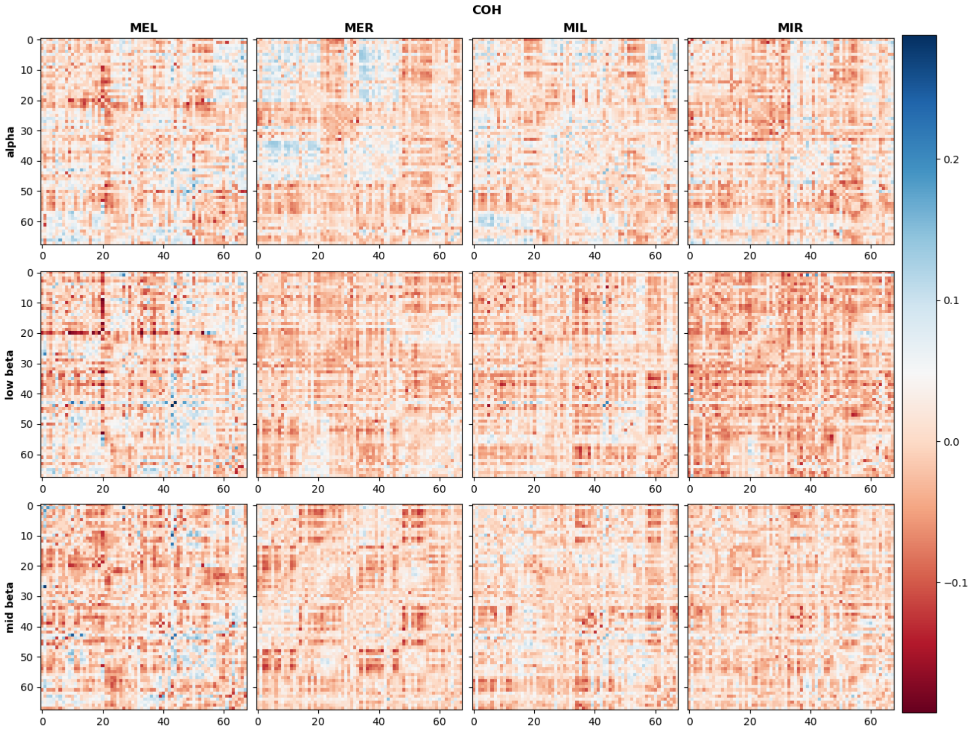

Figure A.5: COH FC difference between rest and other tasks.

Figure A.6: PLV FC difference between rest and other tasks.

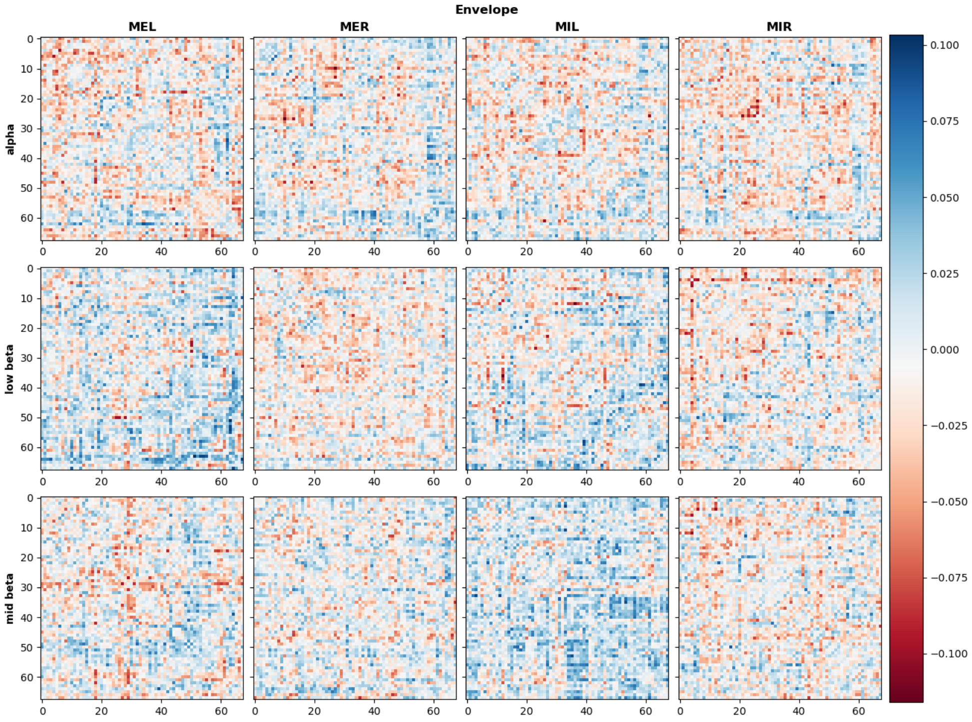

Figure A.7: Envelope FC difference between rest and other tasks.

A.2 Functional Connectivity Statistical Differences

Tables A.1 to A.9 show the highest statistically significant ($\alpha < 0.05$) differences for each FC metric and frequency band. Figure A.8 shows the box plots of all statistically significant ($\alpha < 0.05$) differences for each FC metric and frequency band.

Table A.1: COH alpha FC difference between tasks in all node connections. All FC diferences are statistically significant ($\alpha < 0.05$) and > 0.175.

			REST-MEL	MEL-MER	MEL-MIL	MEL-MIR	MER-MIL	MIL-MIR
metric	frequency	connection						
COH	alpha	lateralorbitofrontal-rh - parsorbitalis-rh				0.182		
		lateralorbitofrontal-rh - cuneus-rh					0.18	
		lateralorbitofrontal-rh - entorhinal-rh		0.186			-0.187	
		lateralorbitofrontal-rh - temporalpole-rh		0.187				
		parsorbitalis-rh - entorhinal-rh				0.201		0.194
		parsorbitalis-rh - temporalpole-lh				-0.184		
		parsorbitalis-rh - insula-lh				-0.191		
		parstriangularis-rh - temporalpole-rh		0.191			-0.175	
		parstriangularis-rh - superiortemporal-rh				0.198		
		rostralmiddlefrontal-rh - transversetemporal-lh		0.18				
		lateralorbitofrontal-lh - parsopercularis-lh				-0.176		
		parstriangularis-lh - supramarginal-lh			-0.204			
		precentral-lh - supramarginal-lh	-0.188					
		posteriorcingulate-lh - supramarginal-lh				0.203		
		posteriorcingulate-lh - superiorparietal-lh				0.233		
		supramarginal-lh - temporalpole-lh			-0.188			
		supramarginal-lh - transversetemporal-lh			-0.223	-0.209		
		supramarginal-lh - insula-lh			-0.183			
		lingual-lh - entorhinal-lh		-0.189				
		entorhinal-lh - superiortemporal-lh				-0.175		
		bankssts-lh - superiortemporal-lh		-0.188				
		bankssts-lh - transversetemporal-lh		-0.183				

Table A.2: COH low beta FC difference between tasks in all node connections. All FC diferences are statistically significant ($\alpha < 0.05$) and > 0.175.

			REST-MEL	MEL-MER	MEL-MIR	MIL-MIR
metric	frequency	connection				
COH	low beta	parsorbitalis-rh - entorhinal-rh			0.188	
		parsorbitalis-rh - temporalpole-rh		0.189	0.176	
		parsorbitalis-rh - insula-rh			0.214	
		rostralmiddlefrontal-rh - cuneus-lh				0.176
		precuneus-rh - cuneus-rh	0.176			
		temporalpole-rh - superiortemporal-rh		0.179	0.178	
		lateralorbitofrontal-lh - superiortemporal-lh			0.213	
		precentral-lh - paracentral-lh	-0.234	0.194		
		posteriorcingulate-lh - cuneus-lh				0.195
		posteriorcingulate-lh - pericalcarine-lh			0.197	0.213
		postcentral-lh - bankssts-lh		-0.181		
		fusiform-lh - inferiortemporal-lh			0.215	

Table A.3: COH mid beta FC difference between tasks in all node connections. All FC diferences are statistically significant ($\alpha < 0.05$) and > 0.175.

			REST-MEL	MEL-MER	MEL-MIL	MEL-MIR
metric	frequency	connection				
COH	mid beta	lateralorbitofrontal-rh - parsorbitalis-rh				0.183
		lateralorbitofrontal-rh - temporalpole-rh		0.183		
		parsorbitalis-rh - frontalpole-rh				0.186
		parsorbitalis-rh - temporalpole-rh	-0.199	0.237	0.182	0.228
		parsorbitalis-rh - insula-rh				0.187
		parstriangularis-rh - temporalpole-rh		0.188		
		paracentral-rh - precentral-lh	-0.189	0.193		
		posteriorcingulate-rh - precentral-lh	-0.179	0.198		
		precentral-lh - paracentral-lh	-0.196	0.189		

Table A.4: PLV alpha FC difference between tasks in all node connections. All FC diferences are statistically significant ($\alpha < 0.05$) and > 0.2.

			REST-MIL	MEL-MER	MEL-MIL	MEL-MIR	MER-MIL	MIL-MIR
metric	frequency	connection						
PLV	alpha	parsorbitalis-rh - parstriangularis-rh				0.202		
		medialorbitofrontal-rh - middletemporal-rh						0.203
		parsopercularis-rh - lateralorbitofrontal-lh					0.235	
		parsopercularis-rh - parsorbitalis-lh					0.225	
		parsopercularis-rh - frontalpole-lh					0.219	
		superiorfrontal-rh - fusiform-lh			-0.206			
		rostralanteriorcingulate-rh - inferiortemporal-lh					-0.202	
		posteriorcingulate-rh - precentral-lh						0.2
		posteriorcingulate-rh - inferiortemporal-lh		0.235				
		isthmuscingulate-rh - inferiorparietal-rh			-0.222			0.208
		inferiorparietal-rh - precuneus-rh			-0.282			
		inferiorparietal-rh - pericalcarine-rh		0.233	0.21			
		inferiorparietal-rh - lingual-rh						-0.202
		inferiorparietal-rh - isthmuscingulate-lh			-0.205			
		inferiorparietal-rh - transversetemporal-lh	-0.21					
		parahippocampal-rh - bankssts-rh					-0.208	0.218
		parahippocampal-rh - transversetemporal-lh						0.214
		temporalpole-rh - caudalmiddlefrontal-lh						0.204
		temporalpole-rh - transversetemporal-lh						0.204
		middletemporal-rh - medialorbitofrontal-lh						0.264
		superiortemporal-rh - transversetemporal-rh						0.207
		insula-rh - transversetemporal-lh					-0.218	0.221
		frontalpole-lh - precentral-lh	-0.208				-0.2	0.223
		medialorbitofrontal-lh - postcentral-lh					-0.203	
		parstriangularis-lh - precentral-lh	-0.206					
		superiorfrontal-lh - precentral-lh		0.21			-0.2	
		precentral-lh - superiorparietal-lh				0.213		0.21
		precentral-lh - inferiorparietal-lh						0.222
		precentral-lh - precuneus-lh						0.207
		pericalcarine-lh - transversetemporal-lh		-0.213				
		lingual-lh - transversetemporal-lh		-0.22				
		fusiform-lh - transversetemporal-lh		-0.237				

Table A.5: PLV low beta FC difference between tasks in all node connections. All FC diferences are statistically significant ($\alpha < 0.05$) and > 0.2.

metric	frequency	connection	MEL-MER	MEL-MIL	MEL-MIR	MER-MIL	MIL-MIR
PLV	low beta	parsorbitalis-rh - rostralmiddlefrontal-rh					0.201
		parsorbitalis-rh - entorhinal-rh					0.225
		parstriangularis-rh - superiortemporal-lh			0.248		
		rostralmiddlefrontal-rh - superiorparietal-rh			0.202		
		paracentral-rh - parahippocampal-lh		0.216			
		paracentral-rh - inferiortemporal-lh		0.227			
		caudalanteriorcingulate-rh - precuneus-rh			0.211		
		caudalanteriorcingulate-rh - transversetemporal-lh				0.202	
		precuneus-rh - caudalanteriorcingulate-lh			0.205		
		temporalpole-rh - transversetemporal-lh					0.201
		superiortemporal-rh - transversetemporal-rh			0.212		
		parstriangularis-lh - precentral-lh	0.237				
		paracentral-lh - fusiform-lh		0.213			
		posteriorcingulate-lh - inferiortemporal-lh		0.21			

Table A.6: PLV mid beta FC difference between tasks in all node connections. All FC diferences are statistically significant ($\alpha < 0.05$) and > 0.2.

metric	frequency	connection	REST-MEL	MEL-MER	MEL-MIL	MEL-MIR	MER-MIL	MER-MIR	MIL-MIR
PLV	mid beta	parsorbitalis-rh - parstriangularis-rh							0.22
		parsorbitalis-rh - insula-rh						0.216	
		parstriangularis-rh - superiortemporal-lh							0.225
		superiorfrontal-rh - supramarginal-lh		0.225					
		superiorfrontal-rh - lingual-lh				0.209			
		paracentral-rh - entorhinal-rh						0.228	
		isthmuscingulate-rh - caudalanteriorcingulate-lh					-0.2		
		superiorparietal-rh - parsorbitalis-lh			-0.222				
		entorhinal-rh - paracentral-lh						0.208	
		entorhinal-rh - precuneus-lh						0.234	
		temporalpole-rh - caudalmiddlefrontal-lh			-0.216				
		temporalpole-rh - transversetemporal-lh			-0.216				
		insula-rh - transversetemporal-lh							0.222
		parsorbitalis-lh - lateraloccipital-lh	-0.204			0.232			
		parstriangularis-lh - precentral-lh		0.227			-0.209		
		parsopercularis-lh - inferiortemporal-lh		-0.23					
		postcentral-lh - bankssts-lh							-0.202
		temporalpole-lh - transversetemporal-lh			-0.219				

Table A.7: Envelope alpha FC difference between tasks in all node connections. All FC diferences are statistically significant ($\alpha < 0.05$) and > 0.12.

metric	frequency	connection	MEL-MER	MEL-MIL	MEL-MIR	MER-MIL	MER-MIR	MIL-MIR
Envelope	alpha	rostralmiddlefrontal-rh - superiorfrontal-rh	-0.121			0.14		
		superiorfrontal-rh - rostralmiddlefrontal-lh						-0.12
		postcentral-rh - superiorparietal-lh						-0.133
		precuneus-rh - isthmuscingulate-lh				-0.124		
		cuneus-rh - precentral-lh					-0.133	
		lateraloccipital-rh - pericalcarine-lh						0.127
		lingual-rh - fusiform-rh			0.13			
		superiortemporal-rh - parsopercularis-lh		0.126				
		lingual-lh - transversetemporal-lh	-0.137					
		fusiform-lh - transversetemporal-lh	-0.136					

Table A.8: Envelope low beta FC difference between tasks in all node connections. All FC diferences are statistically significant ($\alpha < 0.05$) and > 0.12.

			MEL-MER	MEL-MIL	MEL-MIR	MIL-MIR
metric	frequency	connection				
Envelope	low beta	precentral-rh - isthmuscingulate-lh		0.121		
		posteriorcingulate-rh - precuneus-rh	0.137			
		postcentral-rh - supramarginal-lh				-0.138
		medialorbitofrontal-lh - insula-lh				0.121
		caudalanteriorcingulate-lh - superiortemporal-lh		0.128		
		superiorparietal-lh - middletemporal-lh	0.144			
		precuneus-lh - fusiform-lh	0.132			
		precuneus-lh - middletemporal-lh	0.146			
		cuneus-lh - middletemporal-lh	0.12		0.124	
		pericalcarine-lh - middletemporal-lh	0.132		0.144	

Table A.9: Envelope mid beta FC difference between tasks in all node connections. All FC diferences are statistically significant ($\alpha < 0.05$) and > 0.12.

			MEL-MIL	MEL-MIR	MER-MIL	MIL-MIR
metric	frequency	connection				
Envelope	mid beta	medialorbitofrontal-rh - insula-rh				0.131
		parstriangularis-rh - rostralmiddlefrontal-rh				0.129
		parstriangularis-rh - rostralanteriorcingulate-rh				0.122
		parstriangularis-rh - caudalanteriorcingulate-rh				0.122
		parstriangularis-rh - lateraloccipital-lh			-0.127	
		posteriorcingulate-rh - caudalanteriorcingulate-lh			-0.123	
		supramarginal-rh - superiorparietal-rh	-0.123			
		bankssts-rh - superiorparietal-lh		0.121		
		superiortemporal-rh - lateralorbitofrontal-lh	-0.131			
		parsorbitalis-lh - insula-lh			-0.131	
		medialorbitofrontal-lh - insula-lh				0.137
		cuneus-lh - temporalpole-lh	-0.12			

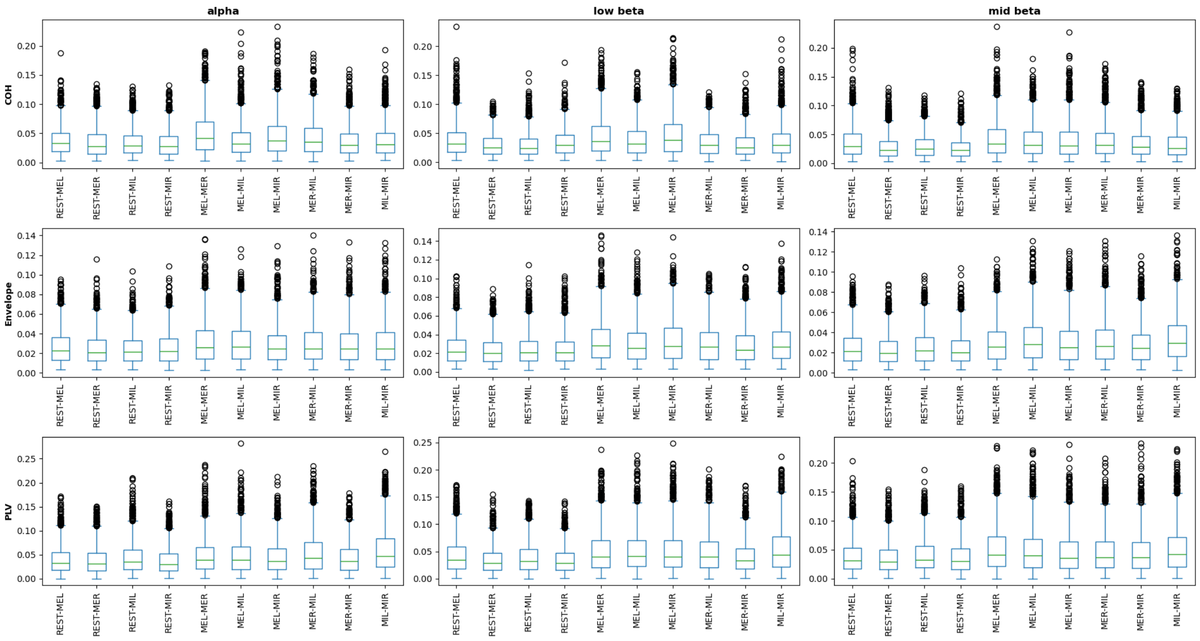

Figure A.8: Box plots of absolute significant differences for all task comparisons frequency bands and FC metrics

A.3 Metastability and Coherence

Figures A.9 and A.10 show the distribution of the empirical metastability and coherence for each task.

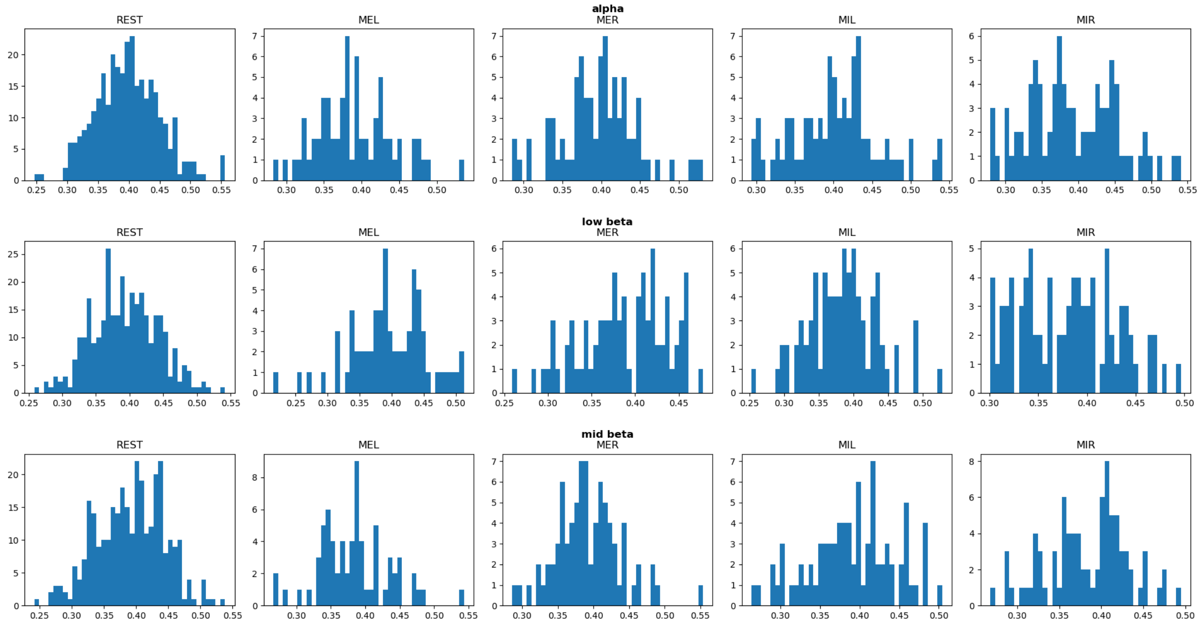

Figure A.9: Coherence distribution for all events and frequency bands

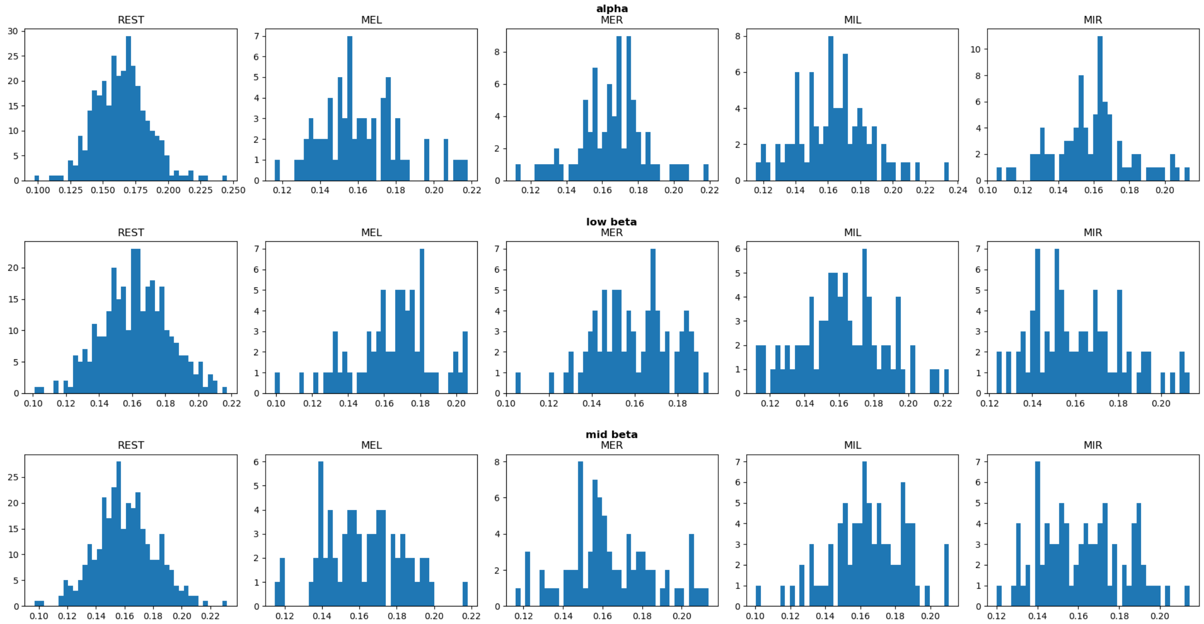

Figure A.10: Metastability distribution for all events and frequency bands

Appendix B

Simulation data

B.1 Structural Connectivity Parameter exploration

Figures B.1 to B.9 show the exploration of the *G* parameter across FC metrics, SC metrics, frequency bands. Figures B.10 to B.18 show the exploration of the *a* parameter across FC metrics, SC metrics, frequency bands.

B.1.1 *G* parameter

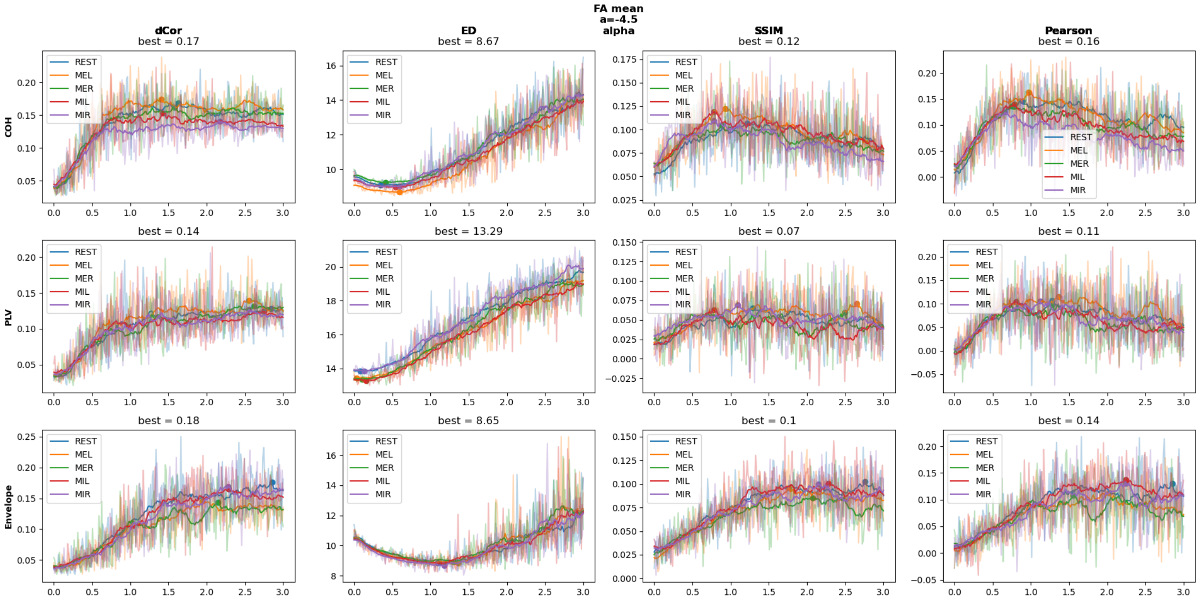

Figure B.1: *G* parameter exploration using FA mean as the adjacency connectivity matrix, *C*, for every task at the alpha frequency and the respective supercritical bifurcation parameter. Each color corresponds to a different task's fit with a moving average filter and a dot on the best fit point. The actual fits are the shaded profiles.

B. SIMULATION DATA

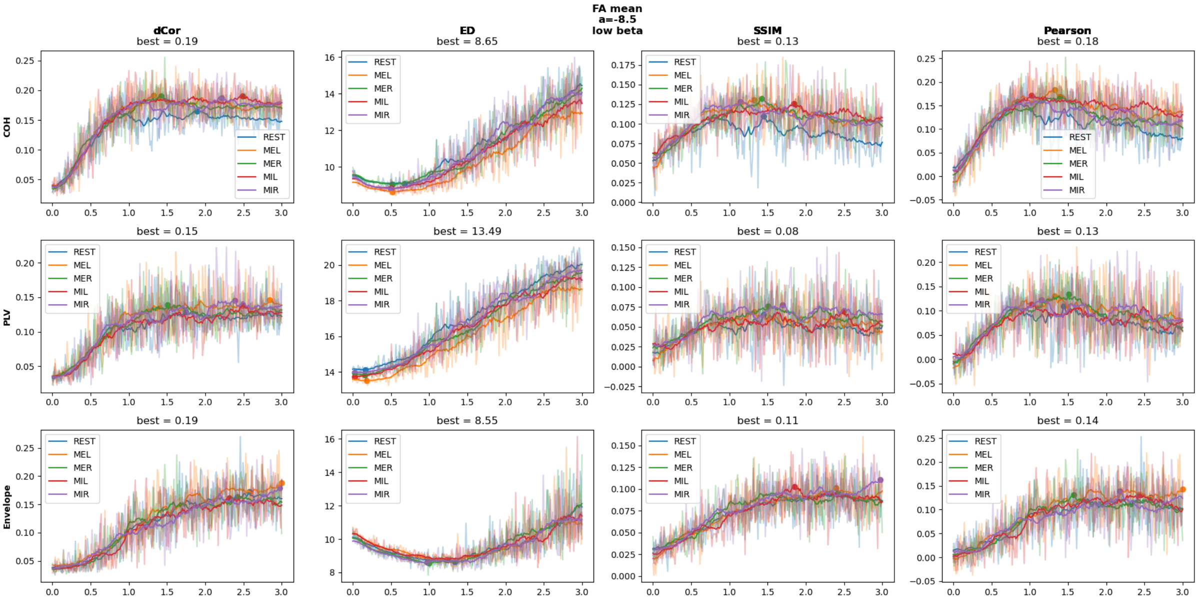

Figure B.2: *G* parameter exploration using FA mean as the adjacency connectivity matrix, *C*, for every task at the low beta frequency and the respective supercritical bifurcation parameter. Each color corresponds to a different task's fit with a moving average filter and a dot on the best fit point. The actual fits are the shaded profiles.

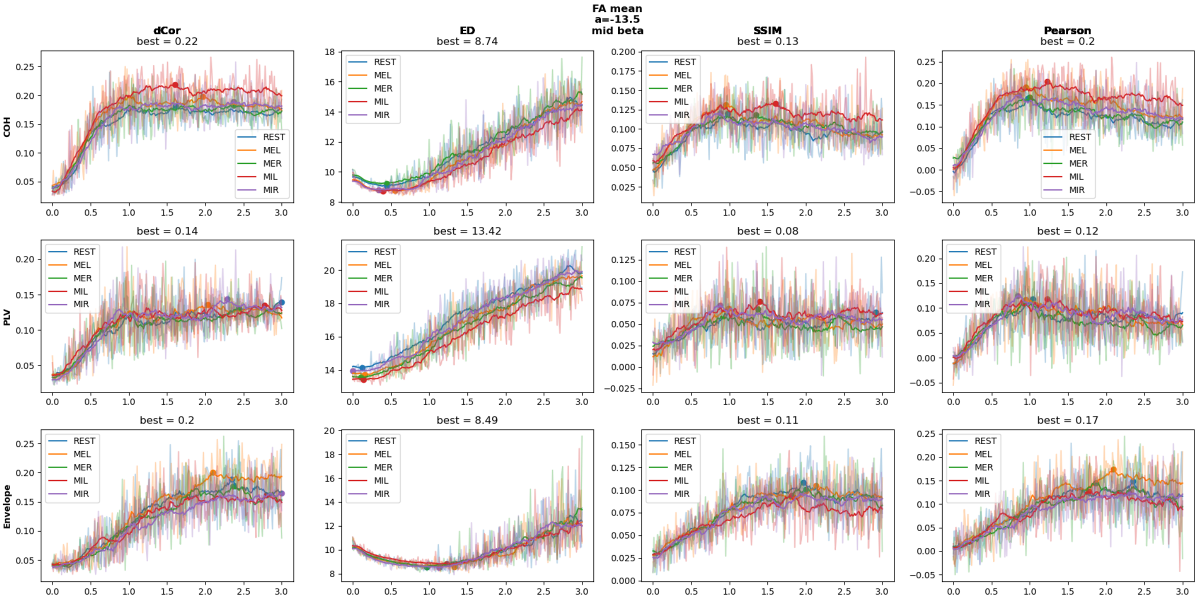

Figure B.3: *G* parameter exploration using FA mean as the adjacency connectivity matrix, *C*, for every task at the mid beta frequency and the respective supercritical bifurcation parameter. Each color corresponds to a different task's fit with a moving average filter and a dot on the best fit point. The actual fits are the shaded profiles.

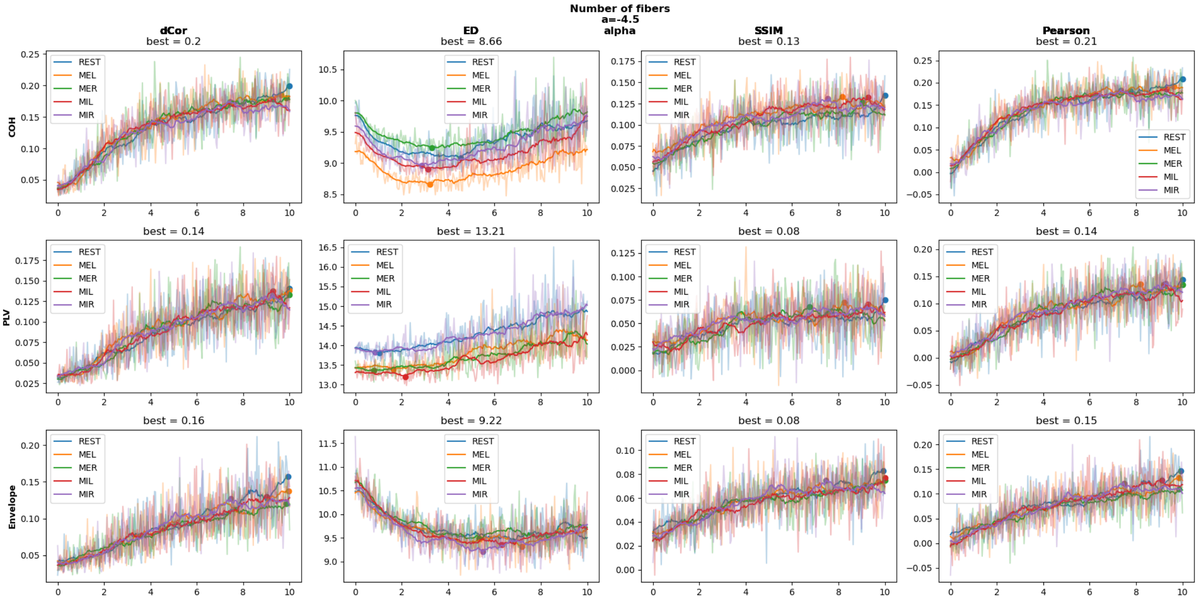

Figure B.4: *G* parameter exploration using Number of fibers as the adjacency connectivity matrix, *C*, for every task at the alpha frequency and the respective supercritical bifurcation parameter. Each color corresponds to a different task's fit with a moving average filter and a dot on the best fit point. The actual fits are the shaded profiles.

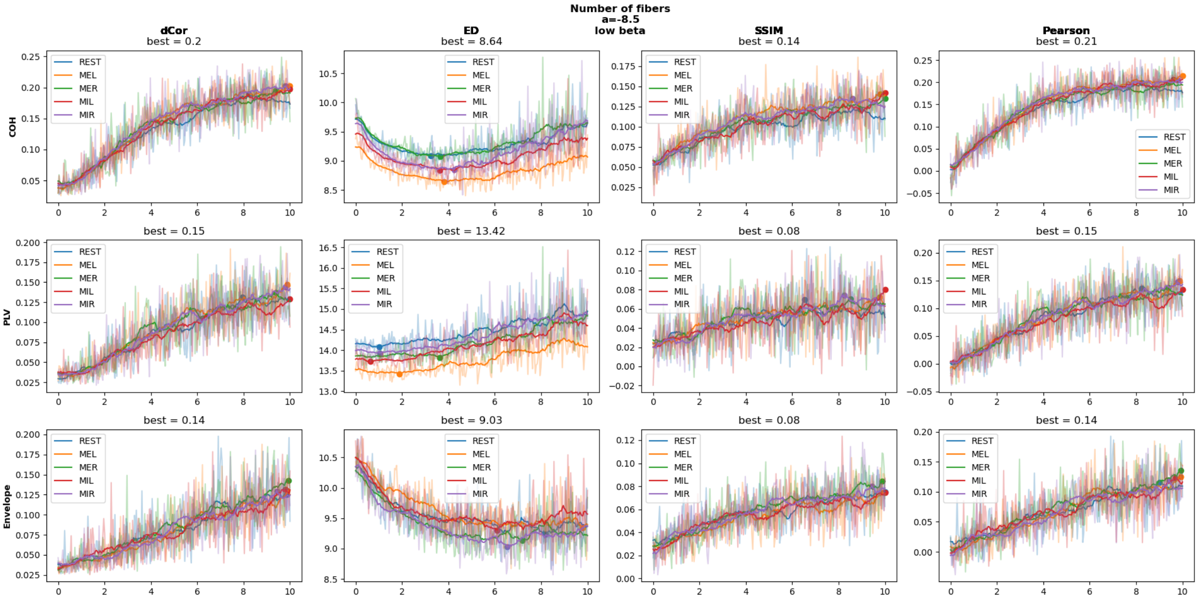

Figure B.5: *G* parameter exploration using Number of fibers as the adjacency connectivity matrix, *C*, for every task at the low beta frequency and the respective supercritical bifurcation parameter. Each color corresponds to a different task's fit with a moving average filter and a dot on the best fit point. The actual fits are the shaded profiles.

B. SIMULATION DATA

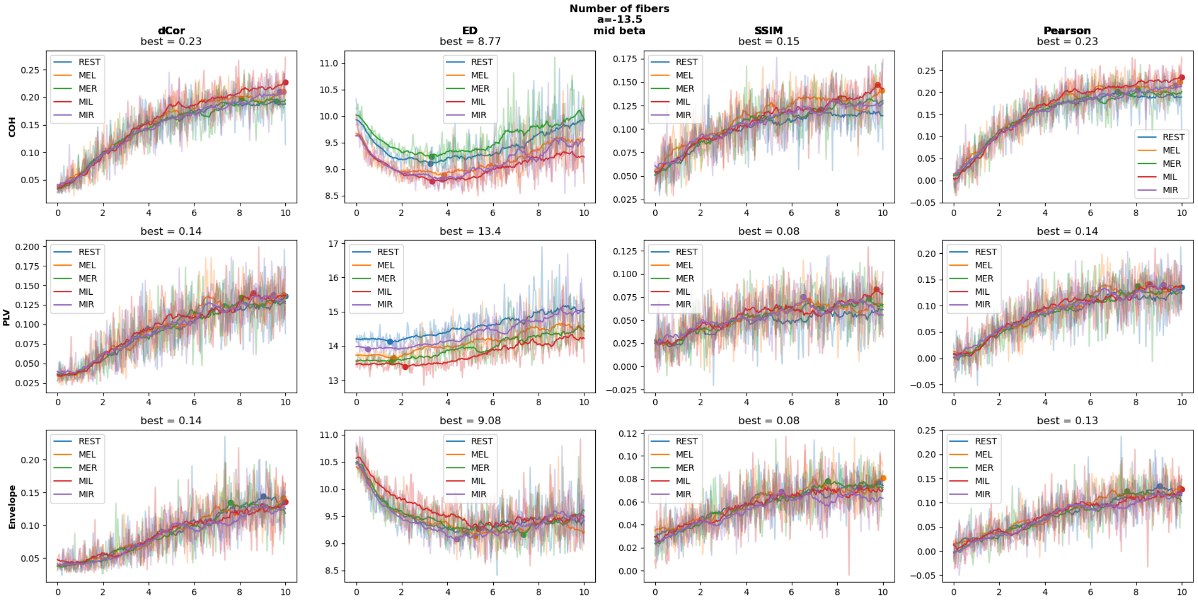

Figure B.6: *G* parameter exploration using Number of fibers as the adjacency connectivity matrix, *C*, for every task at the mid beta frequency and the respective supercritical bifurcation parameter. Each color corresponds to a different task's fit with a moving average filter and a dot on the best fit point. The actual fits are the shaded profiles.

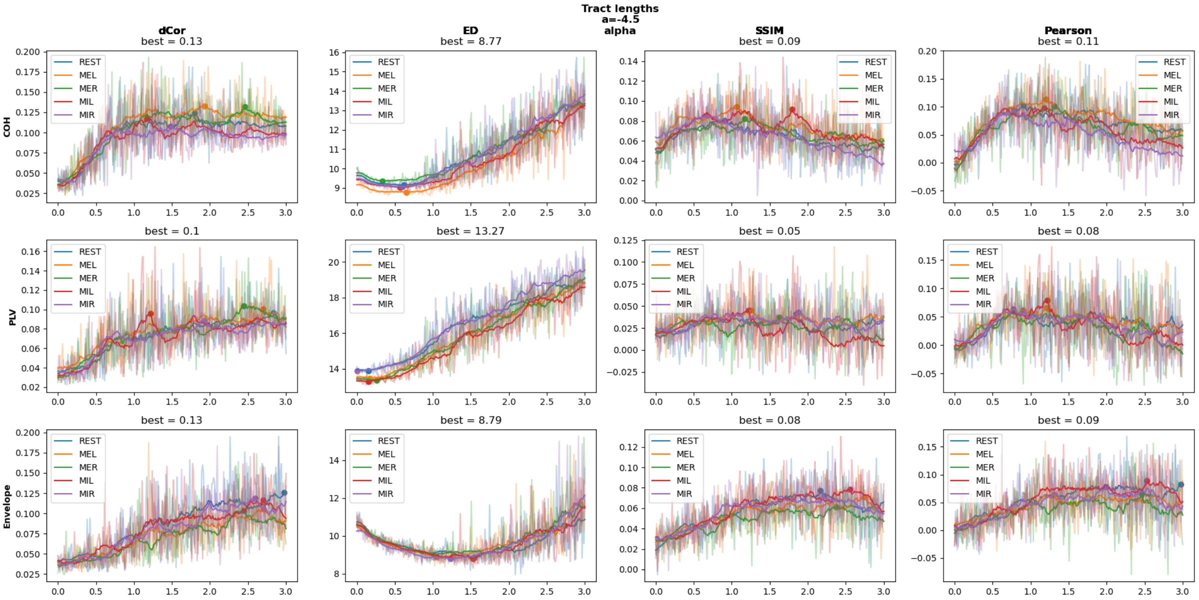

Figure B.7: *G* parameter exploration using Tract lengths as the adjacency connectivity matrix, *C*, for every task at the alpha frequency and the respective supercritical bifurcation parameter. Each color corresponds to a different task's fit with a moving average filter and a dot on the best fit point. The actual fits are the shaded profiles.

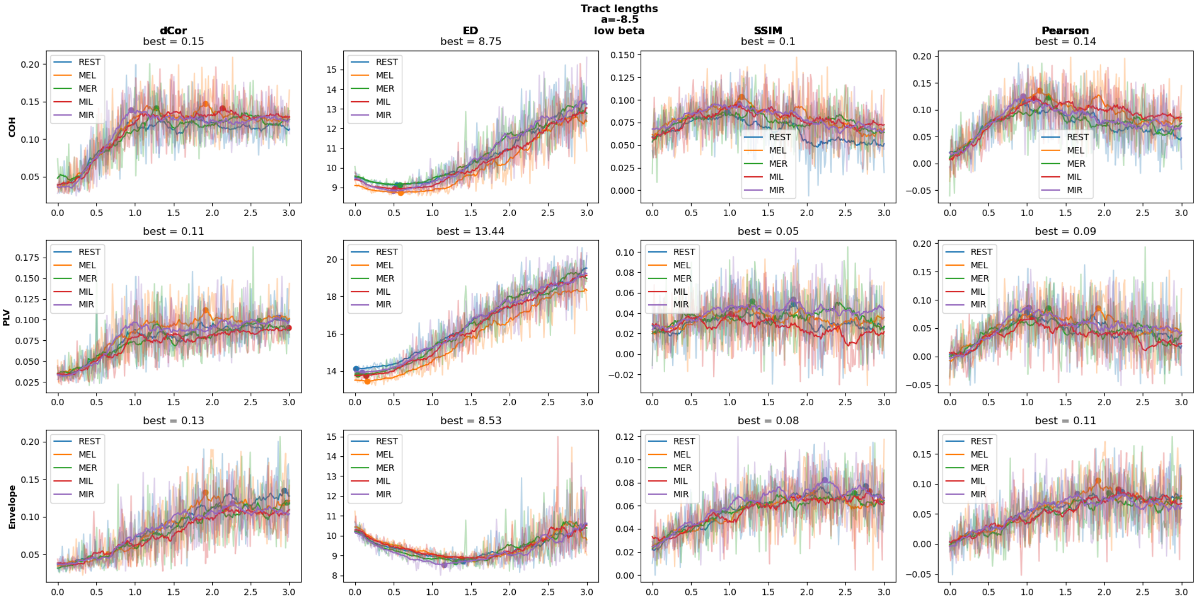

Figure B.8: *G* parameter exploration using Tract lengths as the adjacency connectivity matrix, *C*, for every task at the low beta frequency and the respective supercritical bifurcation parameter. Each color corresponds to a different task's fit with a moving average filter and a dot on the best fit point. The actual fits are the shaded profiles.

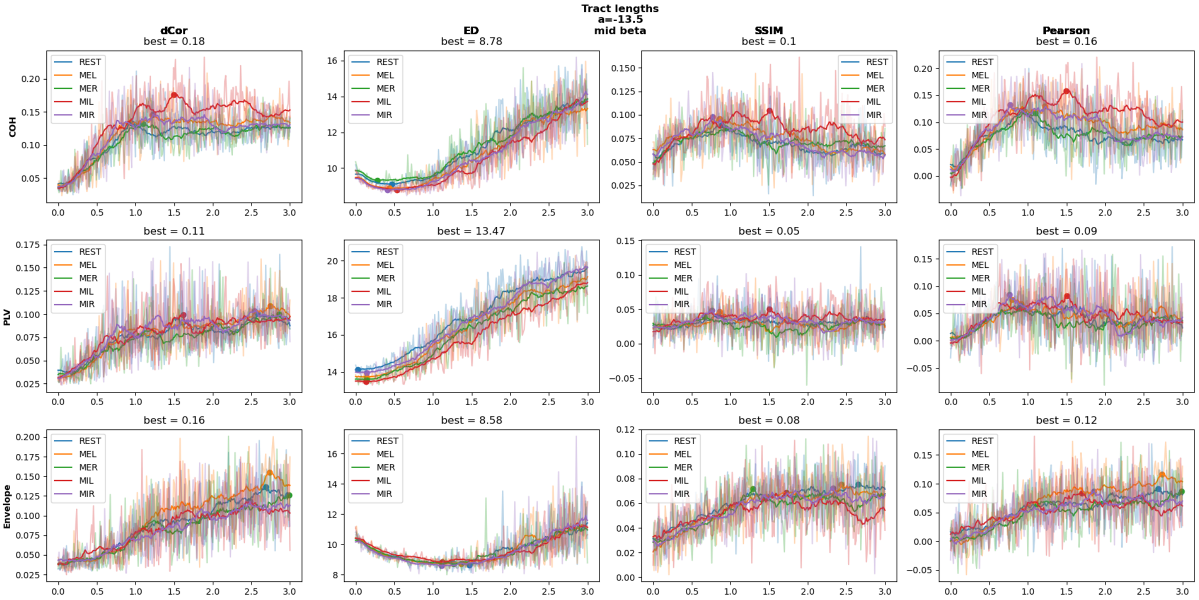

Figure B.9: *G* parameter exploration using Tract lengths as the adjacency connectivity matrix, *C*, for every task at the mid beta frequency and the respective supercritical bifurcation parameter. Each color corresponds to a different task's fit with a moving average filter and a dot on the best fit point. The actual fits are the shaded profiles.

B.1.2 *a* parameter

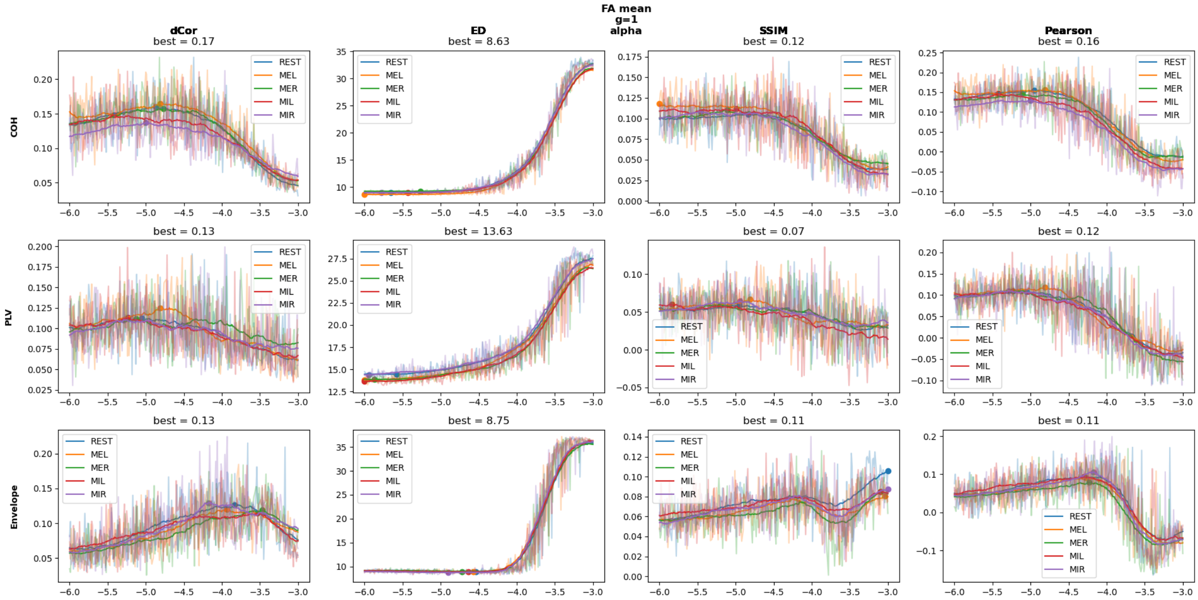

Figure B.10: *a* parameter exploration using FA mean as the adjacency connectivity matrix, *C*, for every task at the alpha frequency. The *g* parameter was chosen for each structural connectivity based on the previous *g* parameter exploration. Each color corresponds to a different task's fit with a moving average filter and a dot on the best fit point. The actual fits are the shaded profiles.

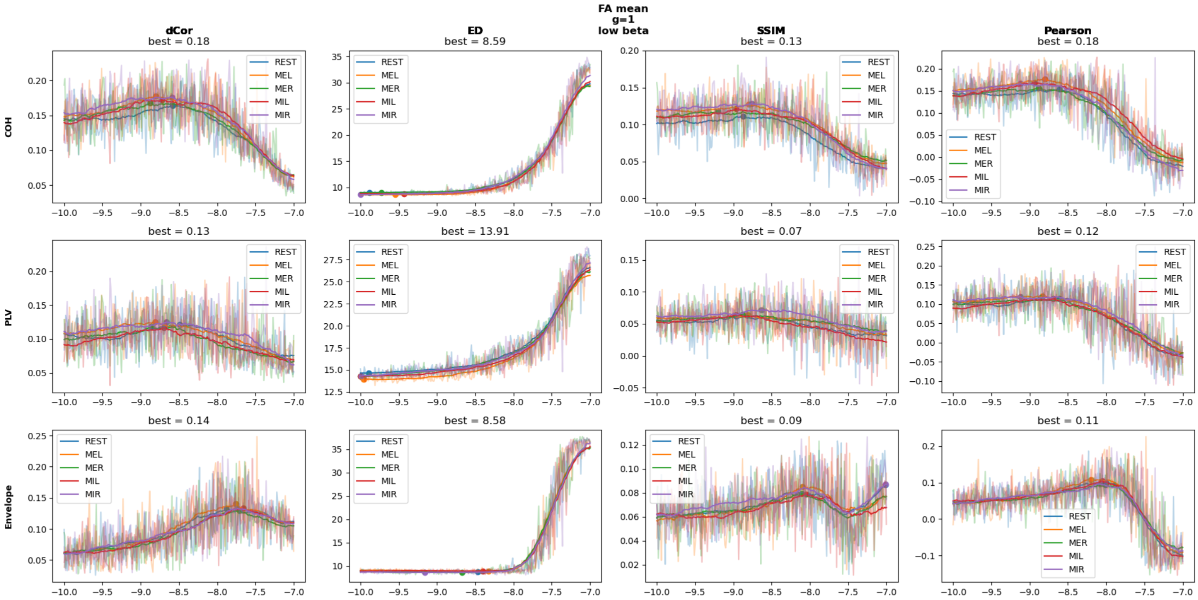

Figure B.11: *a* parameter exploration using FA mean as the adjacency connectivity matrix, *C*, for every task at the low beta frequency. The *g* parameter was chosen for each structural connectivity based on the previous *g* parameter exploration. Each color corresponds to a different task's fit with a moving average filter and a dot on the best fit point. The actual fits are the shaded profiles.

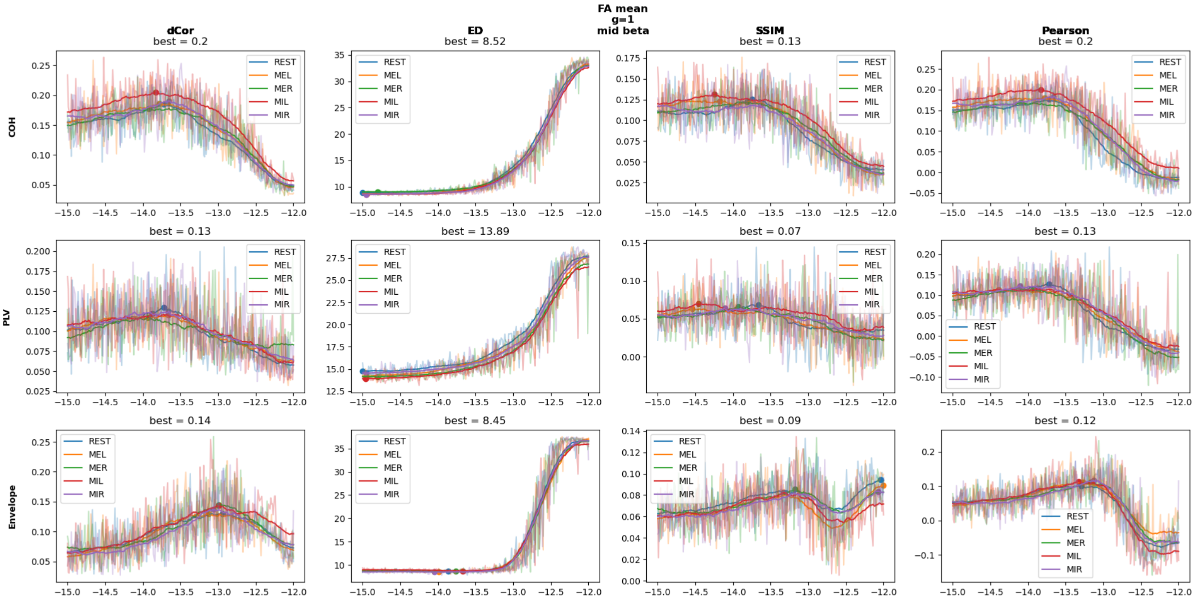

Figure B.12: *a* parameter exploration using FA mean as the adjacency connectivity matrix, *C*, for every task at the mid beta frequency. The *g* parameter was chosen for each structural connectivity based on the previous *g* parameter exploration. Each color corresponds to a different task's fit with a moving average filter and a dot on the best fit point. The actual fits are the shaded profiles.

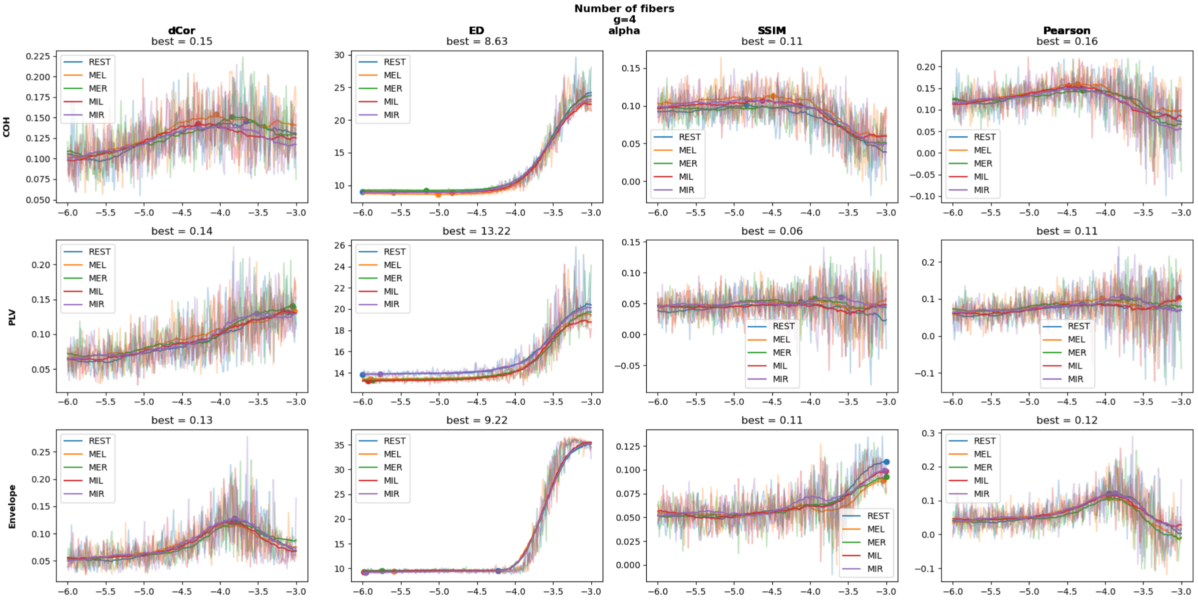

Figure B.13: *a* parameter exploration using Number of fibers as the adjacency connectivity matrix, *C*, for every task at the alpha frequency. The *g* parameter was chosen for each structural connectivity based on the previous *g* parameter exploration. Each color corresponds to a different task's fit with a moving average filter and a dot on the best fit point. The actual fits are the shaded profiles.

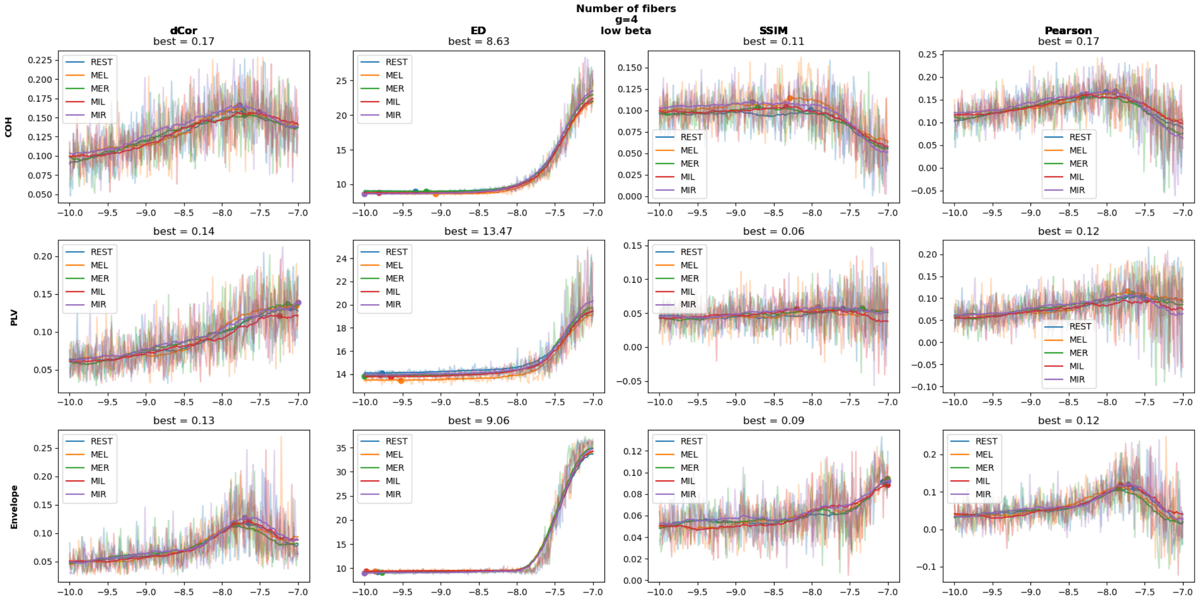

Figure B.14: *a* parameter exploration using Number of fibers as the adjacency connectivity matrix, *C*, for every task at the low beta frequency. The *g* parameter was chosen for each structural connectivity based on the previous *g* parameter exploration. Each color corresponds to a different task's fit with a moving average filter and a dot on the best fit point. The actual fits are the shaded profiles.

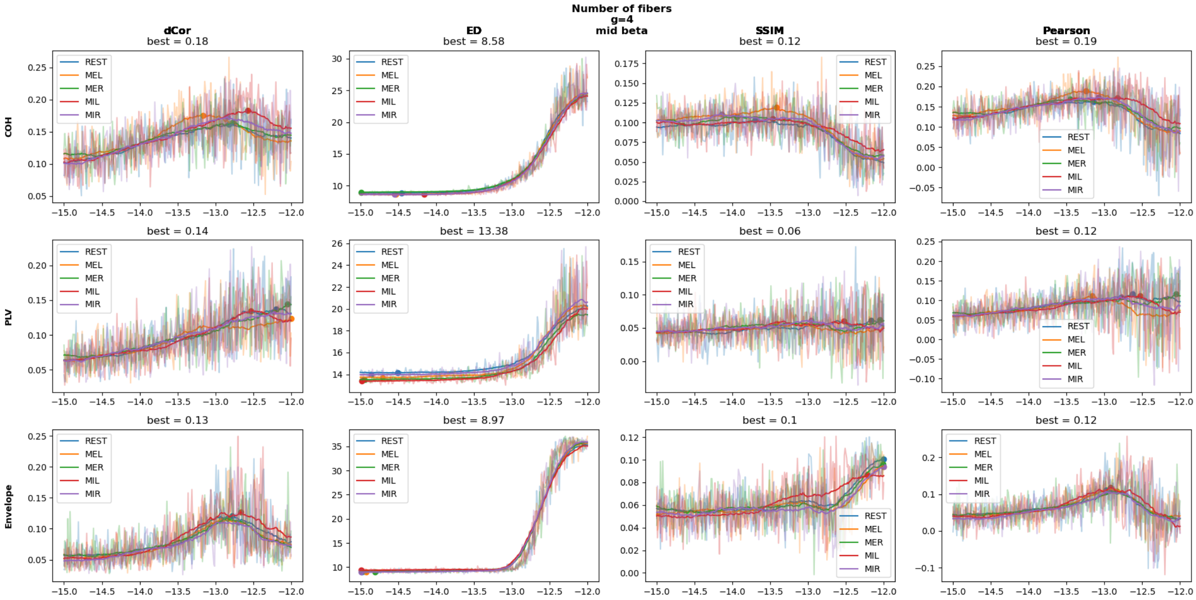

Figure B.15: *a* parameter exploration using Number of fibers as the adjacency connectivity matrix, *C*, for every task at the mid beta frequency. The *g* parameter was chosen for each structural connectivity based on the previous *g* parameter exploration. Each color corresponds to a different task's fit with a moving average filter and a dot on the best fit point. The actual fits are the shaded profiles.

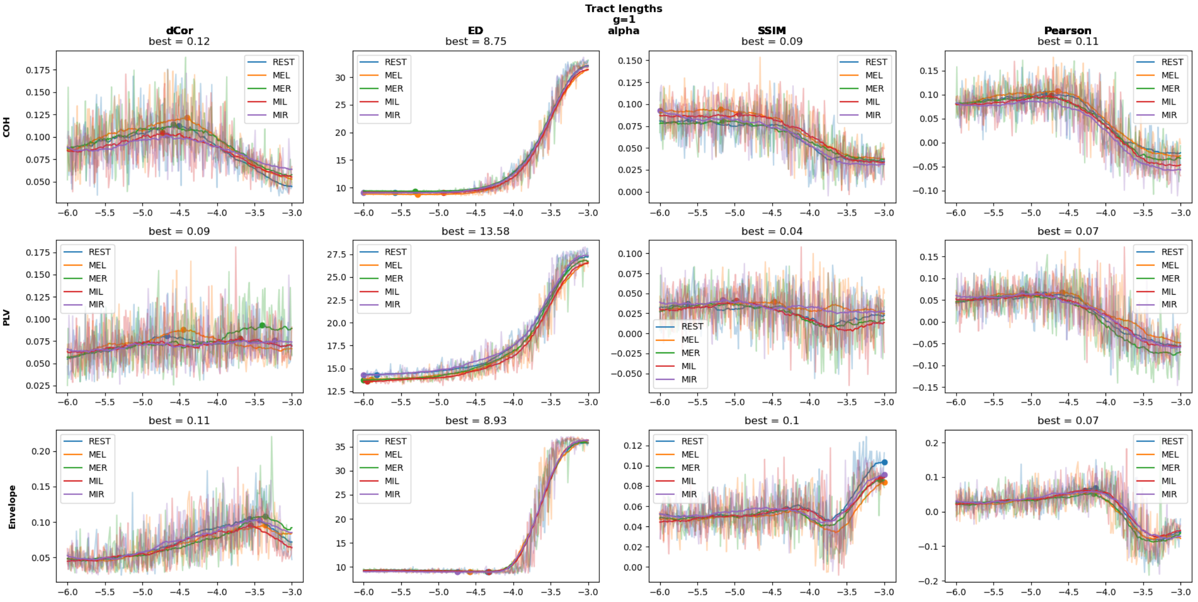

Figure B.16: *a* parameter exploration using Tract lengths as the adjacency connectivity matrix, *C*, for every task at the alpha frequency. The *g* parameter was chosen for each structural connectivity based on the previous *g* parameter exploration. Each color corresponds to a different task's fit with a moving average filter and a dot on the best fit point. The actual fits are the shaded profiles.

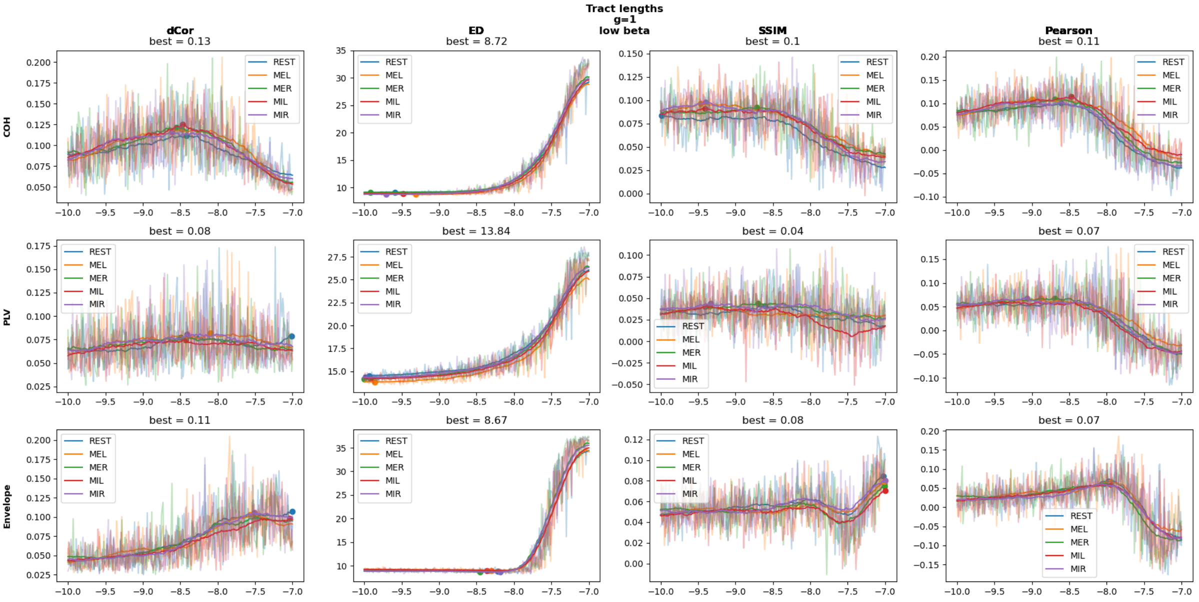

Figure B.17: *a* parameter exploration using Tract lengths as the adjacency connectivity matrix, *C*, for every task at the low beta frequency. The *g* parameter was chosen for each structural connectivity based on the previous *g* parameter exploration. Each color corresponds to a different task's fit with a moving average filter and a dot on the best fit point. The actual fits are the shaded profiles.

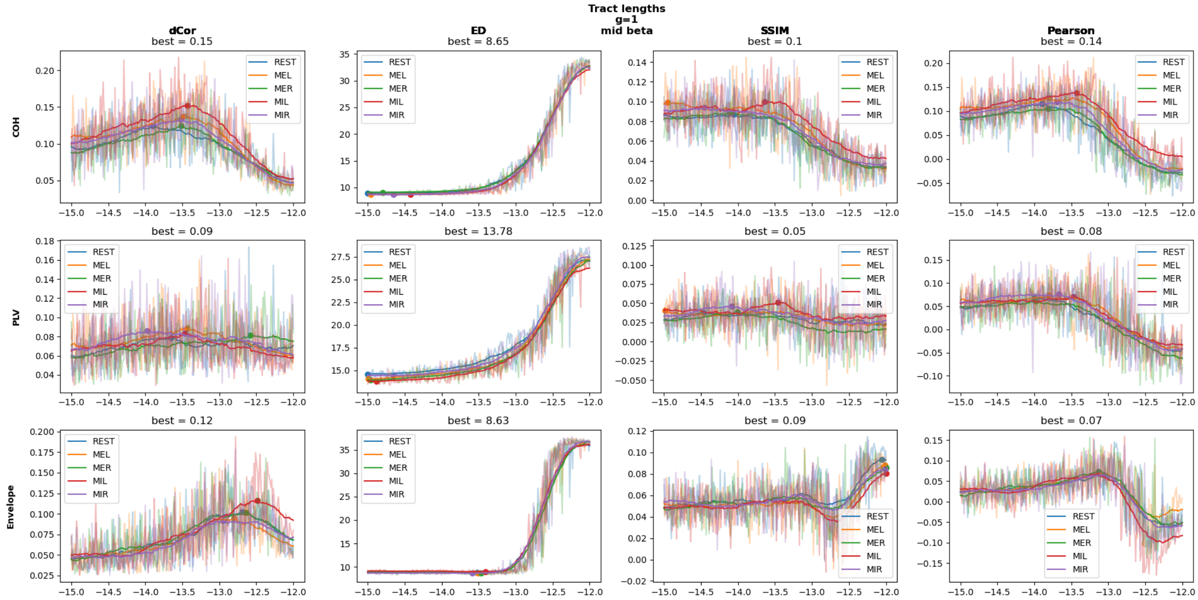

Figure B.18: *a* parameter exploration using Tract lengths as the adjacency connectivity matrix, *C*, for every task at the mid beta frequency. The *g* parameter was chosen for each structural connectivity based on the previous *g* parameter exploration. Each color corresponds to a different task's fit with a moving average filter and a dot on the best fit point. The actual fits are the shaded profiles.

B.2 Effective Connectivity fit

Figures B.19 to B.21 show the EC fitting for each FC metric and frequency, using the FA mean SC metric. Figures B.22 to B.27 show the final EC for each FC metric and frequency band as well as the differences in each EC between REST and other tasks.

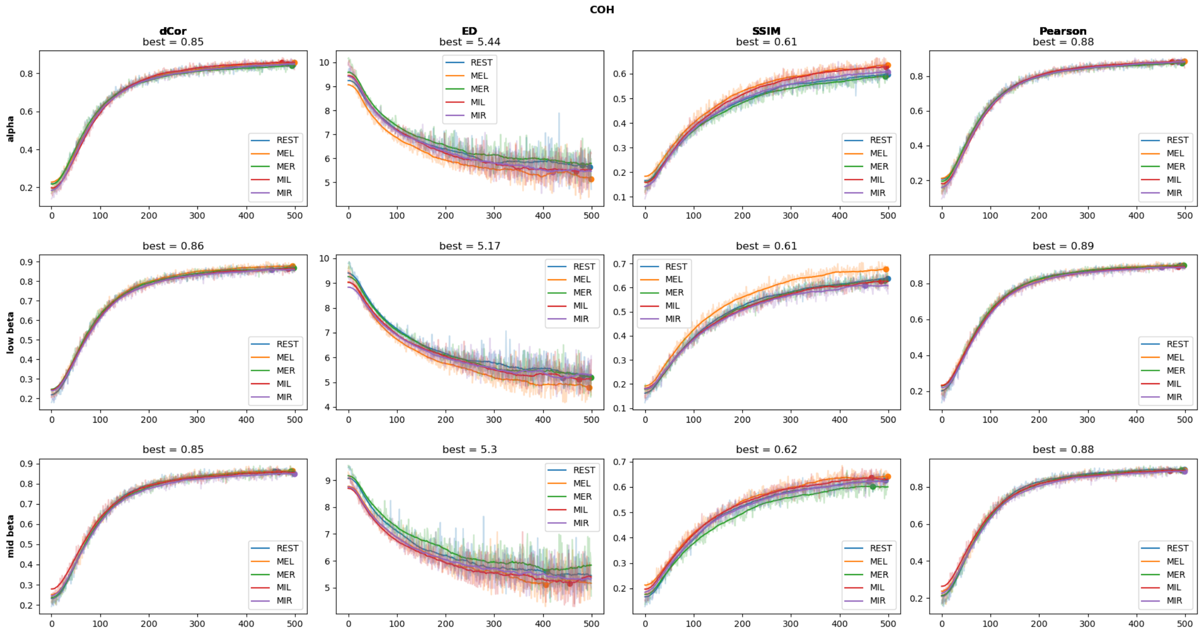

Figure B.19: EC fit for each task type and frequency at respective supercritical bifurcation parameter and $G = 1$ using the COH FC. Each color corresponds to a fit with a different task type with a moving average filter. The actual fit is displayed in a less opaque color.

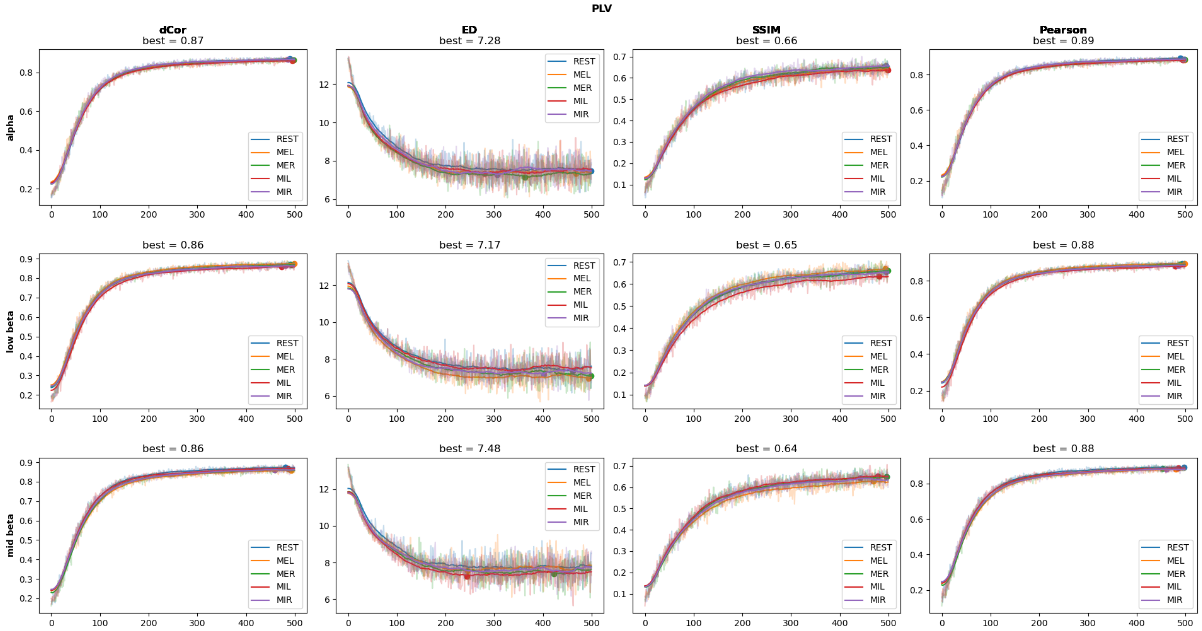

Figure B.20: EC fit for each task type and frequency at respective supercritical bifurcation parameter and $G = 1$ using the PLV FC. Each color corresponds to a fit with a different task type with a moving average filter. The actual fit is displayed in a less opaque color.

B. SIMULATION DATA

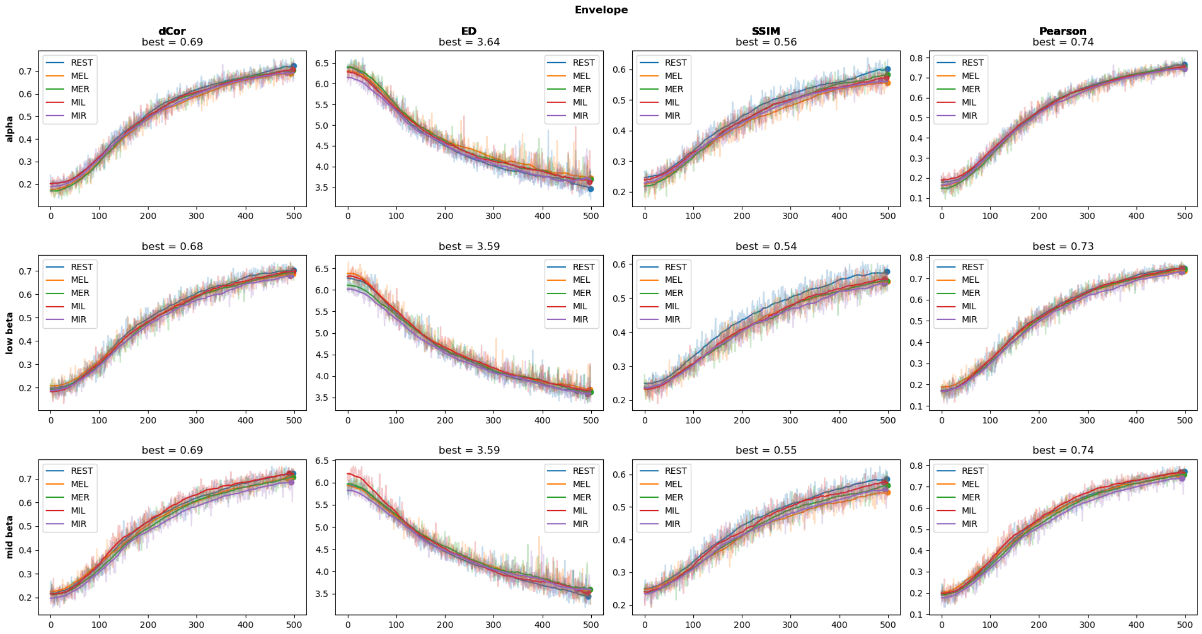

Figure B.21: EC fit for each task type and frequency at respective supercritical bifurcation parameter and $G = 1$ using the Envelope FC. Each color corresponds to a fit with a different task type with a moving average filter. The actual fit is displayed in a less opaque color.

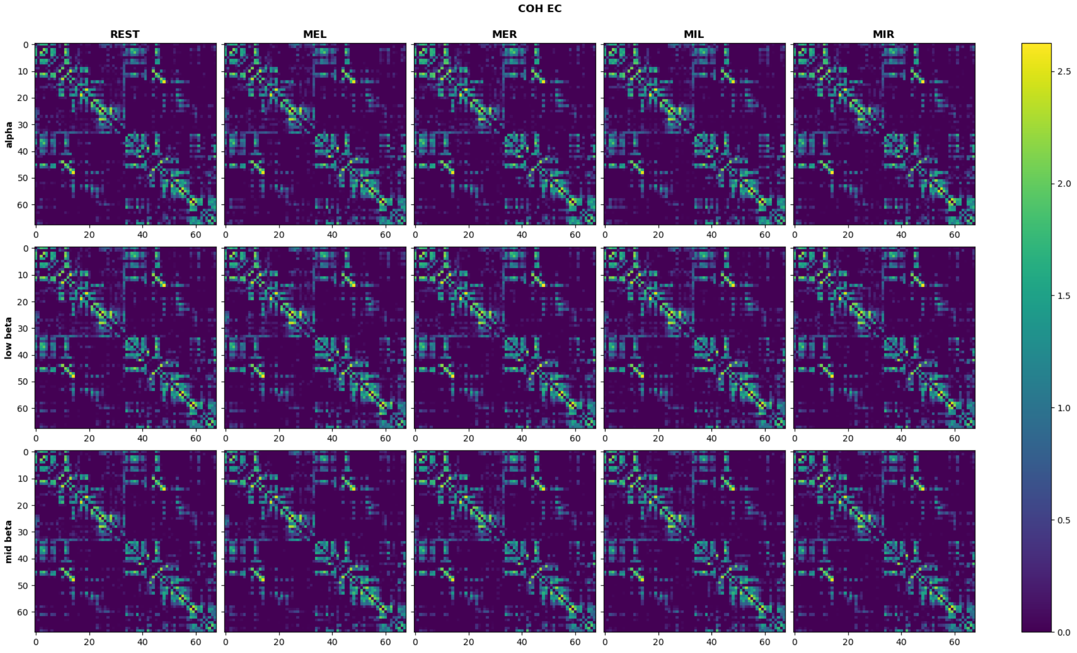

Figure B.22: EC matrix for each for each frequency and task type using the COH FC

Figure B.23: Differences between REST EC matrix and every other tasktype for each frequency, EC fitted using the COH FC.

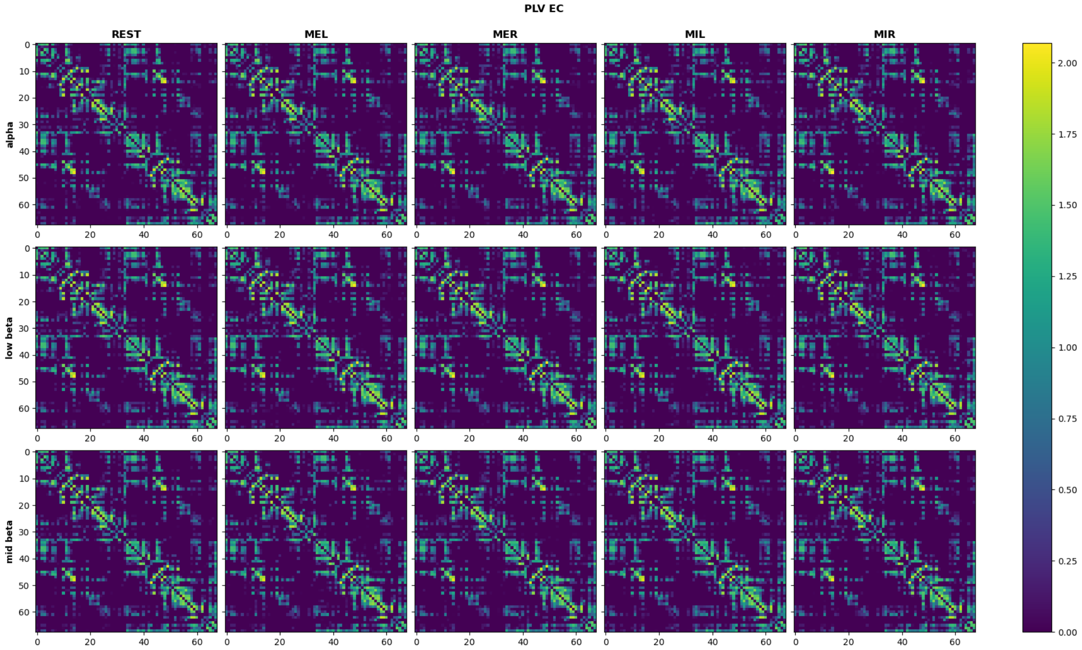

Figure B.24: EC matrix for each for each frequency and task type using the PLV FC

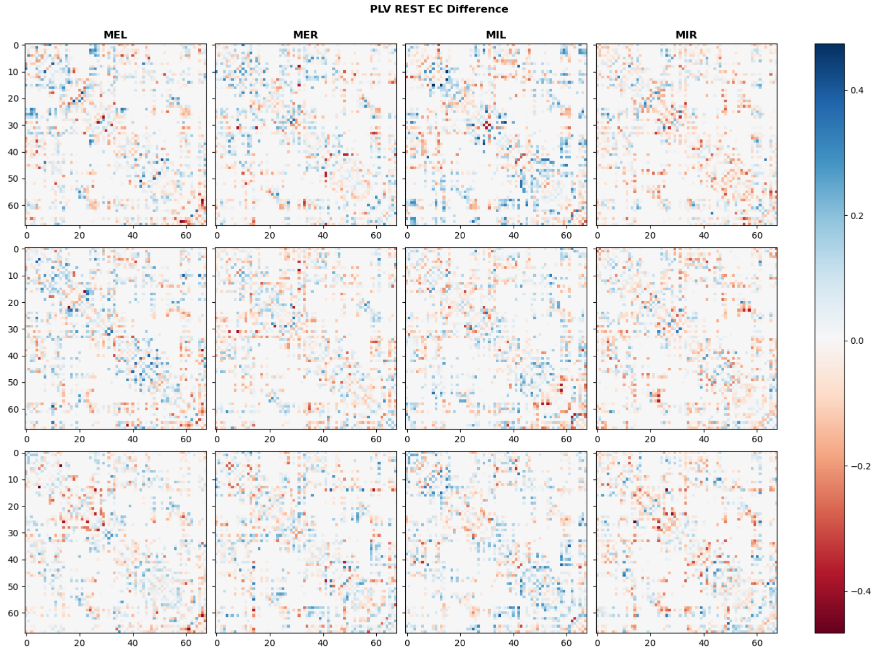

Figure B.25: Differences between REST EC matrix and every other tasktype for each frequency, EC fitted using the PLV FC.

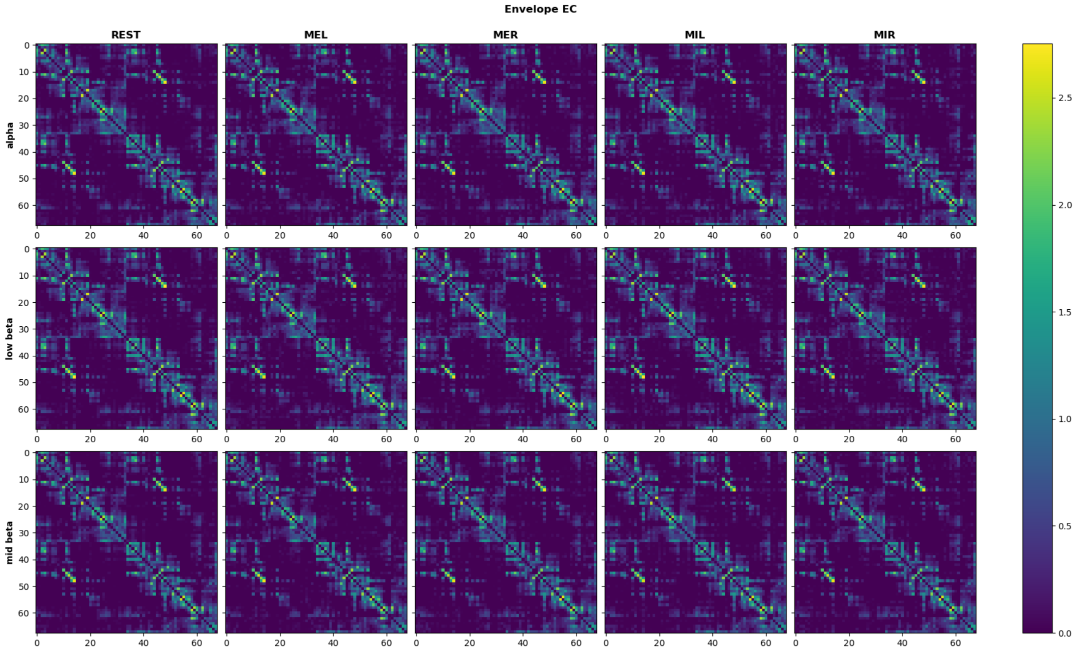

Figure B.26: EC matrix for each for each frequency and task type using the Envelope FC

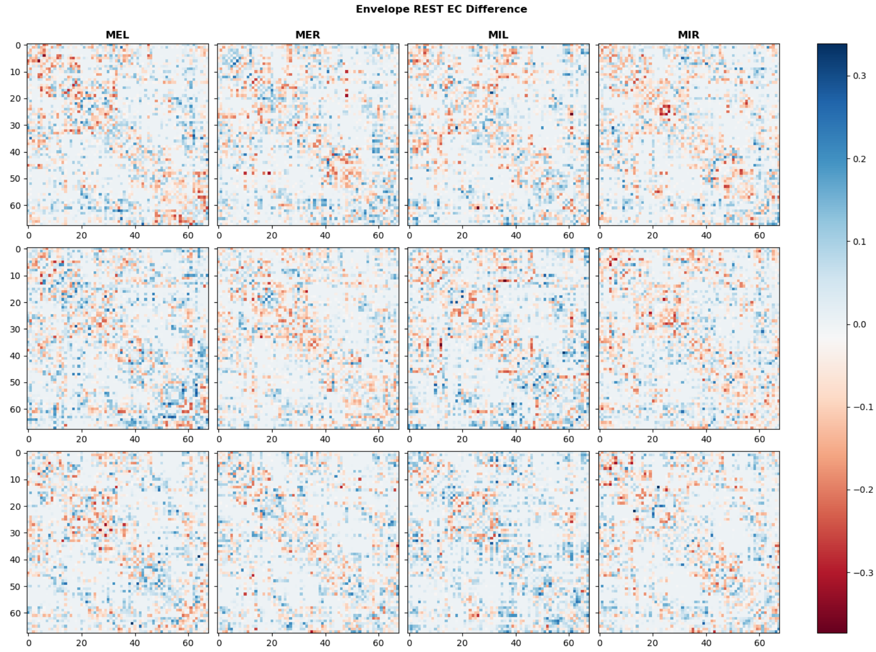

Figure B.27: Differences between REST EC matrix and every other tasktype for each frequency, EC fitted using the Envelope FC.

B.3 Parameter exploration with Effective Connectivity Matrix

Figures B.28 to B.33 show the *G* and *a* parameter exploration using EC across FC metrics and frequency bands.

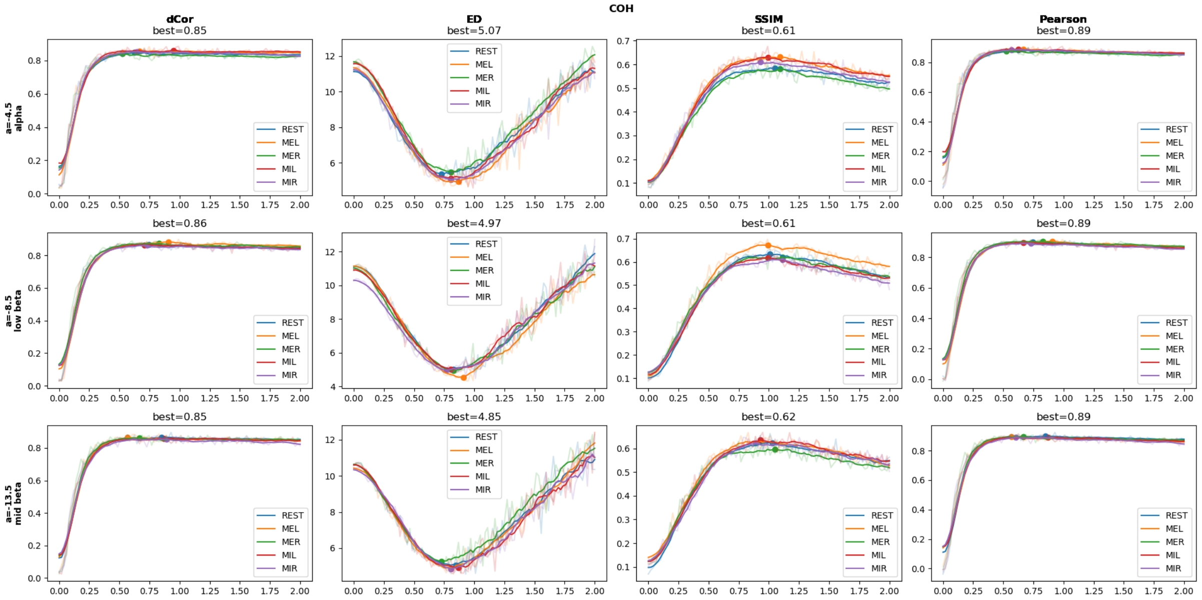

Figure B.28: *G* parameter exploration using EC as the adjacency connectivity matrix, *C*, for every task and frequency band for the COH FC metric. The *a* parameter is the bifurcation location determined for each frequency band. Each color corresponds to a different task's fit with a moving average filter and a dot on the best fit point. The actual fit is displayed in a less opaque color

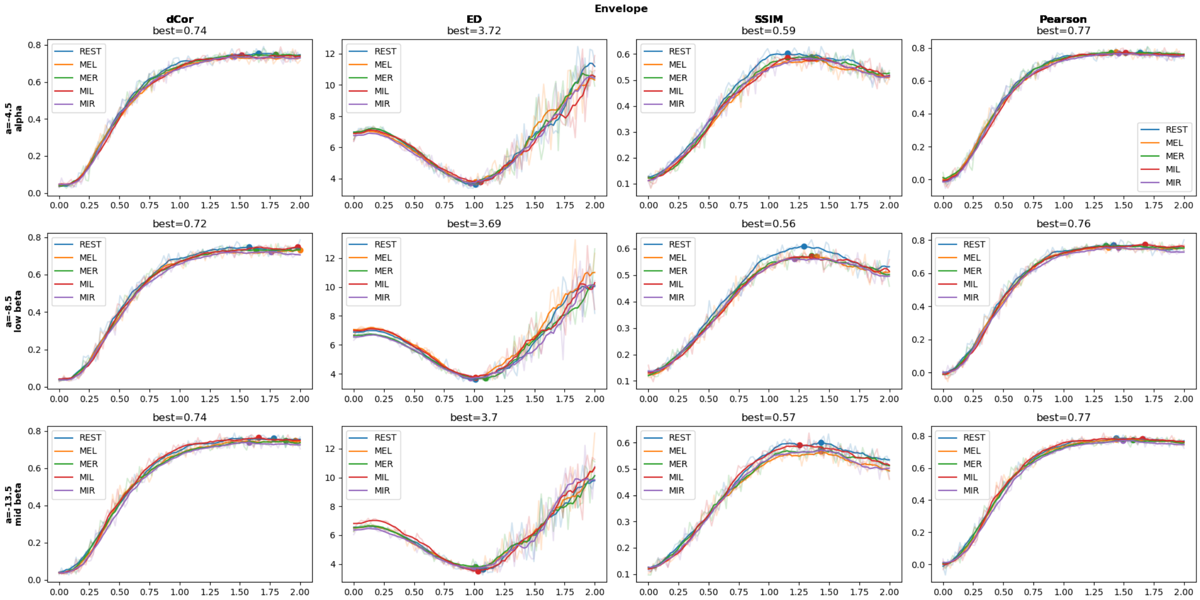

Figure B.29: *G* parameter exploration using EC as the adjacency connectivity matrix, *C*, for every task and frequency band for the Envelope FC metric. The *a* parameter is the bifurcation location determined for each frequency band. Each color corresponds to a different task's fit with a moving average filter and a dot on the best fit point. The actual fit is displayed in a less opaque color

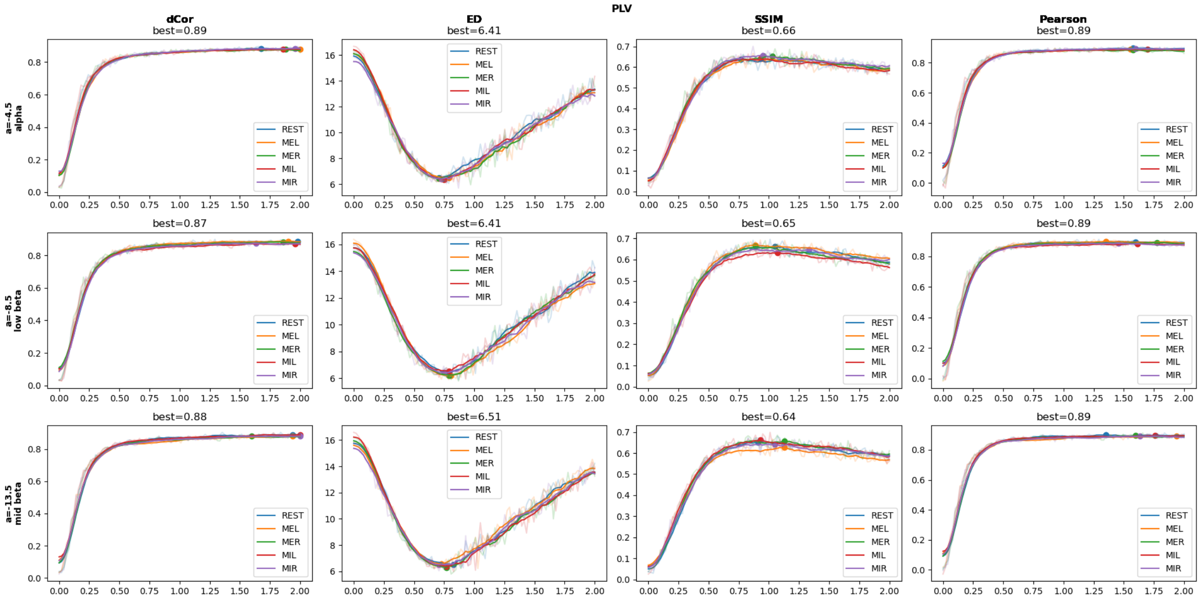

Figure B.30: *G* parameter exploration using EC as the adjacency connectivity matrix, *C*, for every task and frequency band for the PLV FC metric. The *a* parameter is the bifurcation location determined for each frequency band. Each color corresponds to a different task's fit with a moving average filter and a dot on the best fit point. The actual fit is displayed in a less opaque color

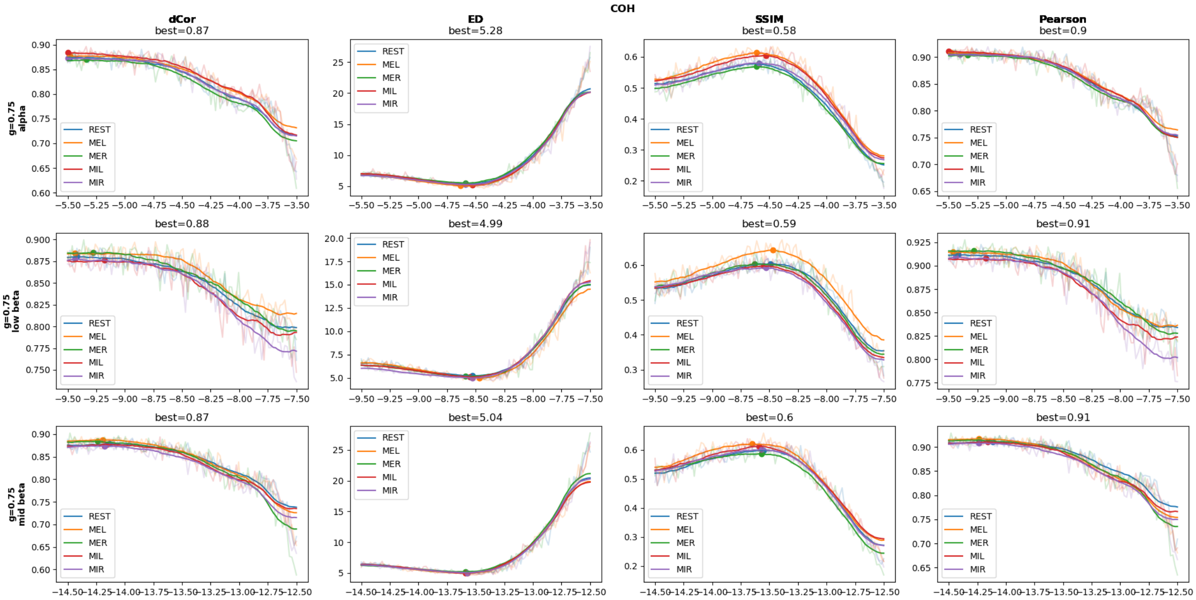

Figure B.31: *a* parameter exploration using EC as the adjacency connectivity matrix, C, for every task and frequency band for the COH FC metric. The G parameter was chosen for each structural connectivity based on the previous G parameter exploration. Each color corresponds to a different task's fit with a moving average filter and a dot on the best fit point. The actual fit is displayed in a less opaque color

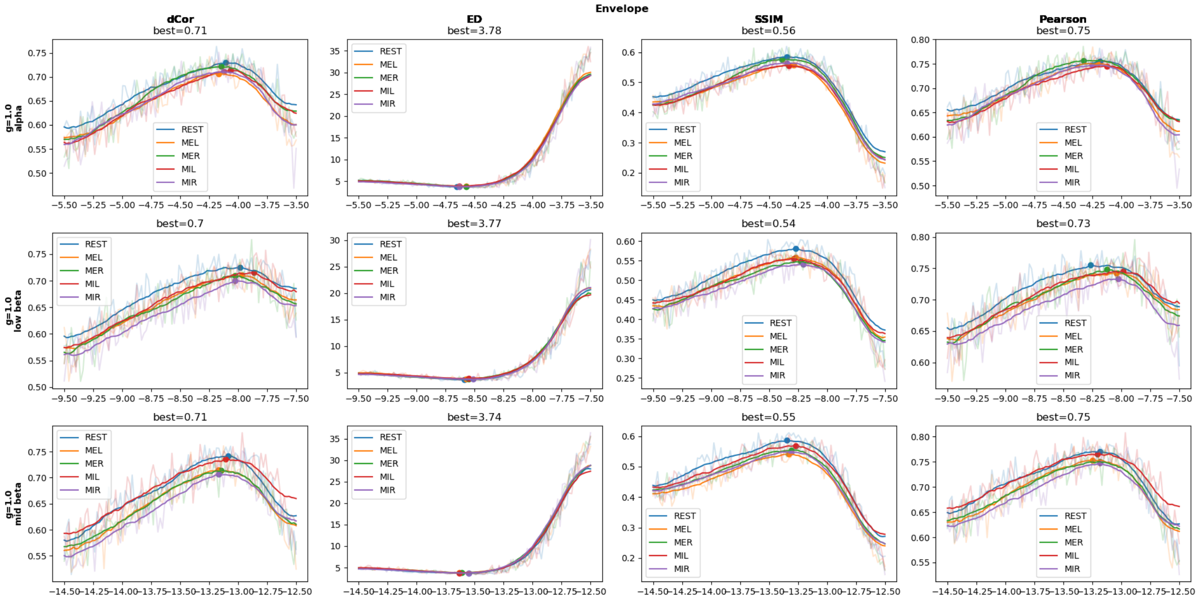

Figure B.32: *a* parameter exploration using EC as the adjacency connectivity matrix, C, for every task and frequency band for the Envelope FC metric. The G parameter was chosen for each structural connectivity based on the previous G parameter exploration. Each color corresponds to a different task's fit with a moving average filter and a dot on the best fit point. The actual fit is displayed in a less opaque color

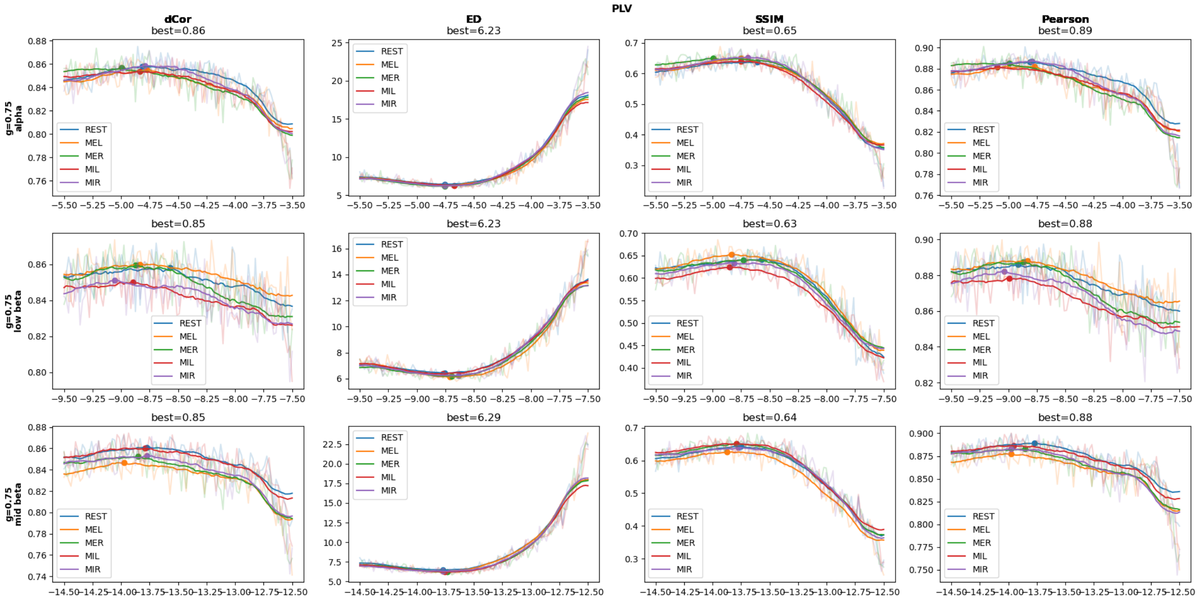

Figure B.33: *a* parameter exploration using EC as the adjacency connectivity matrix, *C*, for every task and frequency band for the PLV FC metric. The *G* parameter was chosen for each structural connectivity based on the previous *G* parameter exploration. Each color corresponds to a different task's fit with a moving average filter and a dot on the best fit point. The actual fit is displayed in a less opaque color

B.4 Metastability and coherence fit

Figures B.34 to B.36 show the metastability and coherence for different *G* values, using EC for each FC metrics and frequency bands. Figures B.37 to B.39 show the estimated *G* parameter that reproduces the empirical metastability and coherence values base on fits from figures B.34 to B.36.

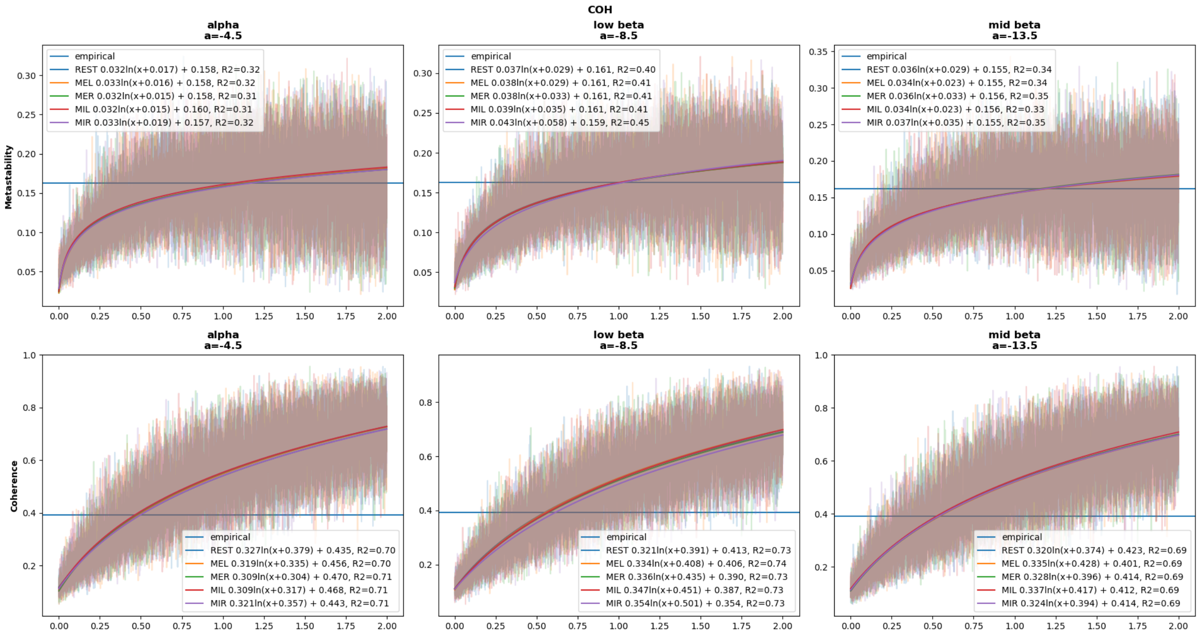

Figure B.34: COH EC coherence and metastability *G* parameter fit for each frequency and the respective critical bifurcation region parameter.

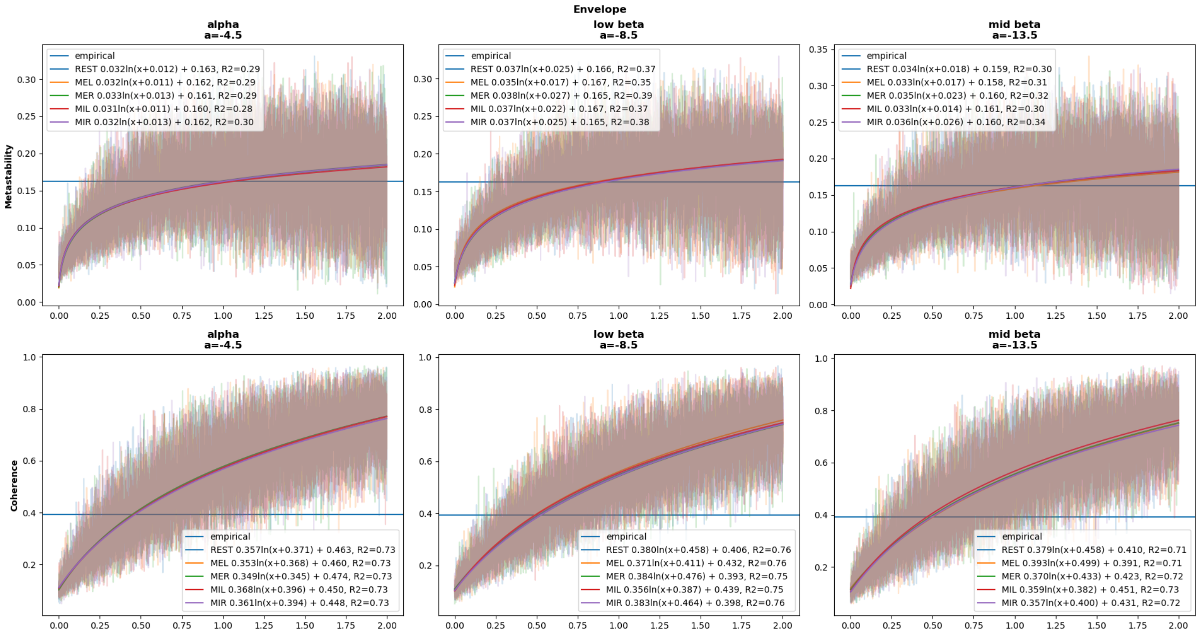

Figure B.35: Envelope EC coherence and metastability *G* parameter fit for each frequency and the respective critical bifurcation region parameter.

B. SIMULATION DATA

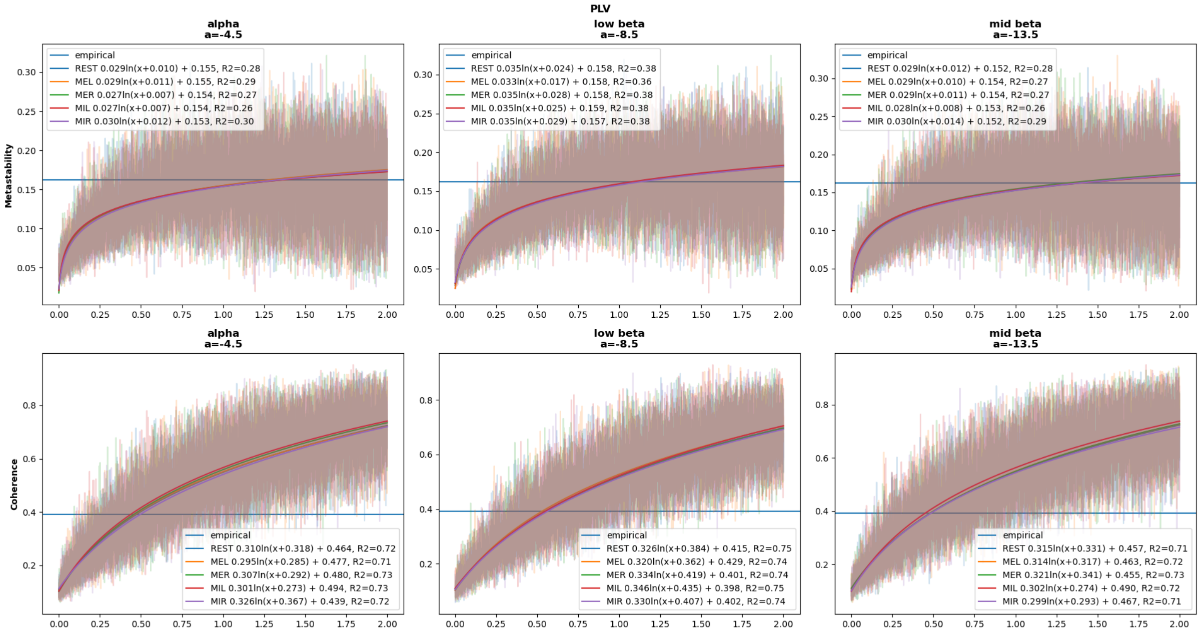

Figure B.36: PLV EC coherence and metastability *G* parameter fit for each frequency and the respective critical bifurcation region parameter.

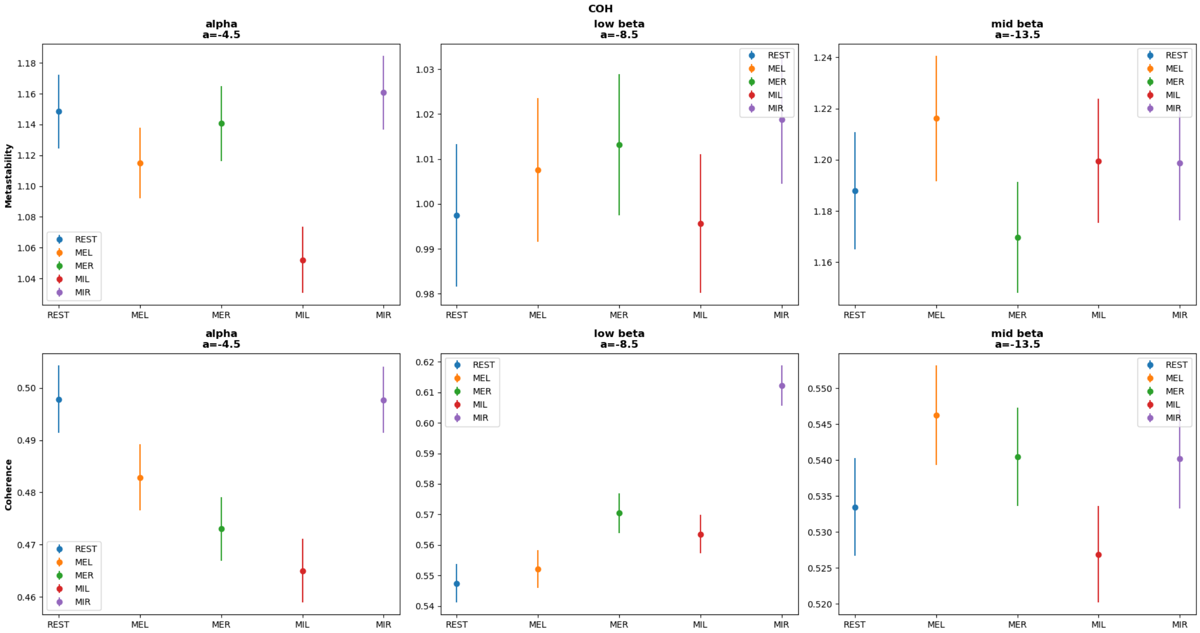

Figure B.37: *G* parameter value estimated from the linear fits, shown in figure B.34.

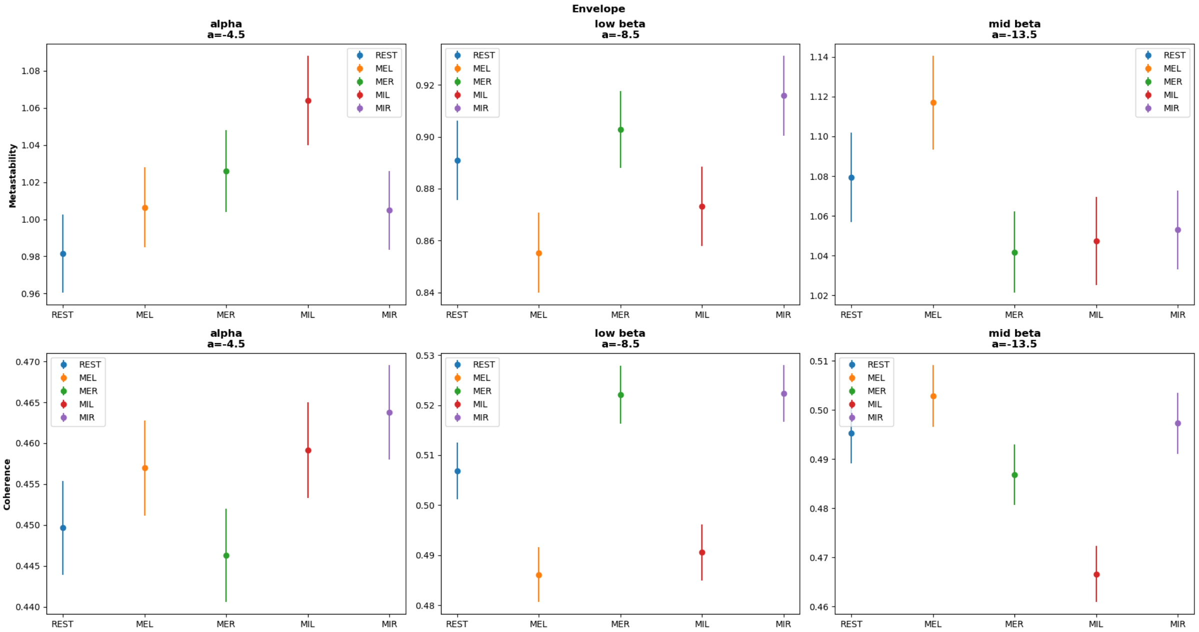

Figure B.38: *G* parameter value estimated from the linear fits, shown in figure B.35.

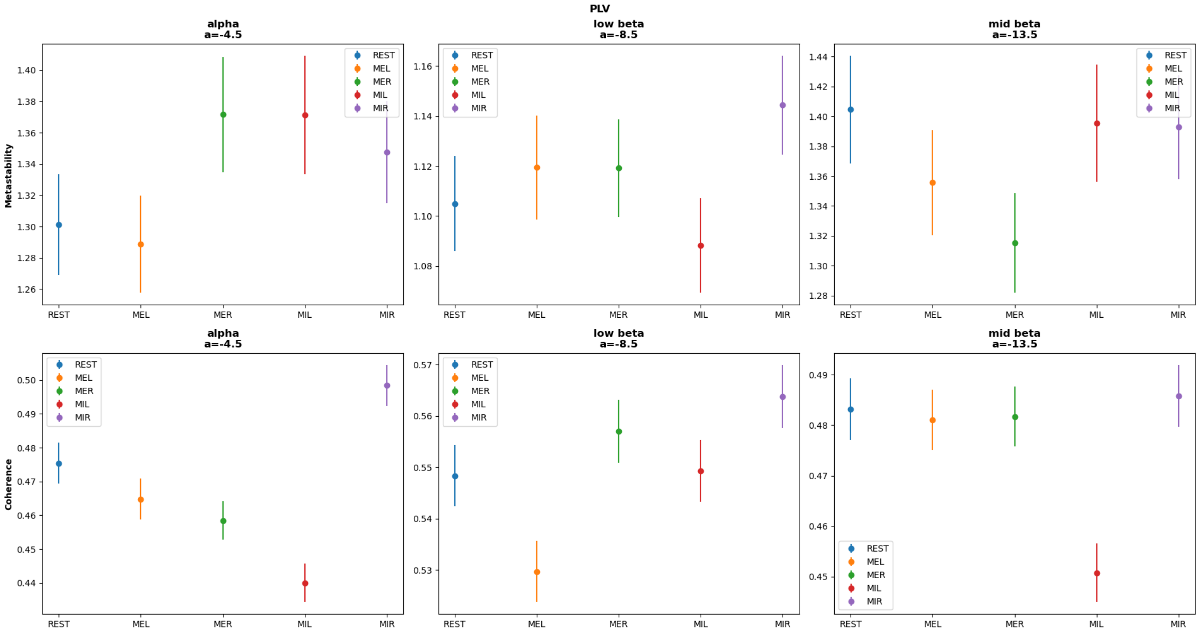

Figure B.39: *G* parameter value estimated from the linear fits, shown in figure B.36.

B.5 Simulated Functional Connectivity Statistical Differences

Tables B.1 to B.9 show the highest statistically significant ($\alpha < 0.05$) differences for each simulated FC metric and frequency band. Figure B.40 shows the box plots of all statistically significant ($\alpha < 0.05$) differences for each simulated FC metric and frequency band.

B. SIMULATION DATA

Table B.1: Simulated Node Connections with significant diferences ($\alpha < 0.05$ and difference>0.115) for COH alpha

method	frequency	node	REST-MEL	MEL-MIL	MEL-MIR	MER-MIL	MIL-MIR
COH	alpha	lateralorbitofrontal-rh-cuneus-rh				0.12	
		lateralorbitofrontal-rh-superiortemporal-rh			0.116		
		parsorbitalis-rh-entorhinal-rh					0.12
		medialorbitofrontal-rh-cuneus-rh				0.119	
		rostralanteriorcingulate-rh-cuneus-rh				0.124	
		cuneus-rh-medialorbitofrontal-lh				0.125	
		cuneus-rh-rostralanteriorcingulate-lh				0.12	
		parstriangularis-lh-supramarginal-lh		-0.137			
		rostralmiddlefrontal-lh-supramarginal-lh		-0.127			
		caudalmiddlefrontal-lh-supramarginal-lh		-0.116			
		precentral-lh-supramarginal-lh	-0.12				
		posteriorcingulate-lh-superiorparietal-lh			0.136		
		supramarginal-lh-fusiform-lh		-0.127			
		supramarginal-lh-temporalpole-lh		-0.144			
		supramarginal-lh-transversetemporal-lh		-0.142	-0.12		
		supramarginal-lh-insula-lh		-0.135			

Table B.2: Simulated Node Connections with significant diferences ($\alpha < 0.05$ and difference>0.115) for COH low beta

method	frequency	node	REST-MEL	MEL-MIR
COH	low beta	lateralorbitofrontal-rh-superiortemporal-rh		0.117
		parsorbitalis-rh-superiortemporal-rh		0.128
		parsorbitalis-rh-insula-rh		0.127
		cuneus-rh-medialorbitofrontal-lh	0.121	
		temporalpole-rh-superiortemporal-rh		0.116
		precentral-lh-paracentral-lh	-0.151	
		precentral-lh-posteriorcingulate-lh	-0.122	

Table B.3: Simulated Node Connections with significant diferences ($\alpha < 0.05$ and difference>0.115) for COH mid beta

method	frequency	node	REST-MEL	MEL-MER	MEL-MIR
COH	mid beta	parsorbitalis-rh-temporalpole-rh		0.122	0.124
		parsorbitalis-rh-insula-rh			0.116
		precentral-lh-paracentral-lh	-0.135	0.12	

Table B.4: Simulated Node Connections with significant diferences ($\alpha < 0.05$ and difference>0.12) for PLV alpha

			REST-MIL	MEL-MER	MEL-MIL	MEL-MIR	MER-MIL	MIL-MIR
method	frequency	node						
PLV	alpha	lateralorbitofrontal-rh-middletemporal-rh			-0.14			0.137
		parsorbitalis-rh-frontalpole-rh						0.153
		parsorbitalis-rh-medialorbitofrontal-rh						0.13
		parsorbitalis-rh-parstriangularis-rh				0.153		0.143
		parsorbitalis-rh-rostralanteriorcingulate-rh						0.126
		parsorbitalis-rh-entorhinal-rh						0.129
		parsorbitalis-rh-insula-rh						0.128
		parsorbitalis-rh-rostralanteriorcingulate-lh						0.126
		parsorbitalis-rh-parahippocampal-lh						0.124
		parsorbitalis-rh-entorhinal-lh						0.133
		frontalpole-rh-middletemporal-rh	-0.122		-0.146			0.146
		medialorbitofrontal-rh-middletemporal-rh			-0.126			0.13
		parstriangularis-rh-middletemporal-rh			-0.128			0.131
		precentral-rh-transversetemporal-rh						0.126
		paracentral-rh-inferiorparietal-rh		-0.127				
		isthmuscingulate-rh-precentral-lh						0.123
		cuneus-rh-pericalcarine-rh		0.125				
		cuneus-rh-pericalcarine-lh		0.136				
		parahippocampal-rh-bankssts-rh					-0.156	0.147
		parahippocampal-rh-transversetemporal-rh					-0.146	0.132
		temporalpole-rh-middletemporal-rh			-0.136			
		middletemporal-rh-bankssts-rh						-0.121
		middletemporal-rh-lateralorbitofrontal-lh			-0.127			0.14
		middletemporal-rh-parsorbitalis-lh						0.127
		middletemporal-rh-frontalpole-lh	-0.121		-0.139			0.132
		middletemporal-rh-medialorbitofrontal-lh	-0.134		-0.152			0.159
		middletemporal-rh-rostralmiddlefrontal-lh						0.13
		superiorfrontal-lh-precentral-lh		0.138		0.128	-0.136	0.126
		precentral-lh-posteriorcingulate-lh						0.128
		precentral-lh-superiorparietal-lh				0.131		0.14
		precentral-lh-precuneus-lh						0.146
		supramarginal-lh-precuneus-lh						0.125
		fusiform-lh-transversetemporal-lh		-0.123				

Table B.5: Simulated Node Connections with significant diferences ($\alpha < 0.05$ and difference>0.12) for PLV low beta

			REST-MER	MEL-MER	MEL-MIR	MER-MIL	MIL-MIR
method	frequency	node					
PLV	low beta	lateralorbitofrontal-rh-parsorbitalis-rh					0.122
		parsorbitalis-rh-frontalpole-rh					0.138
		parsorbitalis-rh-medialorbitofrontal-rh					0.124
		parsorbitalis-rh-parstriangularis-rh			0.122		0.161
		parsorbitalis-rh-entorhinal-rh			0.121		0.145
		parsorbitalis-rh-insula-rh					0.121
		parsorbitalis-rh-entorhinal-lh					0.129
		caudalmiddlefrontal-rh-superiortemporal-rh	0.124	0.132			
		precentral-rh-transversetemporal-rh			0.121		
		posteriorcingulate-rh-supramarginal-lh				-0.121	
		parahippocampal-rh-transversetemporal-rh		0.12	0.131		
		superiortemporal-rh-transversetemporal-rh		0.134	0.121		
		superiorfrontal-lh-precentral-lh		0.144	0.127		
		paracentral-lh-supramarginal-lh				-0.125	
		posteriorcingulate-lh-supramarginal-lh				-0.122	
		supramarginal-lh-precuneus-lh				-0.12	
		temporalpole-lh-transversetemporal-lh		-0.13			

Table B.6: Simulated Node Connections with significant diferences ($\alpha < 0.05$ and difference>0.12) for PLV mid beta

method	frequency	node	REST-MIL	MEL-MER	MEL-MIL	MER-MIR	MIL-MIR
PLV	mid beta	parsorbitalis-rh-frontalpole-rh					0.145
		parsorbitalis-rh-medialorbitofrontal-rh					0.14
		parsorbitalis-rh-parstriangularis-rh	-0.12			0.12	0.161
		parsorbitalis-rh-rostralanteriorcingulate-rh					0.14
		precentral-rh-transversetemporal-rh		0.123			
		rostralanteriorcingulate-rh-parsopercularis-lh					0.127
		bankssts-rh-superiortemporal-rh		0.141			
		parstriangularis-lh-parsopercularis-lh					0.122
		temporalpole-lh-transversetemporal-lh			-0.146		

Table B.7: Simulated Node Connections with significant diferences ($\alpha < 0.05$ and difference>0.065) for Envelope alpha

method	frequency	node	MEL-MER	MER-MIL
Envelope	alpha	rostralmiddlefrontal-rh-superiorfrontal-rh		0.071
		pericalcarine-lh-superiortemporal-lh	-0.069	
		lingual-lh-superiortemporal-lh	-0.065	
		lingual-lh-transversetemporal-lh	-0.069	
		fusiform-lh-transversetemporal-lh	-0.073	

Table B.8: Simulated Node Connections with significant diferences ($\alpha < 0.05$ and difference>0.065) for Envelope low beta

method	frequency	node	REST-MIR	MEL-MER	MEL-MIR	MER-MIR	MIL-MIR
Envelope	low beta	lateralorbitofrontal-rh-transversetemporal-lh					0.069
		frontalpole-rh-transversetemporal-lh					0.067
		medialorbitofrontal-rh-transversetemporal-lh					0.068
		parstriangularis-rh-rostralanteriorcingulate-rh	0.066				
		parstriangularis-rh-medialorbitofrontal-lh	0.07			0.069	
		parstriangularis-rh-rostralanteriorcingulate-lh				0.067	
		rostralanteriorcingulate-rh-transversetemporal-lh					0.067
		medialorbitofrontal-lh-transversetemporal-lh					0.072
		medialorbitofrontal-lh-insula-lh					0.07
		posteriorcingulate-lh-middletemporal-lh		0.066			
		isthmuscingulate-lh-middletemporal-lh		0.081	0.071		
		superiorparietal-lh-middletemporal-lh		0.083			
		precuneus-lh-fusiform-lh		0.068			
		precuneus-lh-middletemporal-lh		0.088	0.067		
		cuneus-lh-middletemporal-lh		0.075	0.072		
		pericalcarine-lh-middletemporal-lh		0.074	0.073		
		lingual-lh-middletemporal-lh		0.067			
		fusiform-lh-middletemporal-lh		0.067			

Table B.9: Simulated Node Connections with significant diferences ($\alpha < 0.05$ and difference>0.065) for Envelope mid beta

			MEL-MIL	MER-MIL	MIL-MIR
method	frequency	node			
Envelope	mid beta	medialorbitofrontal-rh-temporalpole-rh	-0.068		
		medialorbitofrontal-rh-insula-lh		-0.069	
		rostralanteriorcingulate-rh-insula-lh		-0.067	
		temporalpole-rh-lateralorbitofrontal-lh	-0.068		
		temporalpole-rh-frontalpole-lh	-0.071		
		temporalpole-rh-rostralanteriorcingulate-lh	-0.067		
		lateralorbitofrontal-lh-temporalpole-lh	-0.066		
		lateralorbitofrontal-lh-insula-lh		-0.067	
		parsorbitalis-lh-insula-lh		-0.067	
		frontalpole-lh-insula-lh		-0.07	
		medialorbitofrontal-lh-insula-lh		-0.076	0.071
		temporalpole-lh-insula-lh	-0.066		

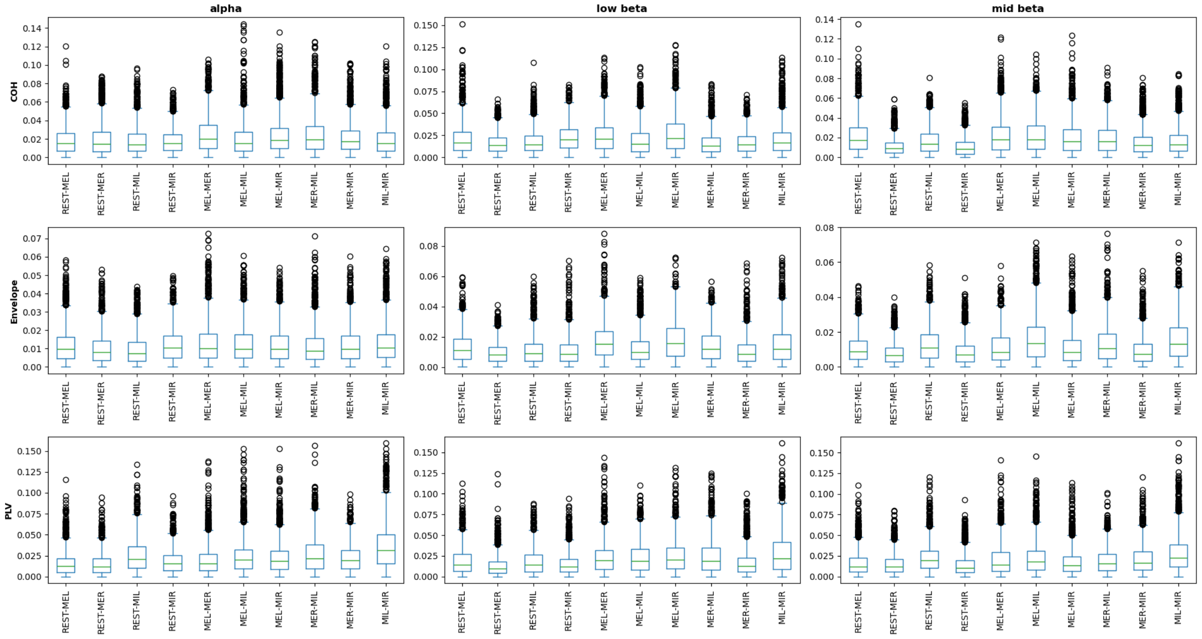

Figure B.40: Box plots of absolute significant simulated differences for all task comparisons frequency bands and FC metrics

B.5.1 Statistical Differences Overlap

freq	method	task comparison	PPV	TPR	NPV	TNR	TP	FP	FN	TN
alpha	COH	REST-MEL	0.899	0.898	0.228	0.231	1808	203	206	61
alpha	COH	REST-MER	0.869	0.895	0.191	0.156	1757	265	207	49
alpha	COH	REST-MIL	0.877	0.902	0.208	0.169	1783	250	194	51
alpha	COH	REST-MIR	0.874	0.897	0.175	0.143	1775	257	203	43
alpha	COH	MEL-MIL	0.878	0.902	0.211	0.173	1784	248	194	52

B. SIMULATION DATA

alpha	COH	MEL-MIR	0.905	0.934	0.192	0.137	1910	201	135	32
alpha	COH	MER-MIR	0.886	0.929	0.23	0.15	1857	238	141	42
alpha	COH	MIL-MIR	0.881	0.888	0.177	0.168	1769	238	223	48
low beta	COH	REST-MEL	0.9	0.921	0.267	0.22	1855	206	159	58
low beta	COH	REST-MER	0.885	0.916	0.254	0.194	1817	237	167	57
low beta	COH	REST-MIL	0.851	0.912	0.232	0.143	1752	306	169	51
low beta	COH	REST-MIR	0.903	0.938	0.244	0.167	1905	205	127	41
low beta	COH	MEL-MER	0.922	0.941	0.169	0.13	1963	167	123	25
low beta	COH	MEL-MIL	0.891	0.9	0.219	0.202	1801	221	200	56
low beta	COH	MEL-MIR	0.905	0.932	0.141	0.103	1915	200	140	23
low beta	COH	MER-MIL	0.896	0.904	0.145	0.134	1837	213	195	33
low beta	COH	MER-MIR	0.875	0.907	0.2	0.153	1793	255	184	46
low beta	COH	MIL-MIR	0.885	0.92	0.243	0.176	1830	238	159	51
mid beta	COH	REST-MEL	0.906	0.914	0.146	0.133	1877	195	176	30
mid beta	COH	REST-MER	0.853	0.852	0.223	0.223	1632	282	283	81
mid beta	COH	REST-MIL	0.852	0.885	0.25	0.199	1692	294	219	73
mid beta	COH	REST-MIR	0.849	0.805	0.192	0.245	1541	274	374	89
mid beta	COH	MEL-MER	0.921	0.918	0.136	0.141	1915	164	172	27
mid beta	COH	MEL-MIL	0.895	0.91	0.192	0.167	1839	215	181	43
mid beta	COH	MEL-MIR	0.898	0.895	0.134	0.138	1825	207	213	33
mid beta	COH	MER-MIL	0.905	0.895	0.205	0.224	1819	191	213	55
mid beta	COH	MER-MIR	0.884	0.874	0.159	0.173	1747	230	253	48
mid beta	COH	MIL-MIR	0.877	0.887	0.158	0.145	1765	247	224	42
alpha	PLV	REST-MEL	0.894	0.796	0.196	0.345	1584	188	407	99
alpha	PLV	REST-MER	0.894	0.79	0.207	0.369	1566	186	417	109
alpha	PLV	REST-MIL	0.891	0.905	0.218	0.193	1814	221	190	53
alpha	PLV	REST-MIR	0.864	0.855	0.206	0.218	1661	262	282	73
alpha	PLV	MEL-MER	0.902	0.861	0.15	0.207	1753	191	284	50
alpha	PLV	MEL-MIL	0.901	0.886	0.131	0.15	1812	199	232	35
alpha	PLV	MER-MIR	0.899	0.883	0.191	0.219	1785	200	237	56
alpha	PLV	MIL-MIR	0.898	0.924	0.083	0.061	1894	215	155	14
low beta	PLV	REST-MEL	0.886	0.832	0.197	0.279	1650	212	334	82
low beta	PLV	REST-MER	0.877	0.744	0.197	0.377	1452	203	500	123
low beta	PLV	REST-MIL	0.891	0.809	0.166	0.276	1620	199	383	76
low beta	PLV	REST-MIR	0.872	0.789	0.192	0.302	1541	226	413	98
low beta	PLV	MEL-MER	0.915	0.874	0.183	0.259	1795	166	259	58
low beta	PLV	MEL-MIL	0.915	0.871	0.192	0.275	1784	166	265	63
low beta	PLV	MEL-MIR	0.901	0.877	0.197	0.239	1775	194	248	61
low beta	PLV	MER-MIL	0.896	0.869	0.165	0.202	1757	205	264	52
low beta	PLV	MER-MIR	0.891	0.803	0.186	0.316	1600	195	393	90
low beta	PLV	MIL-MIR	0.908	0.878	0.184	0.235	1792	182	248	56
mid beta	PLV	REST-MEL	0.89	0.82	0.176	0.276	1639	202	360	77
mid beta	PLV	REST-MER	0.877	0.807	0.212	0.315	1576	222	378	102
mid beta	PLV	REST-MIL	0.881	0.9	0.202	0.172	1789	241	198	50
mid beta	PLV	REST-MIR	0.884	0.782	0.223	0.379	1530	200	426	122

mid beta	PLV	MEL-MER	0.901	0.832	0.205	0.321	1670	184	337	87
mid beta	PLV	MEL-MIL	0.911	0.859	0.182	0.272	1755	171	288	64
mid beta	PLV	MEL-MIR	0.899	0.833	0.202	0.312	1671	187	335	85
mid beta	PLV	MER-MIL	0.897	0.854	0.179	0.244	1722	198	294	64
mid beta	PLV	MER-MIR	0.895	0.866	0.211	0.262	1734	203	269	72
mid beta	PLV	MIL-MIR	0.908	0.909	0.166	0.164	1866	189	186	37
alpha	Envelope	REST-MEL	0.91	0.758	0.15	0.364	1546	152	493	87
alpha	Envelope	REST-MER	0.901	0.712	0.201	0.483	1409	154	571	144
alpha	Envelope	REST-MIL	0.898	0.67	0.157	0.446	1341	153	661	123
alpha	Envelope	REST-MIR	0.905	0.789	0.184	0.366	1590	166	426	96
alpha	Envelope	MEL-MER	0.916	0.776	0.132	0.324	1601	146	461	70
alpha	Envelope	MEL-MIL	0.909	0.781	0.157	0.343	1590	159	446	83
alpha	Envelope	MER-MIL	0.926	0.75	0.156	0.436	1545	123	515	95
alpha	Envelope	MER-MIR	0.915	0.759	0.15	0.377	1554	144	493	87
low beta	Envelope	REST-MEL	0.894	0.803	0.166	0.293	1612	191	396	79
low beta	Envelope	REST-MER	0.909	0.724	0.15	0.401	1471	148	560	99
low beta	Envelope	REST-MIL	0.904	0.737	0.13	0.333	1502	160	536	80
low beta	Envelope	REST-MIR	0.883	0.717	0.151	0.346	1427	189	562	100
low beta	Envelope	MEL-MER	0.925	0.867	0.134	0.228	1811	146	278	43
low beta	Envelope	MEL-MIL	0.932	0.786	0.141	0.38	1640	119	446	73
low beta	Envelope	MEL-MIR	0.923	0.854	0.134	0.24	1779	149	303	47
low beta	Envelope	MER-MIL	0.921	0.822	0.162	0.327	1694	146	367	71
low beta	Envelope	MER-MIR	0.919	0.739	0.153	0.422	1513	133	535	97
low beta	Envelope	MIL-MIR	0.91	0.786	0.139	0.309	1609	159	439	71
mid beta	Envelope	REST-MEL	0.905	0.758	0.156	0.361	1535	161	491	91
mid beta	Envelope	REST-MER	0.903	0.654	0.182	0.524	1299	139	687	153
mid beta	Envelope	REST-MIL	0.915	0.796	0.157	0.339	1630	152	418	78
mid beta	Envelope	REST-MIR	0.907	0.668	0.138	0.437	1356	139	675	108
mid beta	Envelope	MEL-MIL	0.921	0.812	0.124	0.276	1689	144	390	55
mid beta	Envelope	MEL-MIR	0.924	0.72	0.127	0.408	1492	122	580	84
mid beta	Envelope	MER-MIL	0.923	0.775	0.112	0.306	1615	134	470	59
mid beta	Envelope	MER-MIR	0.939	0.687	0.13	0.513	1433	93	654	98
mid beta	Envelope	MIL-MIR	0.934	0.826	0.148	0.339	1728	123	364	63

Table B.10: Overlap between empirical and simulated connections that show significant differences for each frequency, method and task comparison. Only significant overlap metrics ($\alpha < 0.05$) are shown